SANDIA REPORT

SAND2003-1235
Unlimited Release
Printed April 2003

Hypervelocity Impacts on Aluminum from 6 to 11 km/s for Hydrocode Benchmarking

Lalit C. Chhabildas, William D. Reinhart, Tom F. Thornhill, Gregory C. Bessette, W. Venner Saul, R. Jeffery Lawrence, and Marlin E. Kipp

Prepared by
Sandia National Laboratories
Albuquerque, New Mexico 87185 and Livermore, California 94550

Sandia is a multiprogram laboratory operated by Sandia Corporation,
a Lockheed Martin Company, for the United States Department of Energy's
National Nuclear Security Administration under Contract DE-AC04-94AL85000.

Sandia National Laboratories

Issued by Sandia National Laboratories, operated for the United States Department of Energy by Sandia Corporation.

Available to DOE and DOE contractors from
U.S. Department of Energy
Office of Scientific and Technical Information
P.O. Box 62
Oak Ridge, TN 37831

Telephone: (865) 576-8401
Facsimile: (865) 576-5728
E-Mail: reports@adonis.osti.gov
Online ordering: http://www.doe.gov/bridge

Available to the public from
U.S. Department of Commerce
National Technical Information Service
5285 Port Royal Rd.
Springfield, VA 22161

Telephone: (800) 553-6847
Facsimile: (703) 605-6900
E-Mail: orders@ntis.fedworld.gov
Online order: http://www.ntis.gov/help/ordermethods.asp?loc=7-4-0#online

SAND2003-1235
Unlimited Release
Printed April 2003

Hypervelocity Impacts on Aluminum from 6 to 11 km/s for Hydrocode Benchmarking

Lalit C. Chhabildas, William D. Reinhart, Tom F. Thornhill, Gregory C. Bessette, W. Venner Saul, R. Jeffery Lawrence, and Marlin E. Kipp

Sandia National Laboratories
P.O. Box 5800
Albuquerque, NM 87185-1181

Abstract

A systematic computational and experimental study is presented on impact generated debris resulting from record-high impact speeds recently achieved on the Sandia three-stage light-gas gun. In these experiments, a target plate of aluminum is impacted by a titanium-alloy flyer plate at speeds ranging from 6.5 to 11 km/s, producing pressures from 1 Mb to over 2.3 Mb, and temperatures as high as 15000 K (>1 eV). The aluminum plate is totally melted at stresses above 1.6 Mb. Upon release, the thermodynamic release isentropes will interact with the vapor dome. The amount of vapor generated in the debris cloud will depend on many factors such as the thickness of the aluminum plate, super-cooling, vaporization kinetics, the distance, and therefore time, over which the impact-generated debris is allowed to expand. To characterize the debris cloud, the velocity history produced by stagnation of the aluminum expansion products against a witness plate is measured using velocity interferometry. X-ray measurements of the debris cloud are also recorded prior to stagnation against an aluminum witness plate. Both radiographs and witness-plate velocity measurements suggest that the vaporization process is both time-dependent and heterogeneous when the material is released from shocked states around 230 GPa. Experiments suggest that the threshold for vaporization kinetics in aluminum should become significant when expanded from shocked states over 230 GPa. Numerical simulations are conducted to compare the measured x-ray radiographs of the debris cloud and the time-resolved experimental interferometer record with calculational results using the 3-D hydrodynamic wavecode, CTH. Results of these experiments and calculations are discussed in this paper.

Intentionally Left Blank

Acknowledgments

Sandia is a multiprogram laboratory operated by Sandia Corporation, a Lockheed Martin Company, for the United States Department of Energy's National Nuclear Security Administration under Contract DE-AC04-94AL85000. John Martinez is acknowledged for his support with the experiments.

Intentionally Left Blank

Contents

Intentionallly left blank

1. Introduction

Aluminum is an engineering material that is used extensively in space structures such as the space station, satellite structures, and space vehicles. For many of these space applications there is a potential for engagement with either meteorites or space debris. Relevant impact velocities can span the range from a few km/s to velocities approaching 15 km/s. Prediction of the interaction between expanded vaporized debris for the target material resulting from high speed impacts demands an accurate treatment of the melting and vaporization process, and the kinetics of liquid-vapor propagation. Historically, experimental efforts to understand high-pressure melting and vaporization have been hindered by the unavailability of experimental launchers that are capable of speeds needed to induce vaporized states [1]. This problem has been circumvented to some extent by studying materials such as lead, cadmium, and zinc, which have relatively low melting and boiling points [2–5]. For materials of greater programmatic interest (such as aluminum), an alternative is to shock *porous* samples for which irreversible pore collapse enhances heating of the matrix material [6,7]. In this paper, we describe our achievement of record-high impact speeds on *solid* aluminum. Using the new Sandia Hypervelocity Launcher, also referred to as the three-stage light-gas gun [8-10], a titanium flyer plate was launched to speeds from 6.5 km/s to 11 km/s. The flyer impacted a target plate of aluminum, producing shock pressures from about 1 Mb to over 2.3 Mb, and temperatures as high as 11000 K (~1 eV). The release isentropes computed from these states will intersect the vapor dome (see Figure 1.01). To characterize the expanded states, the

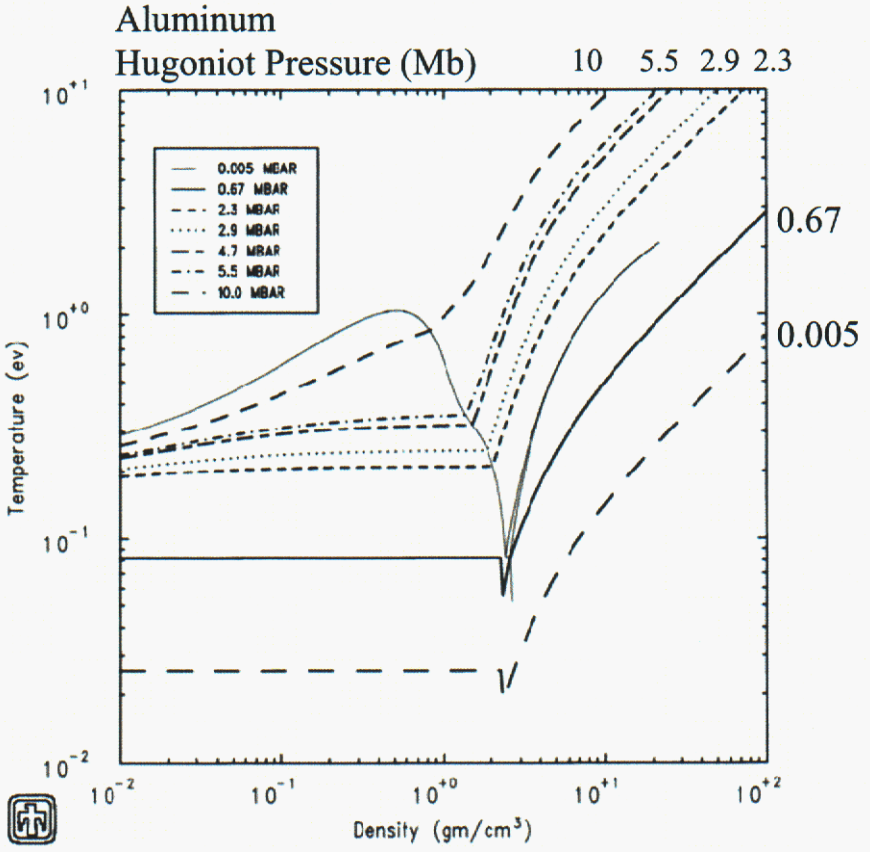

***Figure 1.01**. Calculated phase diagram for aluminum.*

velocity history produced by stagnation of the expansion products against a witness plate is measured using velocity interferometers. X-ray measurements of the debris cloud are also recorded prior to stagnation against the witness plate. The amount by which peak witness-plate velocity decreases for increasing distance between the aluminum target and witness plate is an indicator of the degree of vaporization. Aluminum was chosen for this study because it is an important space engineering material. Furthermore, previously measured experimental data exist for lower-speed impact of aluminum [6], and the commonly used equation of state [11-12] represented these earlier lower-speed lower-pressure experiments for aluminum remarkably well.

The purpose of this paper is: (1) to report the first 1-D, 2-D, and 3-D experimental results for *partial* vaporization of aluminum resulting from shock-compression up to ~2.3 Mb and ~15000 K; and (2) to use these experiments to evaluate the predictions of the Sesame equation of state for aluminum [12], which is most commonly used in CTH [13-15]. This equation of state has been rather well established (and therefore commonly used), and it is thus important to report any results that limit the model's range of applicability. Calculations based on these equations of state have been shown in previous studies [6] to match data for one-dimensional shock release of aluminum for small propagation distances. However, for higher shock states, increasing levels of melting and vaporization of the aluminum should occur, and yet, again for short propagation distances, one-dimensional predictions adequately match the data. In contrast, calculations using these equations of state at intermediate impact velocities, where partial, heterogeneous, and possibly rate-dependent decomposition occurs, are less successful. This is especially true for larger propagation distances, for which multi-dimensional and rate-dependent processes have more space and time to come into play. It is in these latter parameter regimes that currently available equations of state, which lack non-equilibrium effects, do not fully describe the relevant phenomena.

2. Experimental Technique

The three-stage light-gas gun, also referred to as the hypervelocity launcher, was developed in the early nineties [8-9]. Since then, its capabilities have been enhanced to achieve higher engagement velocities, up to 16 km/s [10]. These capabilities were applied for use with applications such as shock-induced vaporization studies [2-5], to assess impact damage to orbital substructures [16], and to perform equation-of-state studies on composite materials [17, 18]. For the code validation studies reported here, methodologies have been developed and refined to achieve the higher degree of precision needed. This includes determining the conditions prior to impact, the imaging of high quality x rays of the impact-generated debris, and using multiple velocity interferometers to record the impulsive loading on the witness plate. In this section, a brief description of the entire experimental set up is given for the sake of completeness. The reader is referred to many of the published references for a more detailed description.

2.1 History of the Three-stage Gun

The Sandia hypervelocity launcher, a three-stage gun, is briefly described here. A two-stage light-gas gun (TSLGG) projectile is accelerated and impacts a stationary flyer plate (Figure 2.01a), which is subsequently launched at velocities from 6 km/s to greater than 11 km/s, depending on the TSLGG projectile impact velocity. The loading pressure pulse on the flyer plate must be uniform and time-dependent to prevent the melting or vaporization of the flyer. To accomplish the time-dependent loading, an assembly of materials with varying shock impedance [19-21] on the TSLGG projectile is used. When this graded-density assembly, shown in Figure 2.01(b), is used to impact a flyer plate, the time-dependent pressure pulse introduces nearly shockless, megabar pressures into the flyer plate [8-10]. This pressure pulse must also be tailored to prevent spallation of the flyer. This technique is now routinely used to launch 17- to 19-mm-diameter, 0.6- to 1.0-mm-thick titanium flyers to velocities greater than 11 km/s. A typical flyer-plate (radiograph) is shown in Figure 2.01(c).

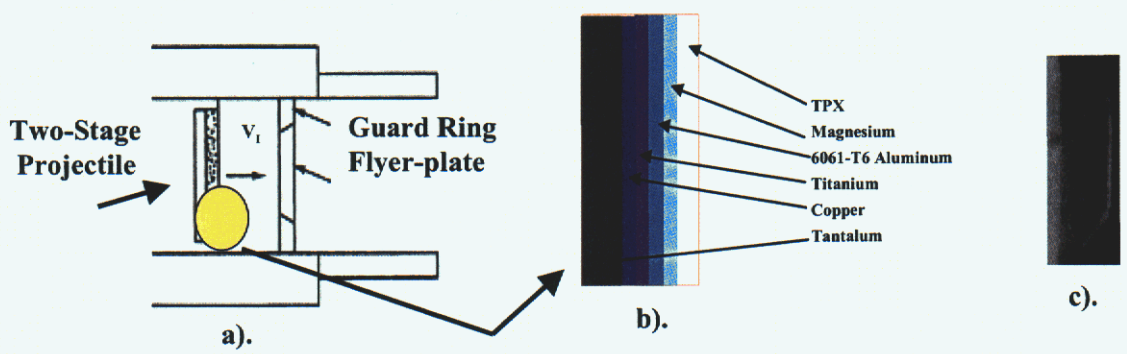

Figure 2.01. *(a) Two-stage projectile and third stage flyer-plate configuration. (b) Graded density impactor with TPX facing impacting the stationary flyer plate. (c) X-ray radiograph of typical three-stage flyer plate traveling at 11.1 km/s.*

Table 2-1. *Summary of impact conditions for the long throw and short throw 2-D experiments.*

Experiment Number	Calculated Impact Velocity (km/s)	Flyer (Ti6Al4V) Thk. (mm)	Target (Al) Thk. (mm)	Flyer-Target Stand-off Distance (mm)	Witness (Al) Thk. (mm)	Target-Witness Stand-off Distance (mm)
CLP-1-LT	10.94	0.894	2.489	751	4.039	74.79
CLP-2-LT	6.49	0.800	2.421	758	3.978	75.02
CLP-7-LT	10..9	0.897	2.469	764	3.998	74.79
CLP-3	9.18	0.896	2.451	30.11	2.019	52.00
CLP-4	10.4	0.841	2.455	30.11	1.996	51.63
CLP-5	11.0	0.897	2.454	30.14	1.902	51.61
CLP-6	9.32	0.902	0.993	30.02	2.031	23.03
CLP-8	9.00	0.904	0.975	30.09	2.019	49.85
CLP-9	9.02	0.894	0.940	29.70	2.021	49.22
CLP-10	9.09	0.902	0.996	30.08	n/a	n/a
CLP-11	8.94	0.897	0.992	34.08	n/a	n/a
CLP-12	11.0	0.894	1.006	34.01	n/a	n/a
CLP-13	8.87	0.907	1.000	34.00	n/a	n/a
CLP-14	8.88	0.909	0.940	30.09	5.693	49.97
CLP-15	10.8	0.904	0.937	30.10	5.692	50.68
CLP-20	6.48	0.904	2.46	77.96	4.036	74.34
CLP-22	10.8	0.903	0.9966	30.10	3.986	10.01
CLP23	10.8	0.903	0.9966	30.10	3.986	50.01

Table 2-2. *Summary of impact conditions for 3-D experiments.*

Experiment Number	Calculated Impact Velocity (km/s)	Flyer (Ti6Al4V) Thkns (mm)	Target (Al) Thkns (mm)	Target Angle Off Vertical (deg)	Flyer-Target Stand-off Distance (mm)	Witness (Al) Thk. (mm)	Witness Angle Off Vertical (deg)	Target-Witness Stand-off Distance (mm)
CLP-16	10.9	0.902	0.993	19.8	77.41	n/a	n/a	n/a
CLP-17	9.04	0.881	1.003	20.0	77.69	n/a	n/a	n/a
CLP-18	10.86	0.909	0.987	20.0	78.14	4.033	7.0	50.83
CLP-19	8.96	0.886	0.995	20.0	78.14	4.035	7.0	50.83
CLP-21	11.18	0.9017	0.991	20.0	78.14	4.031	7.0	50.83

2.2 Two-stage Projectile

The TSLGG projectile for these experiments is an integral part of the technique to launch plates to high velocities and subsequently to obtain the relevant data at extremely high pressures. The projectile velocity must be known to better than 0.2%, the graded-density impactor must be intact, and the tilt of the projectile upon impact must be small for proper three-stage flyer plate launch.

The projectile velocity is measured using a new technique called the Optical Beam Reflectance (OBR) system (Figure 2.02) [22]. In these studies, five (5) fiber probes (indicated in Figure 2.02) are located in the barrel extension with approximately 57 mm incremental separation, and overall separation of about 228 mm. The spacing between each station segment is known to 0.025 mm. The output of the OBR is shown in Figure 2.02 (three outputs—typical—are shown from a low velocity shot). The transit time of approximately 20 μs between each station is determined to better than 2 ns. This system clearly allows determination of projectile velocity to better than 0.2% [23, 24]. The OBR concept shown in Figure 2.02 uses a fiber bundle (probe), a photomultiplier tube, laser, and recording system. The probe has a 200-μm center fiber surrounded by nine 100-μm fibers. The larger centered fiber is aligned to transmit the laser light, while the surrounding smaller nine fibers collect the reflected light from the moving projectile and transmit it to the recording system. All return fiber outputs are coupled into a single photomultiplier tube, which reduces timing and rise-time uncertainties in contrast to long coaxial cable lengths.

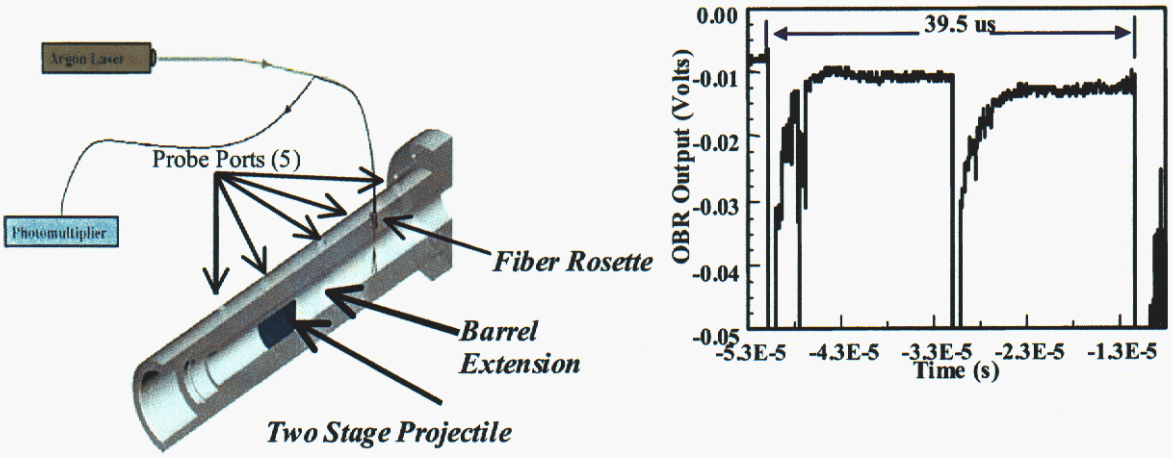

Figure 2.02. *Cut away drawing of the OBR system is on the left. Typical OBR output signal is shown on the right.*

2.3 Flyer Plate Configuration

As shown in Figure 2.03, the flyer-plate configuration used in the experiments consists of a center plate (flyer) made to fit exactly into a guard ring. Upon impact of the flyer plate by the TSLGG projectile, two-dimensional effects due to radial release waves emanating from the edges of the guard-ring will cause a velocity gradient across the radius of the flyer-plate geometry. These velocity gradients will cause the flyer to bow and possibly fragment. The guard-ring geometry shown in Figure 2.03(a) allows controlled separation of the center plate (flyer) from the edges without causing plate bowing and fragmentation. To ensure that the flyer plate is launched intact, the guard-ring geometry (shown in Figure 2.03b) is used in all experiments. The TPX buffer is a low-density plastic, which is designed specifically for controlled release, to avoid high tensile stresses forming within the flyer plate. This prevents spallation of the flyer plate.

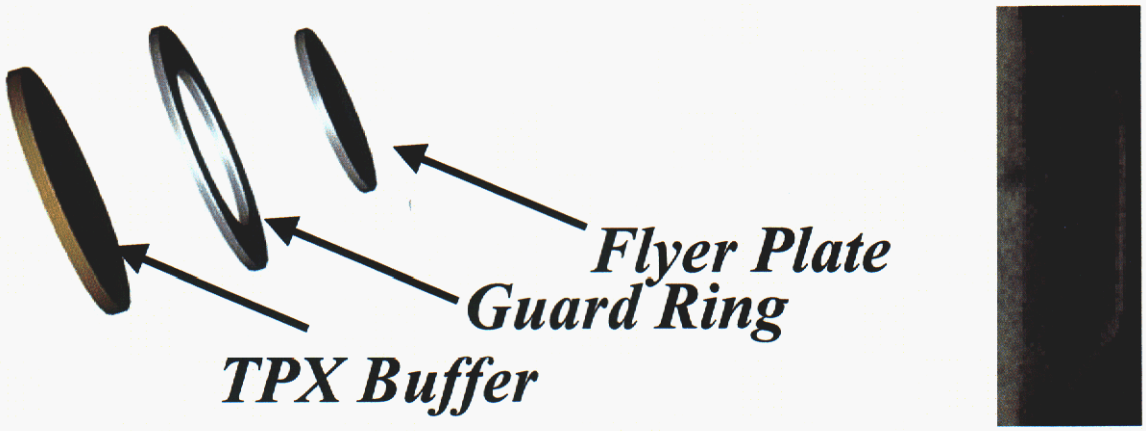

Figure 2.03. *a) Flyer plate geometry, b) radiograph of flyer plate launched to approximately 11 km/s.*

Following the launch, to obtain a viable and a well-defined input for CTH code validation simulations, the flyer plate's velocity, impact conditions, and geometry must be well known. To obtain the flyer-plate velocity and flyer-plate integrity, four flash x rays are taken of the flyer plate while it is in motion over a flight distance of nearly a meter. The x-rays are taken at approximately 50 mm, 250 mm, and 750 mm from its launched position. These x-ray sources have a 150 keV photon energy and a 30 ns pulse duration. Due to the hypervelocities achieved, the 30 ns pulse duration will cause approximately 300 μm of blurring of the flyer plate while it is in flight. Nevertheless, radiographs taken of the flyer plate over these distances provide flyer-plate velocity accuracy to better than 1%.

2.4 Target Configuration

Three target configurations were used for this study. They were; flyer-plate long-propagation experiments, two-dimensional (2-D) flyer-plate short-propagation experiments, and three-dimensional (3-D) flyer-plate short-propagation experiments. All targets and witness plates were fabricated from sheet stock aluminum 6061-T6 in varying geometries. The target and witness plates for all experiments are stock materials and the measured thickness of the stock sheet can vary ±0.0254 mm.

The flyer-plate long-propagation experiments involve launching the flyer 750 mm downrange into the target. The target is either a 1-mm or 2.4-mm-thick plate, 300 mm square. The witness plate is 4 mm thick, 300 mm square, and mounted 75 mm down range of the target plate with VISARs monitoring multiple locations on the free rear surface. Figure 2.04 shows a picture of a typical long-propagation target/witness-plate assembly. This assembly is slotted outside of the flyer and debris impact zone to allow insertion mounting of two x-ray film cassettes. This experimental configuration allows for six radiographs during the experiment, four flyer-plate radiographs for flyer velocity measurement and orthogonal pre-impact characterization, and two radiographs for target post-impact debris orthogonal characterization. Figure 2.05 shows a schematic representation of the x-ray head, film cassette, and target/witness plate layout.

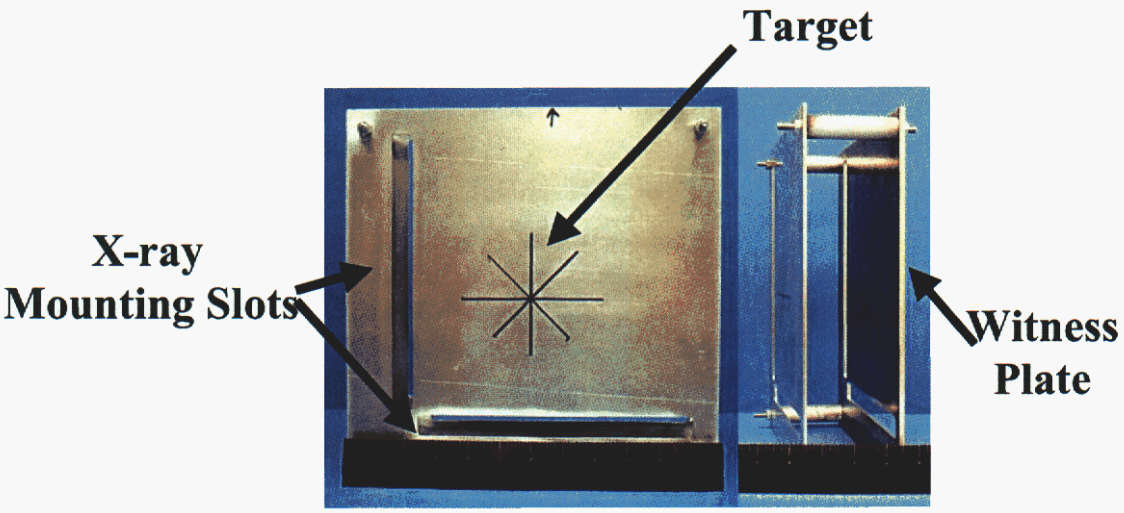

Figure 2.04. *CLP long flyer propagation target/witness plate assembly.*

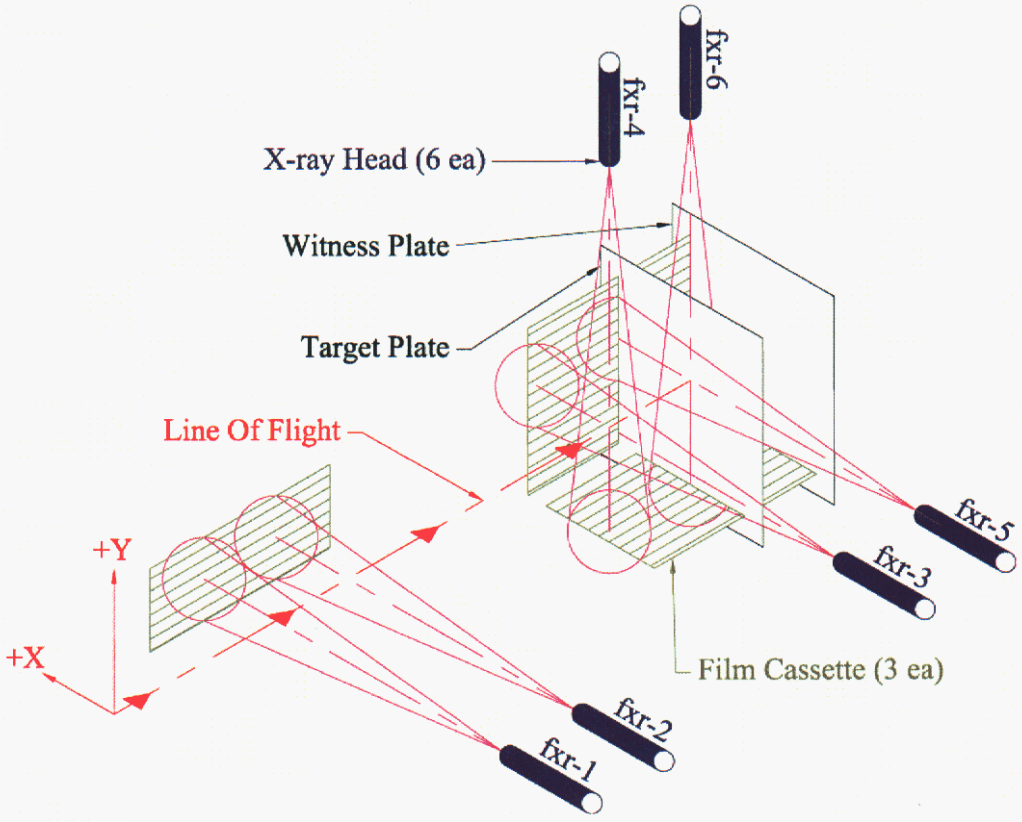

Figure 2.05. *Experimental set-up used in this investigation with emphasis on the schematic of x-ray positions. X rays fxr-1 through fxr-4 is used to measure flyer velocity, while x rays fxr-5 and fxr-6 are used to image the debris cloud.*

For long propagation experiments the target is aligned to the gun bore (*i.e.*, the nominal flyer plate orientation) using a precision-machined alignment rod with straightness callout of 0.0254 mm per 300 mm (1 mil per foot). The rod is leveled with the target fixture and the barrel extension ensuring that the center of the target is aligned to the center of the flyer to approximately 1.0 mm. Perpendicularity of the target to the anticipated trajectory flight of the flyer is performed using right-angled squares and is aligned to better than one degree. The witness plate stand-off is achieved using 75 mm aluminum spacers with dimensional callouts to ±75 μm in length. This ensures the witness and target plates will have consistent spacing throughout the experimental series. The parallelism between the witness and the target plates was measured to be ±70 μm. Exact dimensions for each long propagation experiment are noted in Table 2-1.

The 2-D experiments reduce the flyer plate propagation distance down to approximately 30 mm. This also reduces the target plate radial size to 50 mm diameter. Two nominal target plate thicknesses of 1 mm and 2.4 mm were used. Two types of 2-D experiments were performed in this configuration, a target debris characterization using radiograph(s) with no witness plate, and witness plate with VISARs monitoring the interface of the witness plate and a lithium fluoride (LiF) window at multiple locations. The witness plate thickness is 2 mm, or 5.7 mm thick with a 50 mm stand-off from the target plate.

Figure 2.06 shows a cross section representation of the 2-D experimental hardware. For the 2-D debris characterization shots the witness mount and witness plate were removed, and radiographs of the debris were taken approximately 50 mm downrange from the target plate.

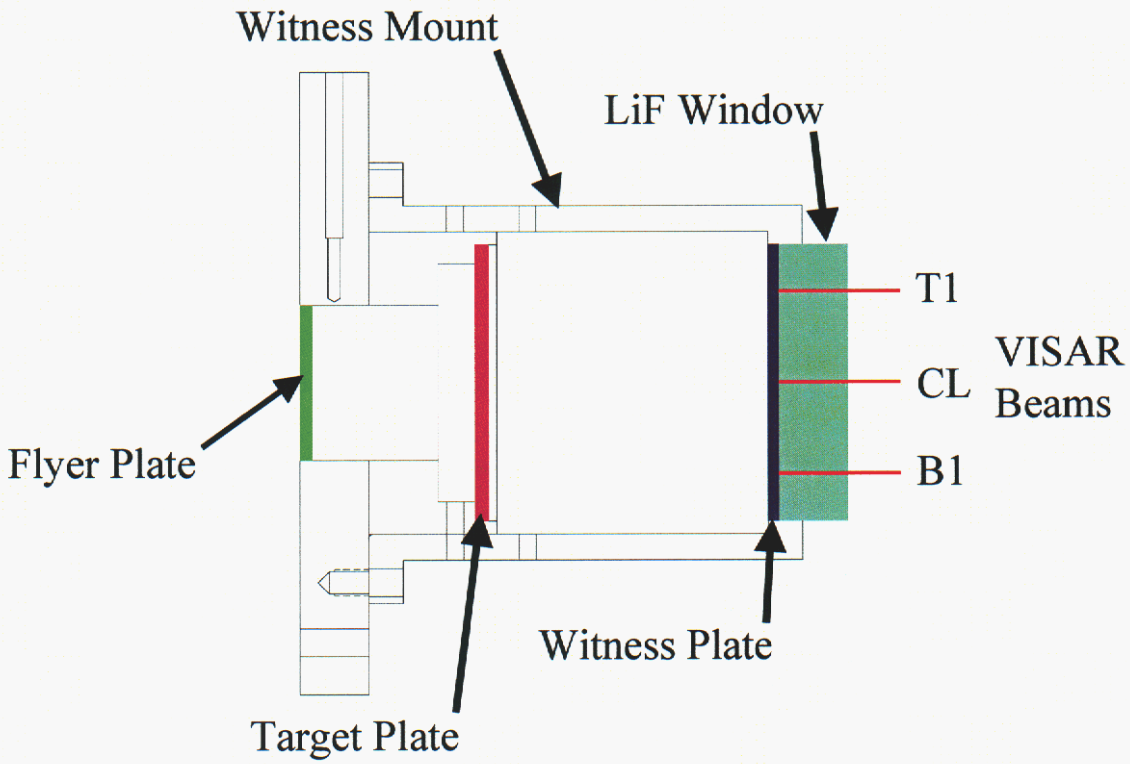

***Figure 2.06**. CLP, 2-D short propagation experimental assembly.*

For 2-D experiments the target and witness plates are mounted directly to the flyer plate barrel. This scheme allows controlling flyer/target/witness plate parallelism through geometric fabrication tolerances of the mounting hardware. The parallelism between the flyer launch position and target plate is <25 μm, and between the target and witness plates is <50 μm. Exact dimensions for each 2-D short propagation experiment are noted in Table 2-1.

The 3-D experiments are very similar to the 2-D experiments except the target plate is tilted 20 degrees off vertical and the witness plate is 7 degrees off vertical. Figure 2.07 shows a cross section schematic of the 3-D experimental setup. Initial experiments in this configuration were done without a witness mount and plate. Subsequent VISAR experiments were performed with a window cut in the witness plate mount to allow radiography of the debris cloud, and VISAR monitoring of the witness plate and LiF window interface. The 3-D experiments have a 1-mm-thick target plate, and 4-mm-thick witness plate when used.

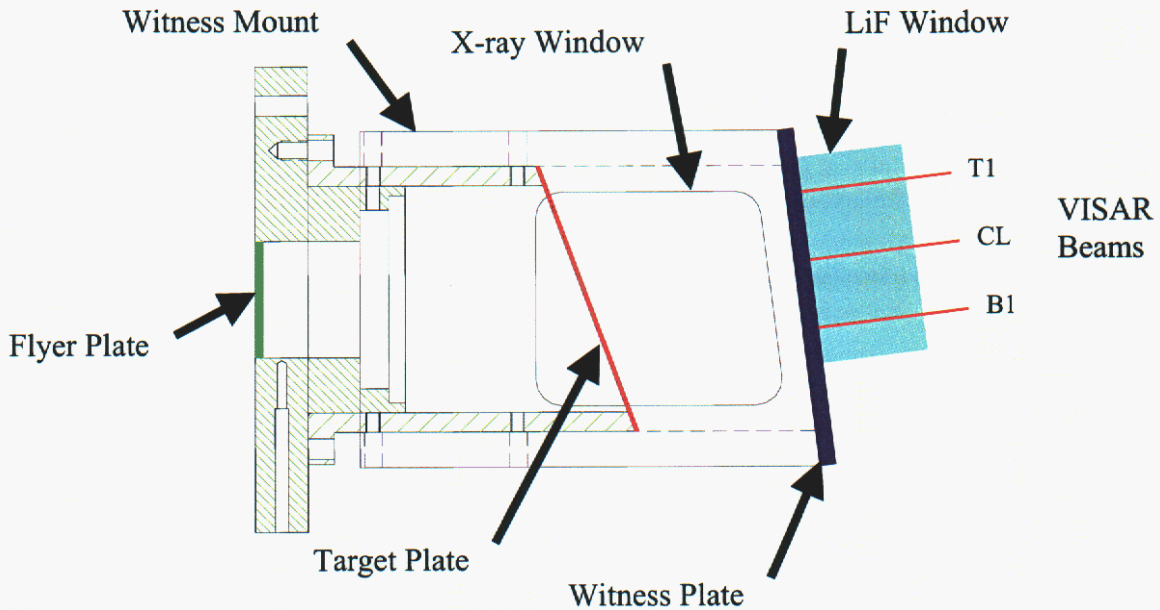

***Figure 2.07**. CLP, 3-D Experimental assembly.*

The as-built and assembled angle on the 3-D target plate was measured at 20 ±0.3 degrees from the radial (vertical) axis, and the witness plate mount was fabricated and assembled with an accuracy of 7 ±0.3 degrees from the vertical axis. The flyer plate to target distance is nominally 77 mm, and the target to witness plate distance is nominally 50 mm. Exact dimensions for each 3-D short propagation experiment are noted in Table 2-2.

2.5 Impact Conditions

Tables 2-1 and 2-2 provide the impact conditions for all experiments. The titanium alloy, Ti-6Al-4V, is used in these studies as a flyer plate because it is known to be fracture resistant and has been launched intact to 16 km/s [10]. Where x rays were not available, estimates for flyer velocity are calculated and are determined to within 1% [25, 26].

2.6 Diagnostics and Precision

2.6.1 Flyer Plate Radiographs

For the flyer-plate long-propagation experiments flyer velocity is obtained from four radiographs, fxr-1 through fxr-4, as shown schematically in Figure 2.05. All flash x-ray heads are Scandiflash model XT-150 with the soft x-ray option installed. The rated pulse width [27] for this system is 30 ns. The flash x ray system is operated in the 120 to 170 keV range. The two horizontal x-ray heads fxr-1 and fxr-2, are used for flyer velocity measurements only. These heads are located 70 cm and 48 cm in front of the target plate. X-ray heads fxr-3 and fxr-4 are an orthogonal pair located 13 cm in front of the target plate. X-ray head location is dictated by the current window port locations in the target-chamber tank wall. The radiograph film cassettes consist of 3-mm aluminum plate armor in the back and front edges, and 1.6-mm Lexan sheet armor over the film exposure area. The film is Kodak DEF 5 with DuPont Quanta Fast Detail intensifier screens. All film cassettes are located inside the target chamber with the x-ray heads located outside, shooting through 6-mm-thick Lexan windows. The distance from the film cassette to the x-ray head is 61 cm.

Flyer-velocity measurements are determined by overlaying static preshot calibration radiographs and the dynamic shot radiographs to measure flyer travel. The static calibration is performed after target alignment. A ¼-20 threaded rod is inserted between the front surface of the flyer and the impact surface of the target. The calibration rod assembly is designed to allow it to be lengthened until the calibration rod is in intimate contact with both the flyer at its starting position and the target center. The calibration rod assembly has position markers strategically placed along the line-of-flight axis. Common reference markers are attached to the target chamber so they will appear in both the static calibration and dynamic shot radiographs and are used for overlay alignment. Figure 2.08 shows a set of (side-view, Y-Z Plane) static calibration radiographs. A static firing of the x ray system is done exposing the film cassettes to the calibration rod located in the flyer experimental flight path. The calibration rod references serve to provide the total length and the distances between the references once removed from the target chamber. All radiograph measurements are done digitally after scanning the negatives at 200 dpi. The distance per digital pixel is determined individually for each x-ray head using the threaded rod as a ruler and counting pixels. Flyer position is determined by overlaying the static and shot radiographs while aligning the common reference markers. Figure 2.09 shows an example of this overlay. Distance from the flyer to each calibration rod reference is then measured in pixels and converted to true distance using the pixels-per-millimeter spatial calibration. Distance between flyer radiographs is then calculated

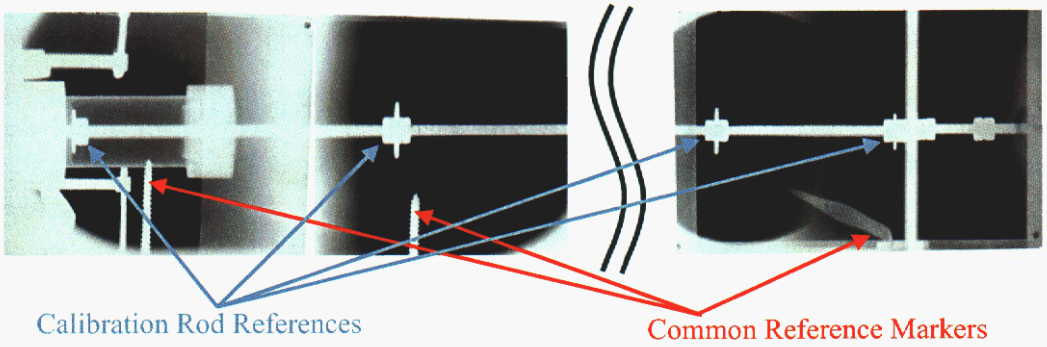

Figure 2.08. *An example of a static calibration determined prior to every experiment. The calibration rod references are used to interpolate the location of the flyer plate and the common reference markers are used for aligning the static x ray with the dynamic x ray for each shot.*

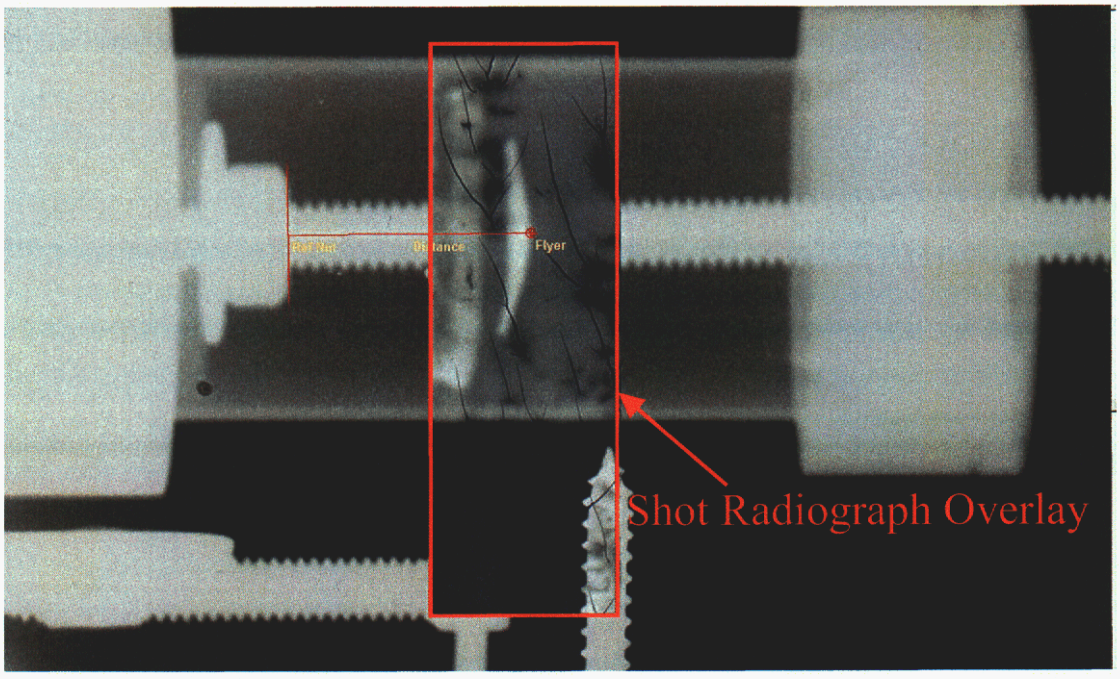

Figure 2.09. *An overlay of the static preshot calibration radiographs with the dynamic shot radiographs to measure flyer travel dimensions, trajectory, and the velocity.*

using the calibration-rod reference measurements. Time between radiographs is determined from x-ray head current monitors recorded on a common time base through a pulse-adding transformer. The flyer velocity is calculated as the change in position between x rays divided by the difference in time between x rays. The accuracy and the uncertainties in these measurements are addressed in a subsequent section.

For the 2-D and 3-D experiments flyer velocity is not measured. The flyer velocity is calculated using 1-D CTH. This calculation is done based on the 2nd-stage projectile velocity, the projectile graded-density impact materials and dimensions, and flyer plate

material and dimensions. With this calculation flyer plate terminal velocity is calculated to within 1% [25, 26] based on previous studies.

Pre-impact flyer plate shape is estimated using the radiographs from the orthogonal x-ray heads fxr-3 and fxr-4 on the long propagation experiments. Flyer shape estimates in two orthogonal planes, the Y-Z plane with fxr-3, and the X-Z plane, are necessary to provide the flyer configuration at impact for numerical simulations. For reporting purposes of this measurement an X,Y,Z axis system as shown in Figure 2.10 is defined with 0,0,0 located at the target plate impact point along the anticipated line of flight, or gun barrel bore trajectory. Three types of estimates can be provided to the numerical analyst: pitch, yaw, and the radius of curvature of the flyer. The flyer pitch and yaw estimates are made for those flyers that do not exhibit appreciable front surface curvature in the radiographs. Flyer radius of curvature estimates are provided for those experiments where the radiograph of the flyer displays a curvature not attributed to experimental anomalies such as flyer location with respect to x-ray source. Flyer impact angle measurements are made from the shot radiographs. The flyer angle is measured as the angle of a line drawn through the flyer major diameter. A pitched down flyer angle θ is negative, and for a yawed down flyer angle φ is negative. Flyer position relative to the centerline identifying the anticipated trajectory is also measured and reported. For radius of curvature measurements, the flyer curved front edge is defined by using 9 to 15 points across its surface and a circle is then fitted to the defining points to get the radius of curvature. Two lines are then defined between the circle center and the top and bottom edges of the flyer. The angle between these lines defines the arc angle of the flyer. Figure 2.11 shows an example of this measurement. The flyer shape is reported as a circle radius location in the experimental X, Y, Z coordinates, and an arc angle with one side of the arc angle referenced to the calibration rod centerline. Figure 2.12 shows an example of the two orthogonal flyer-plate radiographs from x-ray heads fxr-3 and fxr-4.

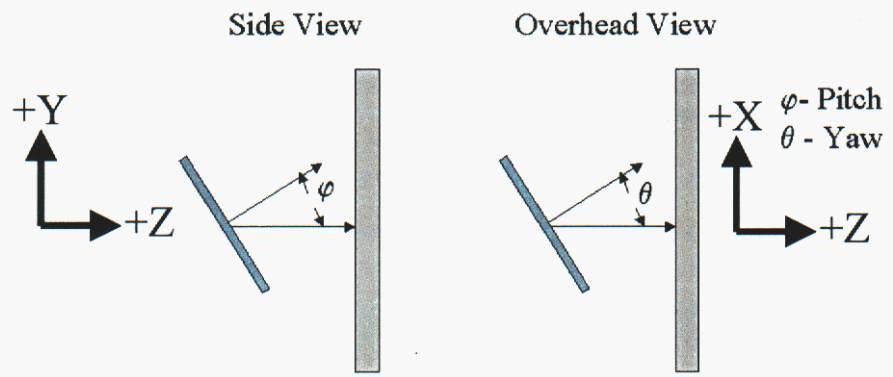

***Figure 2.10**. Reference frame and angles used for reporting flyer shape in long propagation experiments.*

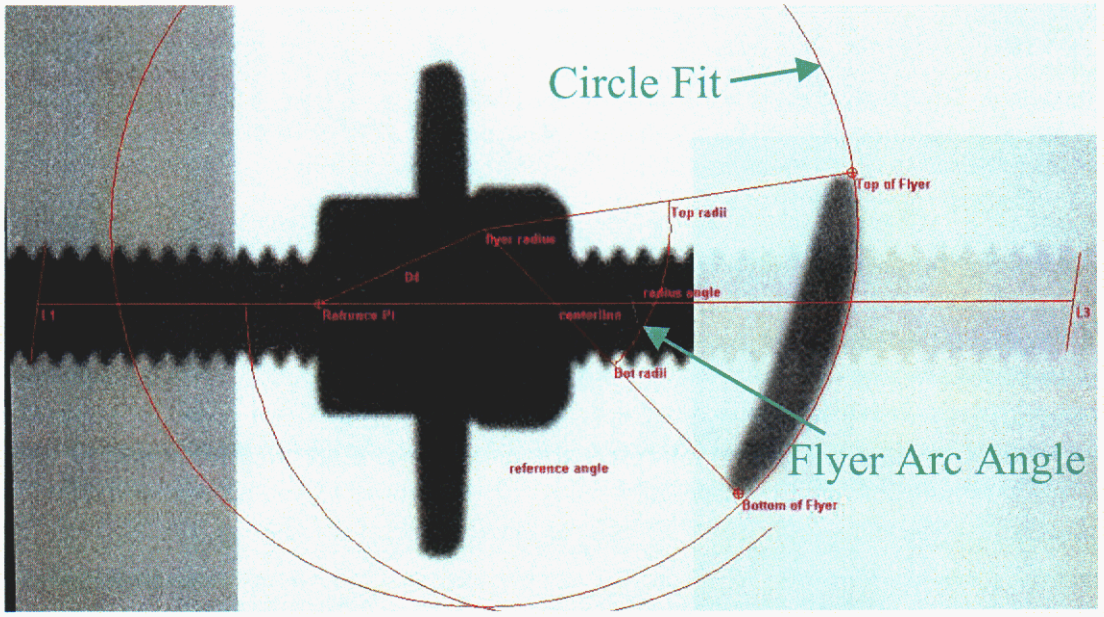

Figure 2.11. *Flyer radius of curvature measurement.*

The analysis of the flyer plate as indicated above defines the worst-case representation of the flyer. This is because the x-ray source subtends a finite angle with the flyer plate in transit, which would shadow an image that is larger than its actual geometric configuration. Unless the x-ray source is exactly normal to the flyer plate this effect cannot be eliminated. No correction was made to the shape of the flyer plate due to geometric shadowing effects.

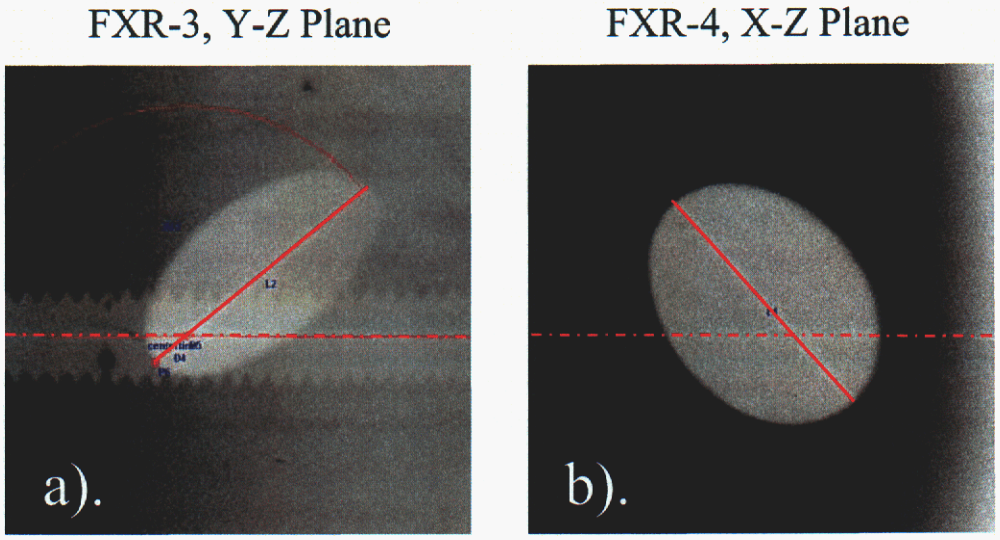

Figure 2.12. *Pre-impact flyer plate shape is estimated using the radiographs from the orthogonal x-ray heads fxr-3 and fxr-4. Flyer shape estimates in two orthogonal planes, Y-Z plane with fxr-3 shown in a), and X-Z plane with fxr-4 shown in b) are necessary to provide the flyer configuration at impact for numerical simulations.*

For the 2-D and 3-D experiments no analysis of the flyer plate pre-impact shape can be made due to the short flyer propagation distance. For this type of experiment the flyer plate is assumed to be planar and normal to the anticipated flight path.

2.6.2 *Debris Radiographs*

Figure 2.13 shows a sample radiograph from the CLP-2 long flyer propagation experiment. Measurement of debris characteristics is based on a static radiograph spatial calibration done using the same methodology described for the flyer measurements. The low-density nature of the debris makes the cloud edge definition in the radiograph very difficult to resolve. Radiograph timing is based on the imaged debris radiograph time relative to the pre-impact radiograph time. In all cases, the radiographs also allow a real-time measurement of the target material hole-size. The hole-size is defined as the debris neck cross section in the debris radiographs as shown in Figure 2.13.

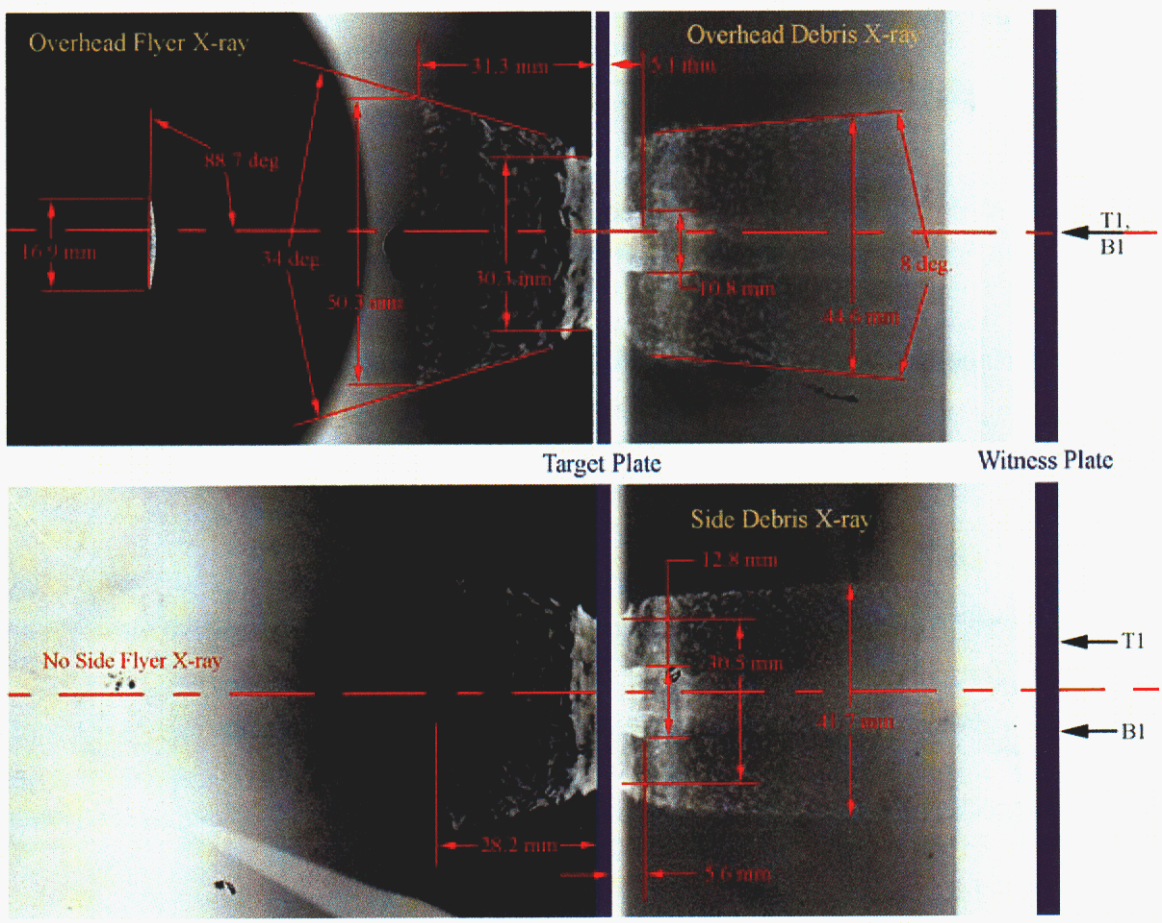

***Figure 2.13**. Experimental radiograph of the aluminum debris resulting from impact of a titanium flyer plate at 6.49 km/s (CLP-2). The first radiograph is taken at 12.2 microseconds after target impact, while the second x-ray is taken 14.3 μs after impact. Notice the collimated density debris shown at the center of the debris cloud. The high-density flyer plate has already impacted the witness plate at this time and is not seen in the radiographs.*

For the 2-D and 3-D experiments debris characteristics are measured in a similar manner. Figure 2.14 shows a sample radiograph from 3-D shot. For these experiments we can obtain a real-time measurement of the hole size in the target plate assuming a circular shape for the hole. Additionally, debris velocity estimates are made on debris front location and timing relative to the VISAR signal time-of-arrival, and/or 2nd stage projectile impact time and calculated flyer velocity. This type of debris velocity measurement assumes a constant flyer plate velocity and instantaneous acceleration. Another example of hole-size and debris-cloud position and velocity measurements obtained from radiographs is shown in Figure 2.15.

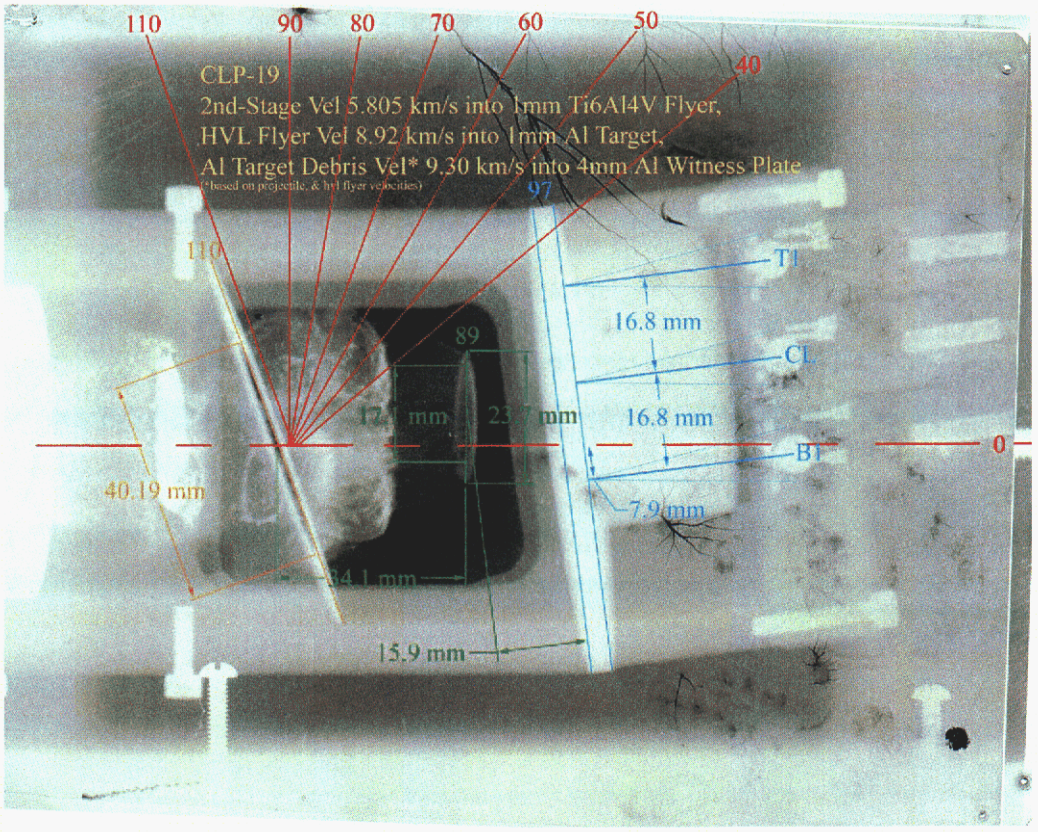

Figure 2.14. *Typical debris radiograph and characterization for 2-D and 3-D experiments.*

Errors in measurements based on radiographs can be attributed to three sources: the timing error, the calibration error, and the measurement error. Timing errors include digital waveform recorders time base error [28], which varies with experiment duration. A typical error number for this measurement is ±0.55 ns for a 40 μs time interval. Another timing error is due to the x-ray exposure duration of 30 ns. Because of this duration, timing of radiographs with respect to non-radiograph events (*e.g.*, correlating with VISAR velocity interferometer records) is ±15 ns with respect to the peak x-ray head current. If we assume all radiograph exposures behave in the same manner, then the 30 ns exposure time is not a contributing factor in estimating the time between different radiographs. The 30 ns x-ray pulse duration, however, will cause approximately 0.3 mm of blurring of the flyer plate while it is in flight.

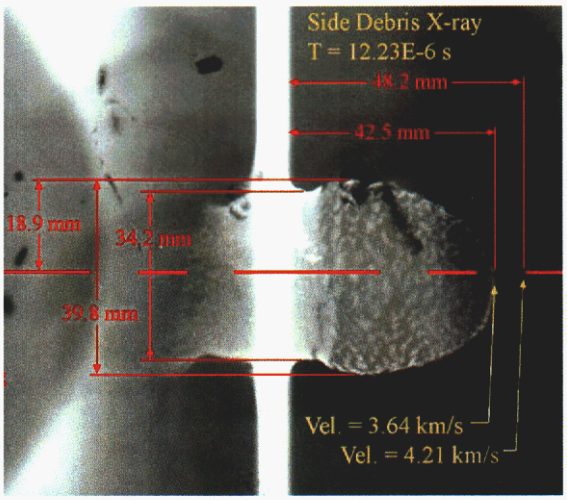

Figure 2.15. *Debris-cloud radiograph taken 12.23 μs after impact. Radiography provides real-time debris characteristics. Target hole size is determined from accurate measurements across the cross section of the debris "neck" in the above radiograph.*

2.6.3 Experimental Measurement Uncertainty

Experimental timing is based on the time at which the flyer impacts the target. To accomplish this a common fiducial is applied to all digital waveform recorders that monitor the VISAR velocity interferometer signals. In addition to the fiducial, the waveform recorders will also record the x-ray monitor pulse. This x-ray monitor pulse is generated from the high voltage pulser output to the flash x-ray tube. Since all the above signals are recorded on the same recorder with the common time base, this allows an extremely accurate time difference between the flyer location prior to impact on the target, the debris cloud x ray, and the arrival of the debris front recorded on the VISAR at the witness plate rear free surface. This is known to within 1 ns. Knowing the flyer position relative to the target (prior to impact), and flyer velocity, the impact onto the target can be determined to better than 100 ns, which corresponds to an accuracy of better than 2% in our timing results. This error is larger than the timing base error because the flyer location prior to impact can be determined only to an accuracy of about 1 mm.

For the 2-D and 3-D experiments all timing is relative to the trigger pins located in the HVL flyer plate launcher. These trigger pins generate a fiducial, which is common to all digitizer records. This provides for common timing between digitized records with an error of ±3 ns.

Some of the calibration errors cannot be quantified and are considered to be quite negligible. Examples of these include:

(1) Variation in the thread pitch of the threaded calibration rod;

(2) Film to x-ray head distance differences between static calibration and dynamic shot film cassettes;

(3) Film to calibration rod versus film to flyer or debris distance differences; and

(4) Scanner resolution uniformity and repeatability.

The film cassettes for the orthogonal x-ray head pairs (to record the debris images) are placed in slots cut in the target witness-plate assembly. This allows for good dimensional repeatability of film placement between static and dynamic radiographs thus minimizing system magnification differences on an experiment. For the flyer-velocity measurements using radiographs, the film cassettes were located in the target chamber, and positioned using physical film stops. In both these instances, the dimensional repeatability of the distance between the x-ray head and the film cassette is estimated to better than 1 mm.

Figure 2.08, previously shown, displays a sample static radiograph for the long-flyer-plate propagation experiments. Measurement error of the calibration rod over the total length of approximately 800 mm is within 0.33 mm. This introduces a velocity measurement uncertainty between the first two and last two flyer radiographs of less than 0.1%. The measurement uncertainty between calibration reference markers located on the reference rod at 33 cm is ±0.013 mm; this is the measurement accuracy of the caliper used. The line of flight in the radiographs is defined by the calibration rod centerline. The calibration rod will sag over the flight dimension of 800 mm and this introduces an error of absolute flyer position relative to the preshot centerline of less than ±1 mm.

Overlaying of the calibration and experimental radiographs is estimated to be better than ¼ of a thread or 0.32 mm. Determining the flyer location with respect to the reference nuts is estimated to be within ½ of a thread or 0.64 mm. Overall, this makes placement of a feature (such as the flyer plate) with respect to the common reference markers at ±0.96 mm.

For 2-D and 3-D shots an angular reference is attached to the calibration rod providing reference angles for analysis purposes. Figure 2.16 shows a sample static radiograph for the 3-D experiments. The angular references are fabricated to ±0.25 degrees. Digital

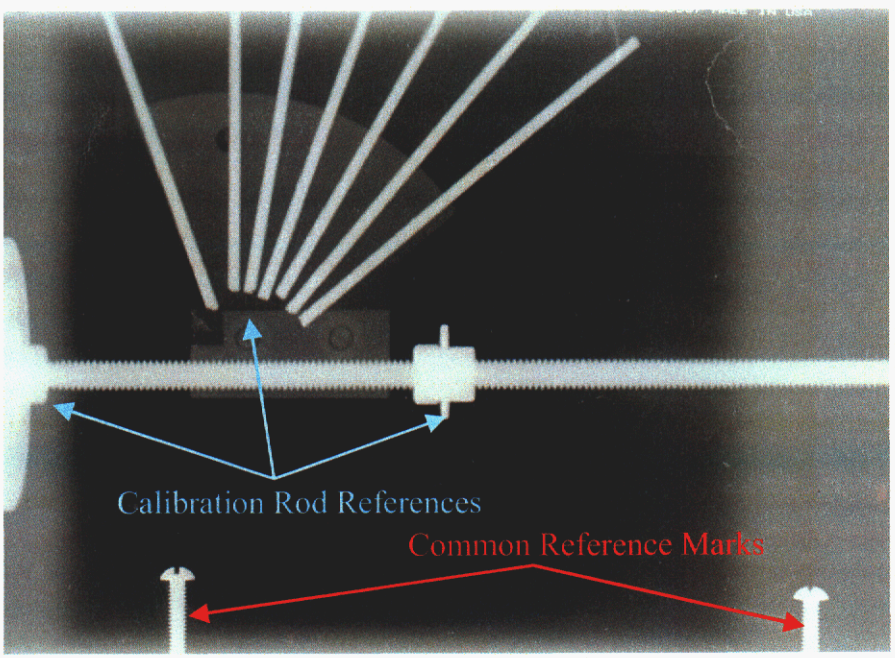

Figure 2.16. *Static radiograph for 3-D experiment.*

measurement of these angles has shown them to be within the fabrication tolerance, hence angular measurements are also within ±0.25 degrees. Linear measurements for these experiments are done with the same precision as discussed above.

2.6.4 *Velocity Interferometry*

Velocity interferometry has become generally accepted as a precision tool for obtaining velocity versus time profiles of the motion of the surfaces of shocked specimens [29]. In a standard VISAR system, the reflected beam from a diffused target is split equally into two beams to form the two different legs of a wide-angle Michelsom interferometer, in which one leg is delayed in time by a period, τ, with respect to the other. Either glass etalons or lens systems are used to introduce a temporal delay in the delay leg of the interferometer, while maintaining the apparent optical path length of the two legs to be the same. When these two beams are superimposed, fringes $F(t)$, are produced in the interferometer and are related to the change in velocity $V(t)$ of the reflecting surface by the relation [30, 31]:

$$V\left(t-\frac{\tau}{2}\right)=(\lambda/2\tau)\,(F(t)/(1+\delta)(1+\Delta\nu/\nu))$$

The wavelength of the light used is λ, and δ is a correction term due to the wavelength dependence of the refractive index of the etalon material (δ = 0.034 at 514.5 nm when fused silica etalons are used to achieve the necessary delay, or δ = 0 when a lens combination is used). The optical correction term $\Delta\nu/\nu$ results from the change in refractive index of the window material with shock stress. If measurements are made at a free surface, $\Delta\nu/\nu$ is 0. $\Delta\nu/\nu$ for a variety of windows will change according to the refractive index of that particular window material. For the lithium-fluoride windows used in this study $\Delta\nu/\nu$ is estimated to be 0.28 [32].

The VISAR [25] system incorporates quadrature coding to eliminate ambiguity in the sign of acceleration and to improve fringe resolution. The two-quadrature fringe signals allow an unambiguous determination of velocity increase versus a velocity decrease. This is accomplished by adding a quarter-wave retardation plate, and a polarizing beam splitter to separate the two fringe signals 90° out of phase. These fringe signals are recorded with the aid of photomultiplier tubes. The VISAR has an accuracy of ~2% for peak surface velocities of ~0.1 km/s, assuming one fringe is recorded. Much better accuracy is obtained as surface velocities are higher and more fringes are obtained. A significant improvement to the standard VISAR [25] has been made that has the effect of increasing the fringe signal amplitude [33], while eliminating time-dependant beam-intensity signals due to incoherent light sources generated during the experiment. This is referred to as a push-pull VISAR.

3. Results

Radiographic measurements of the debris generated upon impact of the target plate are shown in Figures 3.01a, 3.01b, and Figure 2.15 for the experiments at about 11, 9, and 6.49 km/s, respectively, for normal impacts. For oblique impacts where the target is inclined at 20 degrees from the vertical, the radiographs of the debris are shown in Figures 3.02a and 3.02b at impact velocities of 11 and 9 km/s, respectively. The velocity histories resulting from the debris cloud loading on the witness-plate for experiments conducted at 6.5, 9, and 11 km/s are shown in Figures 3.03, 3.04, and 3.05, respectively. The particular experiment is identified in the figure caption, while the exact experimental configurations are given in Tables 2-1 and 2-2. At impact velocities from 6.5 km/s to 11 km/s, the stress states achieved in the aluminum target will vary from 100 GPa to about 230 GPa. Melting is initiated at a shocked stress of about 120 GPa and is complete by around 140 GPa [34, 35]. In either case, the target plate will be totally molten upon release.

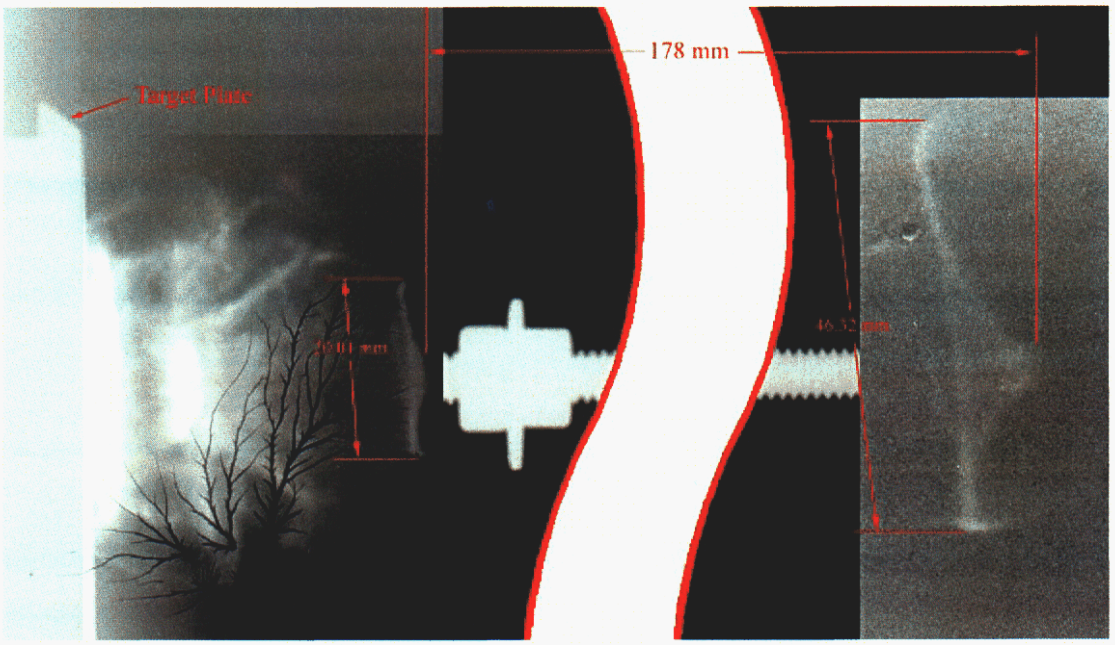

***Figure 3.01a**. Experimental radiograph of the aluminum debris resulting from impact of a titanium flyer plate at 11.04 km/s (CLP-12). The first radiograph is taken at 40 mm from target impact. The high-density debris shown close to the muzzle is the debris from the titanium flyer plate.*

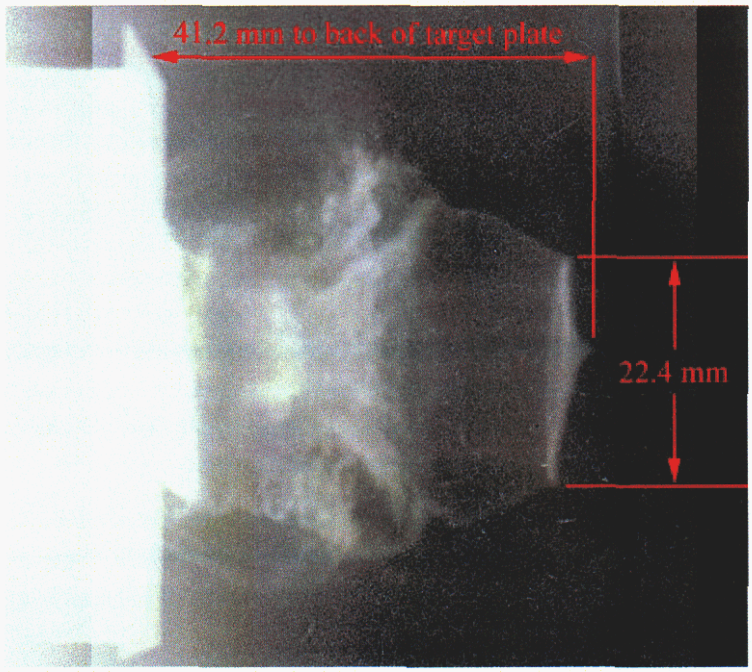

Figure 3.01b. *Experimental radiograph of the aluminum debris resulting from impact of a titanium flyer plate at 8.71 km/s (CLP-13). The first radiograph is taken at 41.2 mm from target impact. The high-density debris shown close to the muzzle is the debris from the titanium flyer plate. Only one x ray is available for this experiment.*

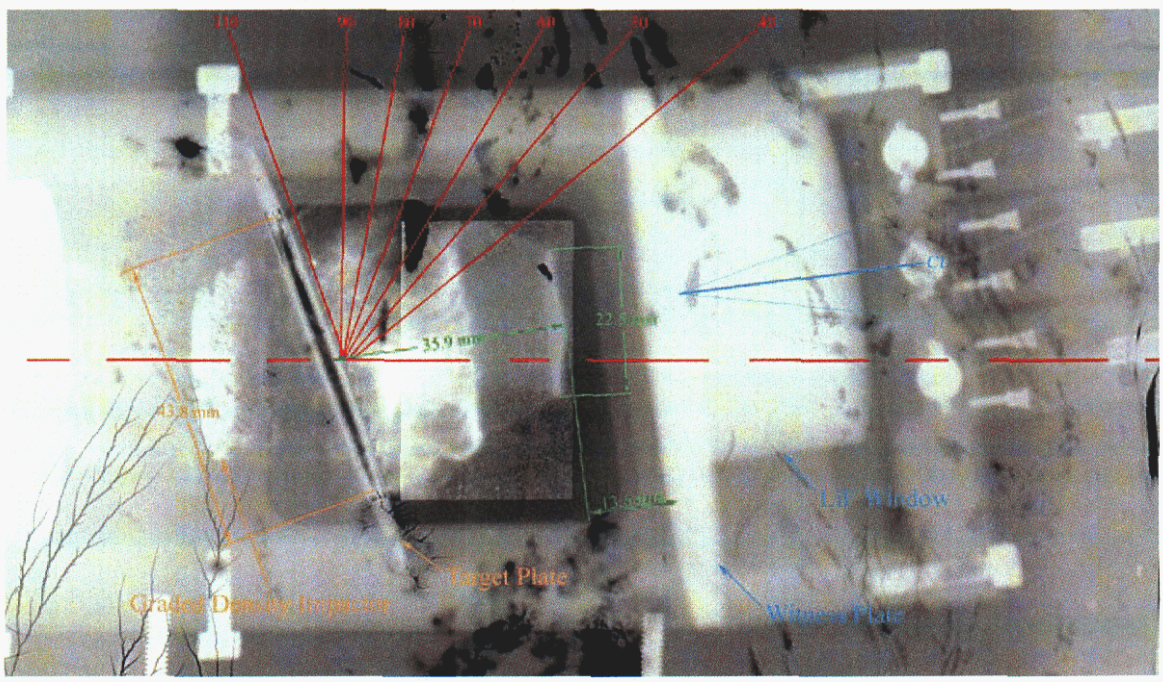

Figure 3.02a. *Experimental radiograph of the aluminum debris resulting from impact of a titanium flyer plate at 11.14 km/s (CLP-21) on an aluminum target that is inclined at 20° from the vertical. The radiograph is taken at 35.9 mm from the center of the target after impact. The high-density debris shown close to the muzzle is the debris from the titanium flyer plate.*

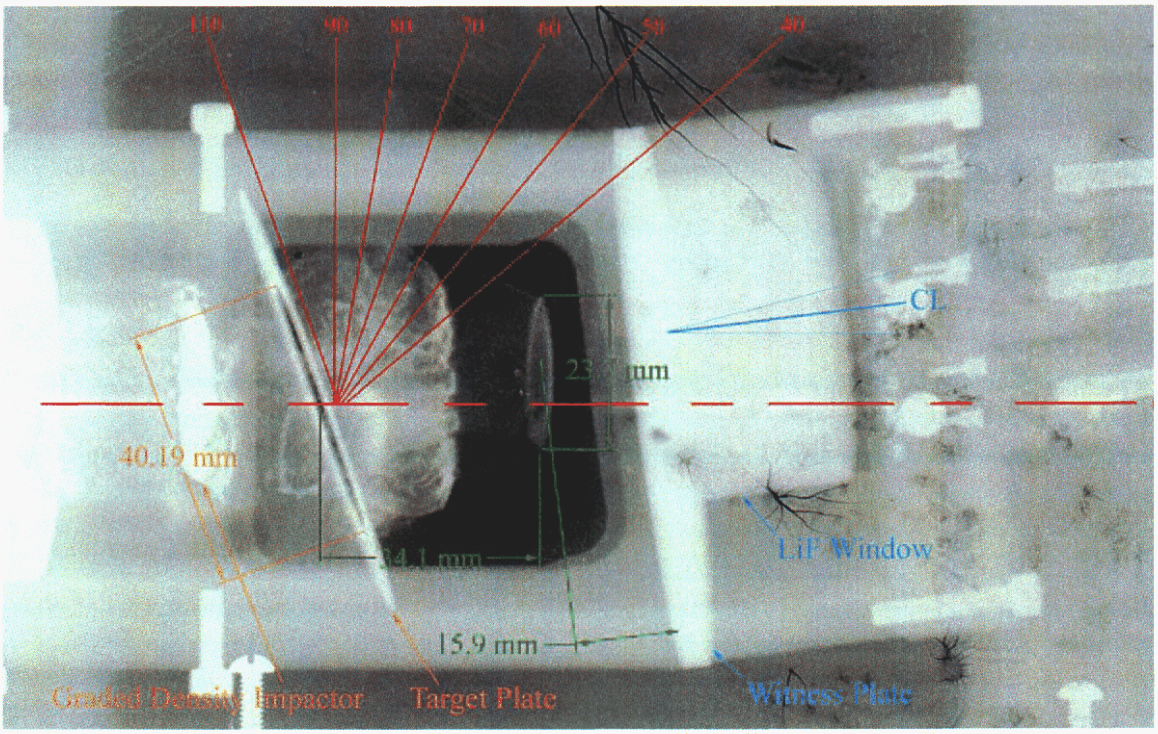

***Figure 3.02b**. Experimental radiograph of the aluminum debris resulting from impact of a titanium flyer plate at 8.92km/s (CLP-19) on a aluminum target that is inclined at 20 degrees from the vertical. The radiograph is taken at 34.1mm from the center of the target after impact. The high-density debris shown close to the muzzle is the debris from the titanium flyer plate.*

3.1 Experiments at ~6.5 km/s: CLP-2 and -20

CLP-2 and CLP-20 are experiments conducted at approximately 6.5 km/s. At this impact velocity, the debris is a molten plate that traverses the gap prior to impacting the witness plate. The radiograph for experiment CLP-2 (Figure 2.13), which triggered late, nevertheless shows a symmetric center column of aluminum debris suggesting a flat-plate 2-D impact. This is corroborated by the velocity history measurements in experiment CLP-2 where a peak free-surface velocity of 1.2 km/s is measured at two different locations approximately 7.5 mm away from the center of the witness plate (Figure 3.03a). Since the witness plate is 4-mm thick an attenuating wave propagates through the witness plate; this results in free-surface spallation when the stress wave arrives and reflects at the free-surface, preventing a measurement of the attenuating release structure. To prevent surface spall of the witness plate, a lithium-fluoride window is attached to its back surface as indicated in Figure 2.06. The velocity history record for experiment CLP-20 is shown in Figure 3.03b. As shown in the figure, a peak particle velocity of ~0.6 km/s followed by a full release is observed at the center of the target plate. This signature is representative of an attenuating wave that would result from impact of a thin flyer on a thick target plate. (A peak particle-velocity measurement of twice this value, or 1.2 km/s, would have been obtained at the free surface.) The main conclusion from these two 2-D experiments at impact velocities of 6.5 km/s is that the resultant debris is a relatively flat molten plate having a finite thickness.

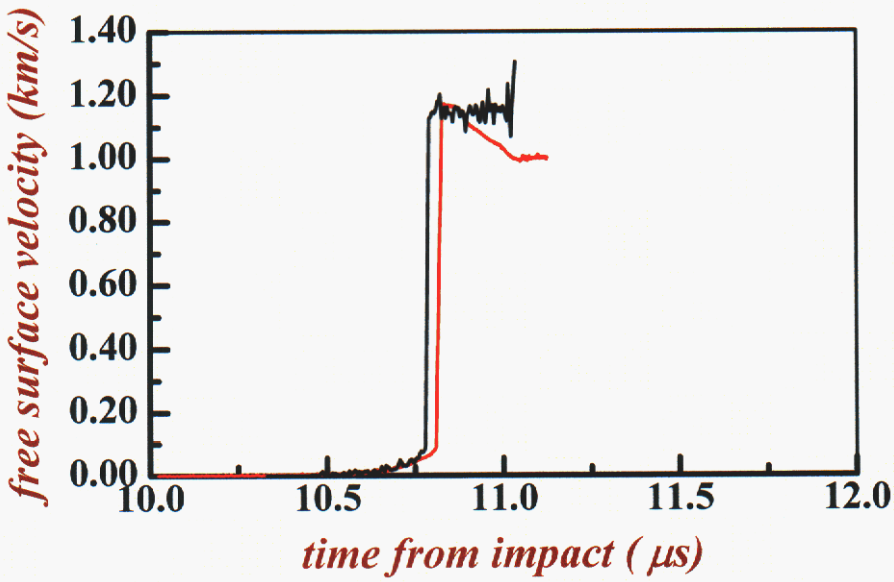

Figure 3.03a. *Velocity records for experiment CLP-2 at locations plus or minus 7 mm from the center of the witness plate.*

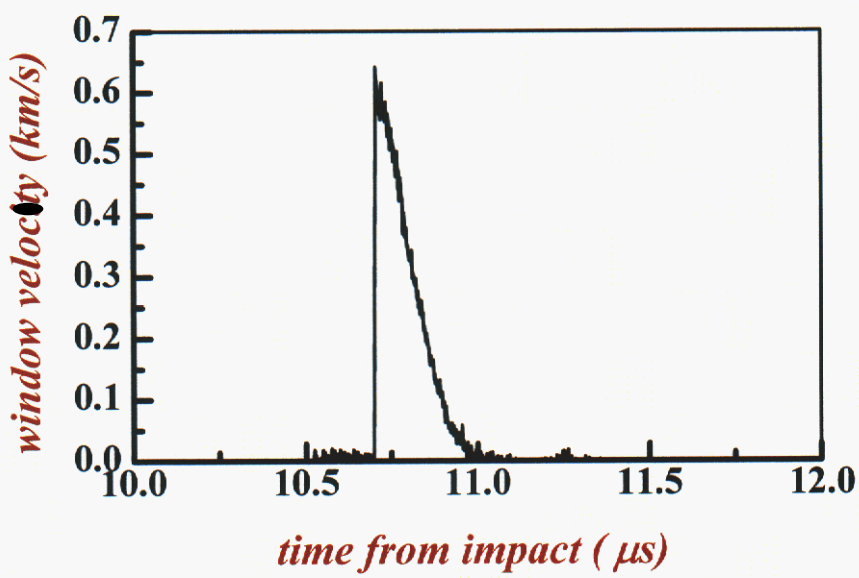

Figure 3.03b. *Velocity record for experiment CLP-20 monitored at the center of the witness plate.*

These experiments also provide the velocity at which the impact generated debris traverses the gap. This is obtained by correlating the impact time of the aluminum target plate to the time of arrival of the loading history on the aluminum witness plate as measured by the velocity interferometers. For these experiments a debris propagation velocity of 7.5 km/s is obtained.

3.2 Experiments at ~9km/s: CLP-3, -6, -13 and -14

At an impact velocity of ~9 km/s, the aluminum target would be shocked to 170 GPa, and will be totally molten in the shocked state and upon immediate release. Upon further expansion, the debris products are expected to be a mixture of liquid and vapor phase (see Figure 1.01) as the debris traverses the gap. Radiographic measurements of the debris (experiment CLP-13) shown in Figure 3.01b suggest that the resultant debris is primarily an intact plate even though it has traversed approximately 41 mm from impact. The plate debris appears to have expanded to 22.4 mm in diameter from its original diameter of 17 mm. This would suggest that the density of the plate-like debris is approximately 1.6 gm/cm^3 provided the thickness of the target plate remains the same. There is also clear evidence of collimated aluminum debris behind the plate. It is not as distinct as shown in the radiograph in Figure 2.16, taken at an impact velocity of 6.5 km/s. This is because the current radiograph in Figure 3.01b is imaged early, ~4 μs after impact, and is not separated sufficiently from the flyer-plate titanium debris resulting from impact.

The loading history resulting from the interaction of this debris with the witness plate is given in Figure 3.04 for experiments CLP-3, CLP-6 and CLP-14, respectively. The exact impact conditions are summarized in Table 1. In experiment CLP-3, three velocity interferometer probes were located over the diameter of 4 mm at the center to monitor the surface motion at the witness plate/window interface. As indicated in Figure 3.04, the peak amplitudes and the release structures are very similar. This suggests uniform loading at the center by *plate-like debris* having a finite thickness. Similar profiles are also seen in experiments CLP-6 and CLP-14. In experiment CLP-6, the peak amplitude is higher because the debris is allowed to propagate about 23 mm before it stagnates against the witness plate, whereas in experiment CLP-3 the *debris plate* propagates ~50 mm. The average density of the debris plate is expected to be higher and well-

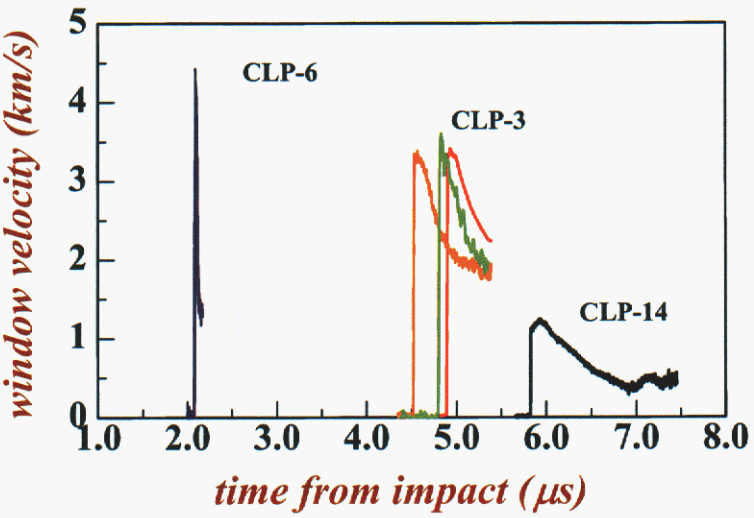

Figure 3.04. *Interface velocity history records of the witness plate in experiments CLP-6 and CLP-14 respectively are at the center of the witness plate. The three profiles for experiment CLP-3 are at the center, and plus or minus 2 mm off center locations on the witness plate.*

defined for shorter propagation thickness. As the debris plate propagates further, due to radial expansion and also due to time-dependent vaporization/expansion kinetics, the average density of the debris will be lower. Wave attenuation effects in the 5.6-mm-thick witness plate dominate the interface velocity history measurements in experiment CLP-14.

3.3 Experiments at ~11km/s: CLP-4, -12, -15, and -22

At an impact velocity of ~11 km/s, the aluminum target is shocked to about 220 GPa, and will be totally molten in the shocked state and upon immediate release. Upon further expansion, the debris products are expected to be a mixture of liquid and vapor phase (See Figure 1.01) as the debris traverses the gap. The vapor fraction compared to the liquid fraction is expected to be higher at an impact velocity of 11 km/s compared to 9 km/s. Radiographic measurements of the debris (experiment CLP-12) shown in Figure 3.01a suggest that the resultant debris is primarily an intact plate even though it has traversed approximately 41 mm from impact point. The plate debris appears to have expanded to 20 mm in diameter from its original diameter of 17 mm. This would suggest that the density of the plate is ~1.9 gm/cm^3 if the thickness of the target plate remains the same. At a propagation distance of about 220 mm beyond impact its diameter has expanded to over 45 mm yielding an average density for the plate of about 0.44 gm/cm^3. What is most surprising from this result is that the high density region of the debris resembles a plate even though it has propagated over 220 mm. It's lateral expansion velocity is determined to be 2.0 km/s compared to its axial velocity of 13.2 km/s. The leading edge, where there appears to be a *bow*, is where the vaporization process is presumed to dominate; along the edges the rate of vaporization is lower—suggesting a heterogeneous vaporization process. Since the debris appears to resemble a plate of finite thickness, as opposed to a vapor cloud, it is quite likely that effects due to *super-cooling* are playing a significant role.

The loading history resulting from the stagnation of the debris against the witness plate is shown in Figure 3.05a and Figure 3.05b for experiments CLP-22 and CLP-4, respectively. The peak particle velocities are very similar if you consider that the witness plate dimensions are not the same in the two experiments. The debris generated in these experiments at impact velocities of 11 km/s are typical of those that result from thin plate impacts. This is consistent with what is observed in experiment CLP-12 where *plate-like debris* is imaged by x rays after a propagation distance of 50 mm. However, in a similar experiment, CLP-15 (Figure 3.05c), the signature and the peak particle velocity measured are totally different. The loading history includes a time-dependent ramp loading followed by a shock. The early ramp loading is caused by the presence of a lower density vapor cloud that precedes the higher density liquid, which results in shock loading at the witness plate. In this experiment, it appears therefore that the constituents of the debris included a larger mass fraction of vapor compared to liquid—unlike the results depicted for experiments CLP-4 and CLP-22. The lower peak particle velocity measurements in experiment CLP-15 are due to the witness plate interaction with a relatively lower average density debris cloud.

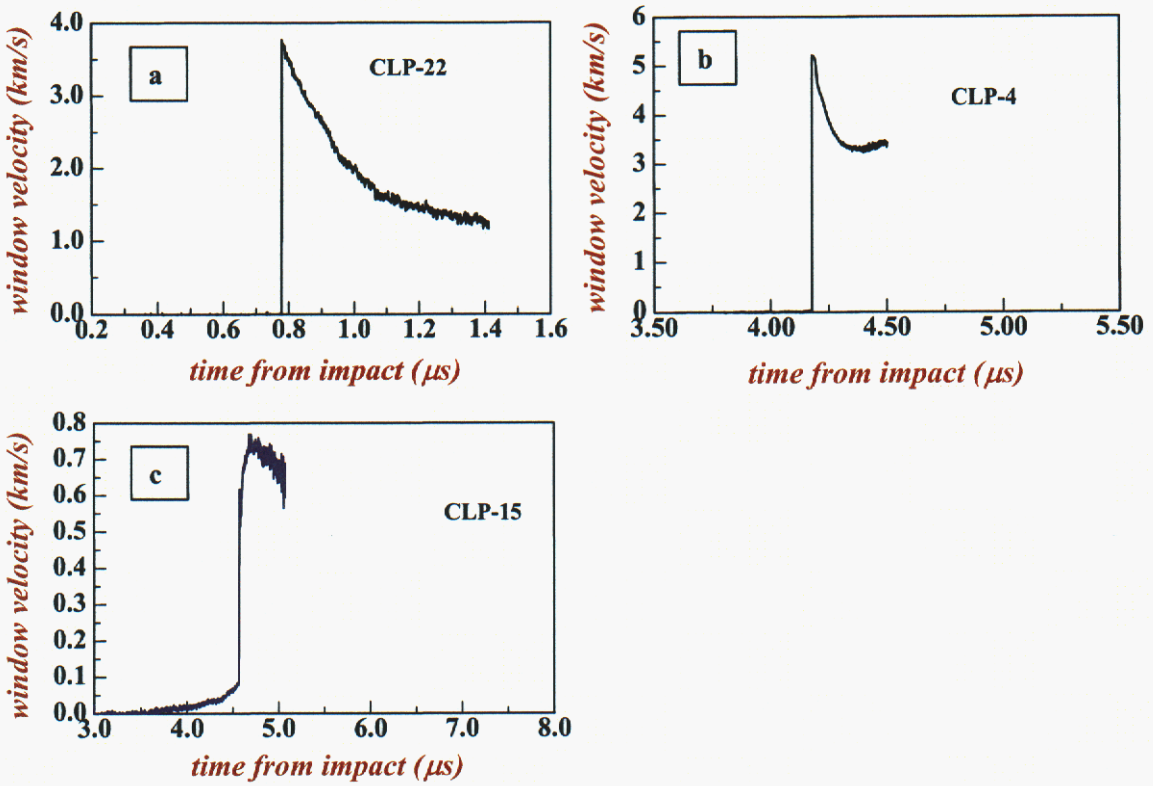

Figure 3.05. *Interface particle velocity profiles at the center of the witness plate for experiments CLP-22, CLP-4 and CLP-15 are shown in a), b), and c) respectively.*

3.4 Inclined Impact Experiments at ~9 and 11km/s: CLP-19, -18, and -21

In these experiments the aluminum target is tilted 20 degrees from its vertical axis (see Figure 2.07). The titanium flyer impacts the target at ~9 km/s in experiment CLP-19, and at about 11 km/s in experiments CLP-18 and CLP-21, respectively. As shown in Figure 3.02b for CLP-19 the aluminum debris is *plate-like* and appears to be traversing along its original flight path. The loading resulting from the interaction of the debris plate with the witness plate is shown in Figure 3.06a. The velocity history at the witness-plate/window interface is indicative of an attenuating wave that has traversed through the witness plate. This is consistent with the earlier deduction that the debris in the form of a thin plate impacts the witness plate. Similar results are obtained for experiment CLP-21. The radiograph in Figure 3.02a indicates plate-like debris for this experiment, and the particle velocity history at the interface in Figure 3.06b also suggests impact by a thin plate. However, in a similar experiment, CLP-18, the signature and the measured peak particle velocity is totally different. As indicated in Figure 3.07a, the loading history includes a time-dependent ramp followed by a shock. The early ramp loading is due to a lower density vapor cloud that precedes the higher density liquid that causes the shock loading. The shock does not overtake and steepen up the ramp even though the witness plate is sufficiently thick. In this experiment, it appears that the mass constituents of the debris included more vapor and less liquid, unlike the results depicted for experiments CLP-19

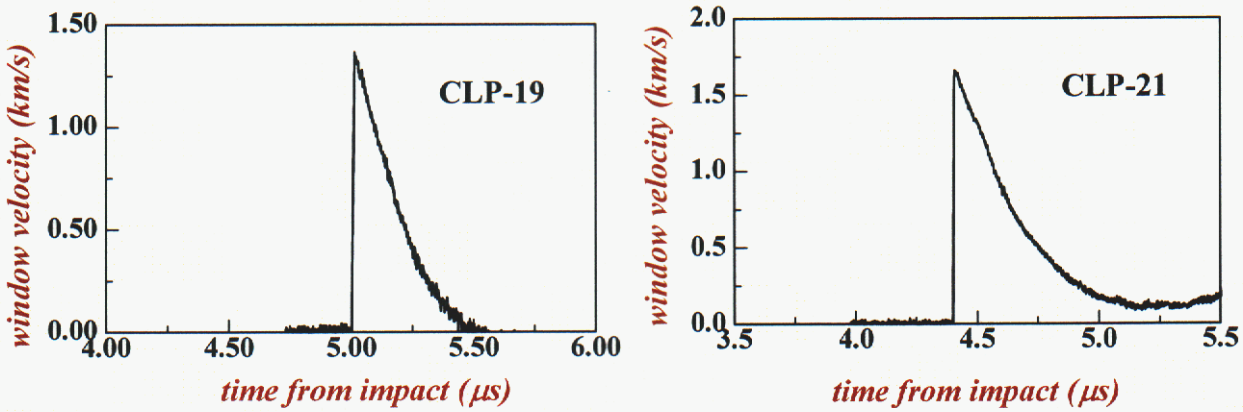

Figure 3.06. *Witness plate particle velocity history from oblique impact experiment CLP-19 at 9 km/s is shown in (a) and for CLP-21 at 11 km/s is shown in (b).*

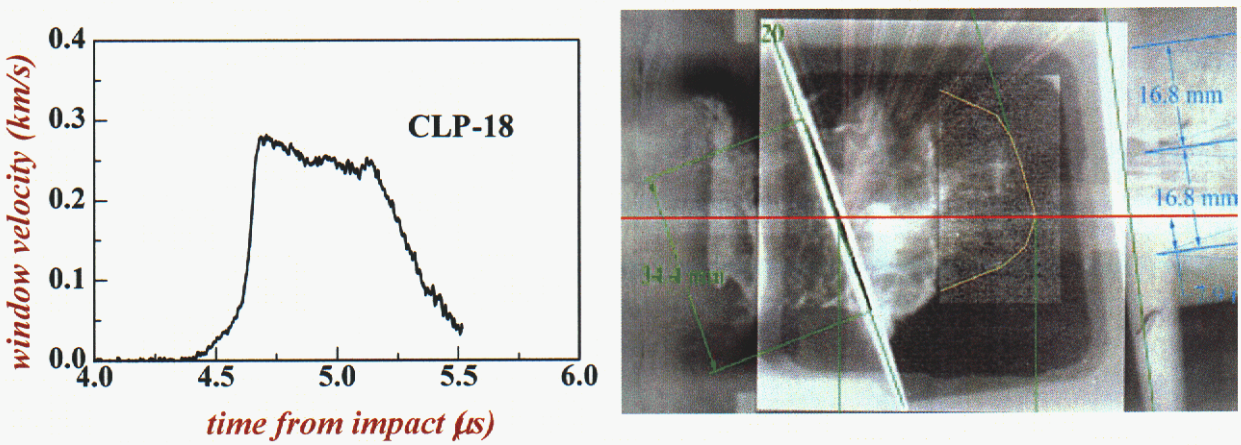

Figure 3.07. *Witness plate particle velocity history from oblique impact experiment CLP-18 at 11 km/s is shown in (a) and the corresponding radiograph of the debris is shown in (b).*

and CLP-21. The interaction of the lower average-density of the debris cloud with the witness plate in experiment CLP-18 results in peak particle-velocity measurements that are significantly lower than those caused by a *plate*. This is confirmed by the corresponding radiograph record (Figure 3.07b) that imaged the debris prior to its interaction with the witness plate. As indicated in the radiograph, the debris is not a plate but appears to have lower density features suggesting the presence of a liquid-vapor mixture.

3.5 Dependence of Witness-plate Velocity Measurements on Stand-off Distance

In these experiments, the debris generated upon impact propagates a certain stand-off distance before it is allowed to stagnate against an aluminum witness plate. The resultant loading features are determined at the witness-plate/window interface as interface velocity measurements. Figure 3.08 shows the variation of the interface velocity measurement as a function of stand-off distance in the experiments at 9 and 11 km/s. In the figure, the velocity measurements have been normalized to the interface-velocity

estimate that would have been obtained for zero stand-off distance. Since the impact conditions are well known, the interface-velocity value at zero propagation distance can be calculated very accurately. The change in the velocity measurement from the zero-gap propagation distance measurement is directly related to the degree of vaporization resulting from time-dependent vaporization process. This is also consistent with the x-ray measurements shown in Figure 3.01, which also show a lower density debris as a function of propagation distance.

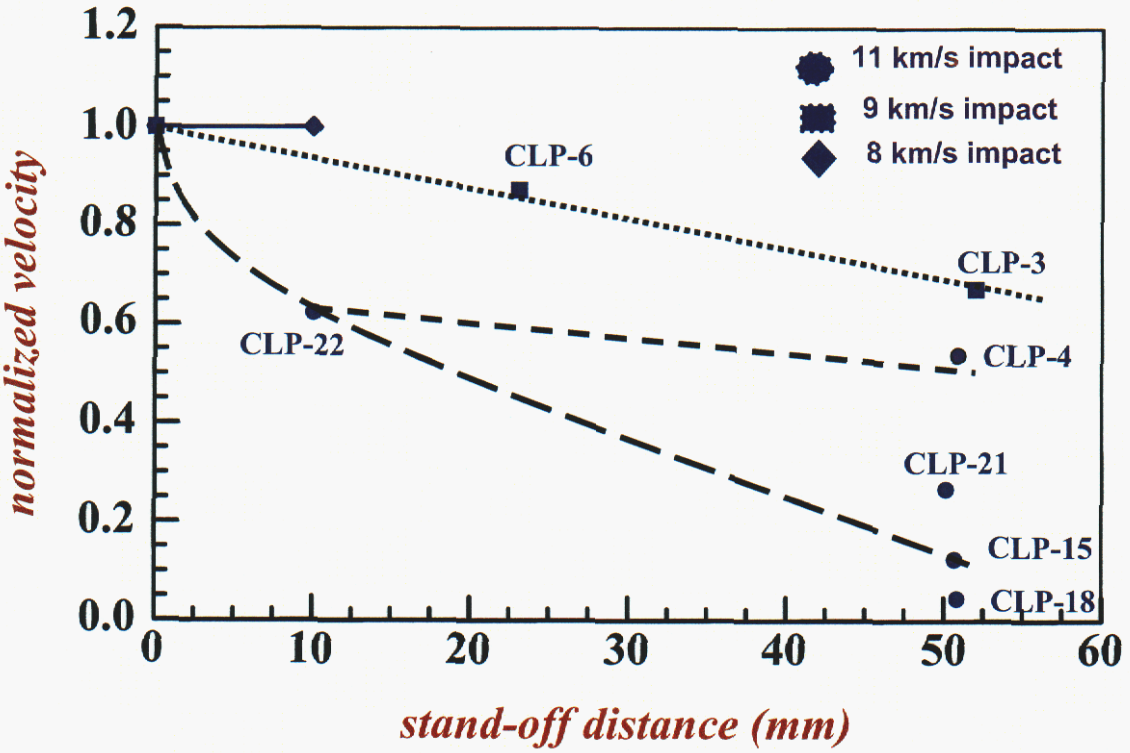

Figure 3.08. *Variation of normalized witness plate velocity with debris propagation distance.*

Intentionally Left Blank

4. Discussion of Experiments

4.1 Previous Studies

Similar studies were previously performed on porous aluminum [6] at impact velocities up to 7.5 km/s, to a shock stress of about 0.8 Mb, and the debris products were allowed to propagate a gap of 10 mm before stagnating against an aluminum witness plate/lithium-fluoride window. The results of these studies indicate that little or no vaporization occurred even though porous aluminum was used to increase shocked temperatures in the samples. These experiments also suggested that the witness plate velocity did not change with propagation distance, indicating that no measurable vapor was present. Results of one experiment on solid aluminum at an equivalent impact velocity of 8 km/s and shocked to a stress of 1.4 Mb also indicate no vaporization and no change in particle velocity after a propagation distance of 10 mm. These latter results are included in Figure 3.08.

4.2 Radiographic Measurements

We have imaged the debris at both normal and inclined impact velocities of 9 km/s and 11 km/s. *Plate-like* debris is observed, even at impacts on targets inclined at 20° from the vertical for propagation distances of the order of 50 mm. Since the debris is a plate of finite thickness, as opposed to a vapor cloud, it is quite likely that effects due to *super-cooling* are playing a significant role. This indicates time-dependent vaporization kinetics and is due to *heterogeneous* vaporization processes; this is further evidenced by radiographic measurements at 11 km/s that show *plate-like* debris in experiment CLP-21 and *vapor-like* debris in experiment CLP-18. The measurements, therefore, suggest that the threshold for vaporization kinetics in aluminum becomes significant when the material is expanded from shocked states over 230 GPa. At shocked stresses below 230 GPa, effects due to super cooling and time-dependent vaporization kinetics dominate the expansion process. In other words, vaporization does not occur instantaneously. To properly model these experiments, explicit treatment of boiling kinetics may be necessary—a result that has been deduced from shock-induced vaporization studies in other metals such as zinc and lead [2-5].

4.3 Witness-plate Particle-velocity Measurements

The aluminum witness-plate/lithium-fluoride window can be regarded as a target with which the liquid/vapor debris interacts. The peak interface-velocity measurement is an indicator of the maximum stress resulting from this interaction (Figures 3.03, 3.04, and 3.05). The measured peak velocity increases with increasing impact velocity over the range from 6.5 to 11 km/s, which suggests a lack of significant vaporization occurring over the stress regime of 100 GPa to 230 GPa. This also means that the debris interaction with the witness plate increases. *What is more significant is that the stress resulting from this interaction span over 1 Mb to 2 Mb for the experimental geometry and impact conditions used in this study.* Particle-velocity histories that indicate loading and

immediate release are signatures that are typically obtained by thin-plate impacts. Evidence of leading vapor debris, if any, is overdriven by the high-amplitude shock caused by the subsequent interaction of the high-density liquid plate. For normal and inclined experiments at 11 km/s, in addition to the thin-plate impact signatures, ramp loading followed by lower amplitude shocks are also observed (experiments CLP-15, CLP-18, CLP-21). In these experiments, significant vaporization causes the precursor ramp loading; the subsequent shock, which is of a lower amplitude (than plate-like impact), is due to the interaction of the lower density liquid debris with the witness plate. The implication is that the *vapor debris* has both density and velocity gradients that are spread over larger dimensions compared to the *plate-like* debris. The results are consistent with those obtained from radiographic measurements, namely that the threshold for vaporization kinetics in aluminum becomes significant when it is expanded from shocked states over 230 GPa.

Figure 3.08 shows the variation of the witness-plate velocity measurements as a function of stand-off distance in the experiments at 9 and 11 km/s. The witness-plate velocity measurements have been normalized to the velocity estimates that would have been obtained for zero stand-off distance. The change in the velocity measurement from the zero-gap propagation distance value is directly related to the degree of vaporization resulting from time-dependent vaporization process. When there is no change in particle velocity measurement, which is indicated for the experimental results at 8 km/s, there is no vaporization and the interaction of the debris with the witness-plate will be independent of the gap size. This is reasonable because the debris travels as a molten plate and is not changing its density since there is no vaporization. However, as the impact velocity is increased, there is a decrease in witness plate particle-velocity measurement suggesting that the interaction stress is decreasing with increased gap distance. For the experiments at 9 km/s, a 2-mm-thick witness plate is used, while a 4-mm-thick witness plate is used in the11 km/s experiments. The rate of attenuation is steeper in the 11 km/s experiments, which is why there is a substantial decrease initially from 0 to 10 mm stand-off propagation distance. There is considerable *scatter* in the normalized velocity ratio as the stand-off is increased to 50 mm. This is due to the *time-dependent* and *heterogeneous* boiling kinetics as the material is at the threshold of vaporization phenomena. In experiment CLP-4, where there is practically no change in the normalized velocity ratio, super cooling is dominating. Experiments CLP-15, CLP-18, and CLP-21 suggest that the vaporization phenomenology is heterogeneous as indicated by the increased variation in the velocity ratio measurement for the 50 mm gap distance.

5. A Preliminary Computational Analysis

Throughout the course of this project we used the multi-dimensional Eulerian hydrocode CTH to analyze many different aspects of the dynamic response of the various experimental configurations. We wanted to conduct a numerical analysis early in the project to obtain an initial idea of the level of detail that we would need to reproduce in the numerical simulations. Another purpose was to see if there were any unanticipated problems, with the numerical techniques, with the equations of state, or with our other assumptions regarding the modeling of the basic physical configurations.

All of the experiments conducted here are very similar. They all involve flyer plates that impact stationary thin targets at velocities between 6 and 11 km/s. This leads to target penetration and the formation of debris clouds that propagate downstream behind the target, and eventually stagnate on witness plates. The response of the witness plates is characterized in terms of velocity measurements from its rear surface, either as a free surface or as an interface with a transparent window material. For this preliminary analysis we chose a 0.8-mm-thick titanium alloy (Ti-6Al-4V) flyer plate, and allowed it to impact a 2.4-mm-thick 6061-T6 aluminum target at a velocity of 6.5 km/s. Experimental x rays suggest that the flyers have little or no pitch or yaw, but that at impact they might have a warped shape with a finite radius of curvature. A 6061-T6 aluminum witness plate (4 mm thick) was placed 75 mm downrange of the target. For these calculations we did not include a window on the back of the witness plate. This configuration is similar to that shown in Figure 2.04.

This early analysis provided an opportunity to perform an in-depth evaluation of the CTH code for modeling this class of problem. This study incorporated the following:

(1) Modeling the problem in 2-D axisymmetry:

(a) Investigate the important physics related to this class of problems;

(b) Perform a mesh sensitivity study to investigate the influence of mesh resolution on the analysis; in particular, the effect of zoning on quantities used for comparison with experimental data (*e.g.*, plate hole diameters, debris cloud evolution, and specific velocity histories);

(c) For a fixed mesh, examine the influence of flyer geometry, *i.e.*, examine differences resulting from modeling the flyer as a flat circular disk (the ideal problem) versus a warped geometry (the configuration actually observed in long-throw experiments); and

(d) Assess the implications of the above for comparison with the experimental results.

(2) Modeling the problem in full 3-D, and examining the differences with the 2-D axisymmetric analysis.

5.1 CTH Description and Problem Setup

The Eulerian shock physics code CTH [13, 15] was used to perform the benchmarking calculations. The CTH family of codes encompasses the mesh generation algorithms, analysis modules, and post-processing software, all for the analysis of transient, large deformation problems and/or problems involving strong shocks. CTH utilizes a two-step approach for solution of the conservation equations. This technique first involves a Lagrangian step, where the Eulerian mesh is allowed to deform. The Lagrangian step is followed by a remap step. The remap algorithm advects material quantities (*i.e.*, the volume flux, mass, momentum, and energy) from the deformed Lagrangian configuration back onto the fixed Eulerian grid. The tracking of material interfaces in CTH is done using a high-resolution interface tracker, more formally referred to as the Sandia Modified Young's Reconstruction Algorithm (SMYRA). The reader is directed to the basic CTH references [13, 15] for a more thorough discussion of the relevant methodology.

For these calculations, the multi-material temperature and pressure model option was employed, with material interfaces treated using the high-resolution interface tracker. Material response was modeled using the Sesame equation of state and the Steinberg-Guinan-Lund strength model. CTH library material model parameters were utilized for both the titanium and aluminum. Material fracture with subsequent void insertion is based upon a principal stress criteria. Fracture stresses used for the titanium and aluminum were –1.0 and –1.1 GPa, respectively. The selection of these values is largely experience-based with the values considered here derived from previous analyses [36-40].

5.2 Analysis of the 2-D Axisymmetric Problem

5.2.1 Mesh Resolution Study

The primary goal of this study was to examine the sensitivity of various quantities used for code benchmarking to zoning or mesh size. Quantities of interest include hole diameters in the target plate, debris cloud evolution, and velocity histories at the back surface of the witness plate. Thus, it is important to first understand their dependence on mesh resolution. Integrated with this study was an investigation of the important physics of the impact event. The simplified 2-D analysis provided insight into the problem and served as a foundation for more complex 3-D analyses discussed later.

For this study, the impact event was modeled in 2-D axisymmetry, with the axis aligned with the direction of the flyer motion. The titanium flyer plate was modeled as a flat circular disk, having a thickness and diameter of 0.8 and 17 mm, respectively. The CTH mesh was composed of an interior uniform-zone region surrounded by an outer region where the zone size was smoothly graded. Along the radial direction, the grid was uniformly zoned from the centerline out to a radius of 30 mm. The mesh was then graded out to a radius of 60 mm with a grading ratio of less than one percent. Semi-infinite boundary conditions were imposed along the outer radius of the mesh. The specified

width of the outer ring of CTH cells was twice that used in the central uniform-zone region. Mesh spacing along the axial direction was predominately uniform, with only a small graded region employed behind the flyer.

Three different mesh configurations were considered. These grids, referred to as the coarse, medium, and fine meshes, describe the cell width associated with the central uniform mesh region. Cell sizes associated with the coarse, medium, and fine meshes are 0.2, 0.1, and 0.05 mm, respectively. The total numbers of cells in the coarse, medium, and fine configurations are approximately 0.15, 0.60, and 2.3 million cells, respectively. To gain insight into the impact event, the results of the analysis for the medium mesh were examined first. Following this, comparisons were drawn with the coarse and fine meshes to assess the influence of mesh resolution.

Spatial plots of the material, density, and temperature fields at selected times are provided in Figures 5.01 and 5.02 for the flat flyer and medium mesh. In these plots, the density or temperature distributions are shown on the left-hand side, while the material regions are given on the right. For reference, incipient melt and vaporization temperatures for the titanium alloy are approximately 1943 and 3533 K [40], respectively. Incipient melt and vaporization temperatures for aluminum are approximately 933 and 2753 K, respectively [41].

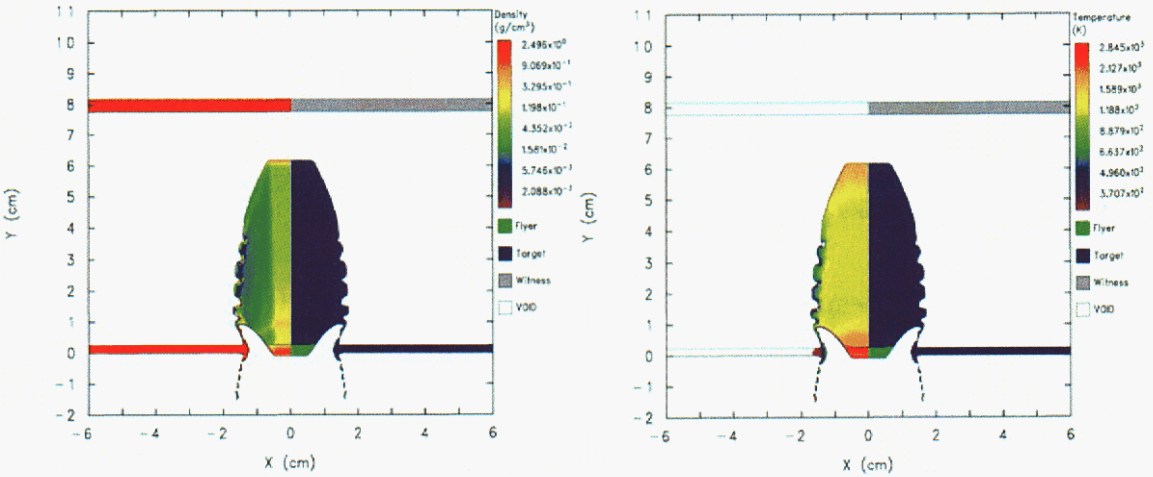

(a) Density **(b) Temperature**

***Figure 5.01**. Density (a) and temperature (b) for preliminary calculation with a medium mesh and a flat flyer at **t** = 8 μs. For these 2-D plots, the density and temperature are shown on the left and the materials are indicated on the right.*

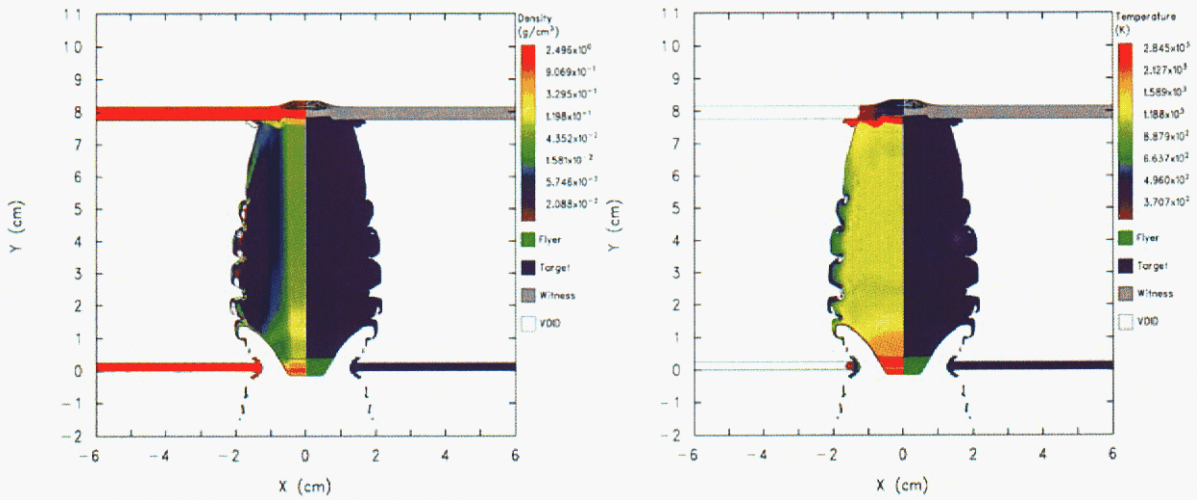

(a) Density **(b) Temperature**

Figure 5.02. *2-D plots for the preliminary calculation at* $t = 12\ \mu s$, *showing density (a) and temperature (b). Again, density and temperature are shown for the medium mesh.*

When the flyer impacts, it imparts virtually all of its momentum to the target. This momentum transfer is highly localized about the region of impact, leading to a plugging type of failure in the target. Almost immediately following impact, a debris cloud composed of aluminum target material is formed. The flyer remains in the vicinity of initial impact (at least for the time duration considered here), a consequence of the nearly complete momentum transfer to the target.

Over time, the debris cloud expands behind the target and eventually impacts the witness plate, as shown in Figures 5.01 and 5.02. The expanding debris cloud is characterized by a dense inner core of material surrounded by a radially expanding region of low-density material. The high-density inner core of material appears to stay relatively intact throughout the process of debris cloud expansion behind the target plate. High temperatures are noted at the leading edge of the debris cloud as well as in the region of initial impact. In general, temperatures are above the melt temperature, but below that needed for full vaporization.

At approximately 10 μs, the leading edge of the debris cloud impacts the witness plate. This impact results in a relatively short compressive shock wave being transmitted into the witness plate. When this shock pulse reaches the back surface, it is reflected as a tensile wave. The resulting tension cannot be sustained and material fractures or spalls from the back surface of the witness plate, as can be seen in Figure 5.02. One should note the exceedingly high temperatures in the vicinity of this impact, indicating vaporization of debris-cloud material in a localized region about the impact interface. In contrast, temperatures in the witness plate are significantly lower and do not appear to even exceed the melt temperature.

By 20 μs, the witness plate fails due to perforation by the dense inner core of material within the debris cloud. The diameter of the perforation hole in the witness plate is

slightly larger than that of the dense core of material observed earlier in the expanding debris cloud. Significant bending of the witness plate is noted in the neighborhood of this perforation hole.

Now that the salient features of the impact event have been discussed, we consider the influence of mesh resolution on the analysis. These effects are perhaps best illustrated by examining the debris cloud at a selected snapshot in time. For the fine and coarse meshes spatial plots of the density and temperature fields at 8 μs can be found in Figures 5.03 and 5.04, respectively. Comparisons with the medium mesh results shown in the earlier figures indicate that as the mesh is refined, the velocity of the leading edge of the debris cloud increases. CTH tracers embedded along the centerline of the target provide some indication of these leading edge velocities. Calculated leading edge velocities as a function of mesh resolution are provided in Table 5-1. Note that all of these velocities are higher than the original impact velocity. This phenomenon has been observed in other experiments involving low L/D flyer plates (*e.g.*, see [42, 43]). In a related aspect of this observation, which we had not anticipated, we found that for the coarse-zoned run the calculated signal arrival times at the rear of the witness plate were substantially later than either the fine-zoned runs (see Figures 5.05 and 5.06) or related experimental measurements. However, the peak particle velocity magnitudes were not too different. To examine these phenomena we looked at 1-D Lagrangian calculations, which will be described in a subsequent section. To anticipate those results, mesh resolution can have a significant influence on the so-called *jump-off* velocities for the debris cloud. Because this velocity equilibrates quickly, and is allowed to propagate over a relatively large distance—75 mm in this case—a significant error in the witness-plate arrival time can follow. This phenomenon is different from the normal effects of poor resolution, which generally show up in terms of smeared out and attenuated wave shapes.

Table 5-1. *Comparisons for 2-D axisymmetric problem.*

Mesh	Flyer Plate Configuration	Radius of Curvature (mm)	Leading Edge Velocity (km/s)	Hole Diameter (mm)
Fine	Flat	Infinite	7.76	25.0
Medium	Flat	Infinite	7.60	25.0
Coarse	Flat	Infinite	6.79	25.0
Medium	Warped	65.2	7.26	25.6
Medium	Warped	32.6	6.97	26.0

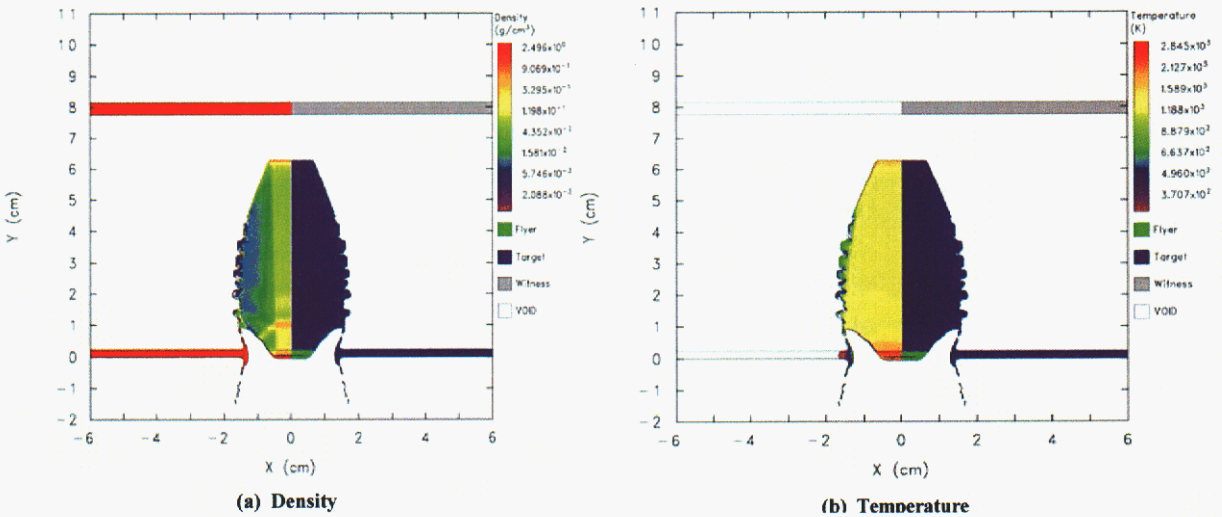

Figure 5.03. *Calculated density (a) and temperature (b) for a fine mesh and a flat flyer at* ***t*** *= 8 μs. The density and temperature are on the left and the materials are indicated on the right.*

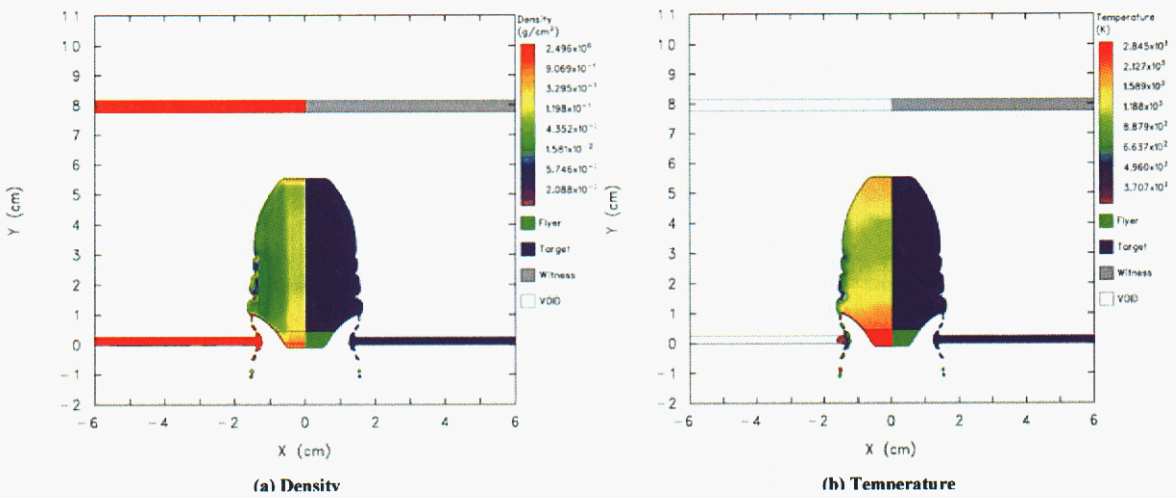

Figure 5.04. *Density (a) and temperature (b) with a coarse mesh and a flat flyer at* ***t*** *= 8 μs. As above, the density and temperature are shown on the left and the materials are indicated on the right.*

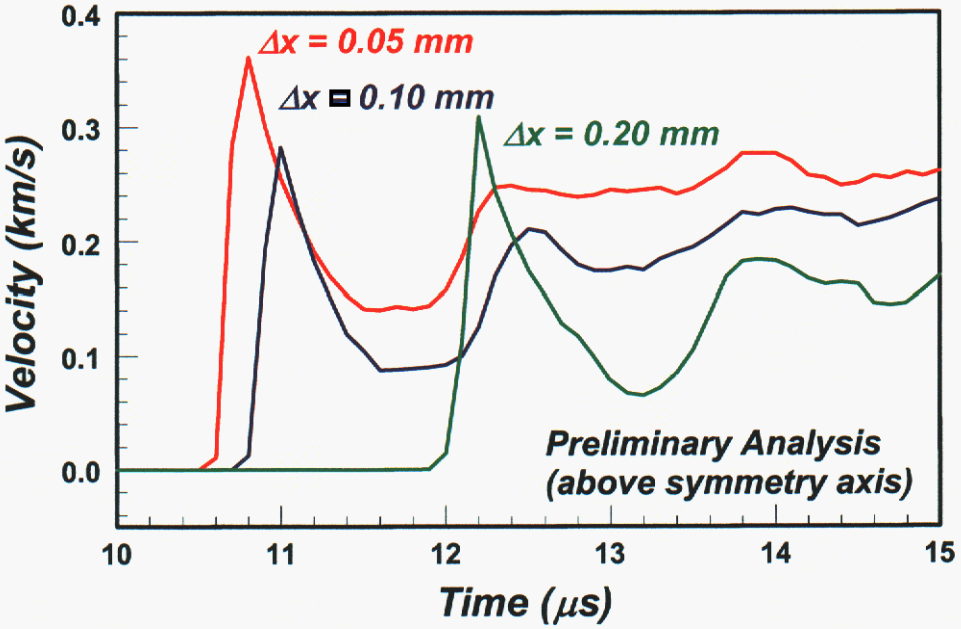

Figure 5.05. *Calculated velocities for above the axis of symmetry, at the rear of the witness plate, for the preliminary analysis. A flat flyer was used. As expected, a finer mesh leads to somewhat higher velocities and earlier arrival times. The latter is at least partly due to the errors in the jump-off velocity as the debris cloud is formed. The calculated traces are radially offset based on early experimental observations.*

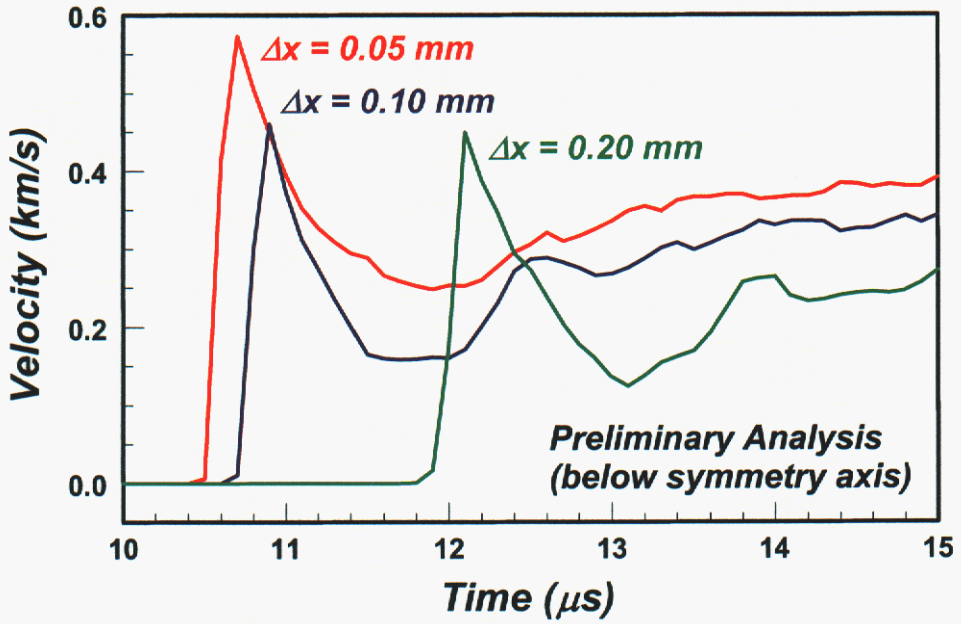

Figure 5.06. *Calculated velocities for below the axis of symmetry for the preliminary analysis, using a flat flyer. As with Figure 5.05, finer zoning gives higher velocities and earlier arrival times. These data suggest that* $\Delta x = 0.1$ *mm gives a reasonable, although not fully converged, compromise between accuracy and required computer resources. Note the expanded time scales here and in the previous figure. These profiles are radially offset in space based on early experimental observations.*

Notwithstanding the uncertainty in the jump-off velocities, the leading edge velocities increase with mesh resolution, and both the spatial and temporal errors appear to decrease, as expected. This leads to better resolution of the mass distribution and stress fields, which are used to calculate the cell face velocities by CTH. As the mesh is refined, we also note increases in the stress magnitudes, which lead to higher computed velocities throughout the mesh. In any case, the higher leading edge velocities produce a corresponding earlier arrival time of the debris cloud at the witness plate. The arrival time associated with the coarse mesh is significantly later that that for the medium and fine meshes, a consequence of the lower jump-off velocity as calculated by CTH. The peak magnitudes of the witness plate velocities were only marginally affected by resolution. Clearly, mesh resolution affects the analysis and it is important to understand the implications. For these 2-D analyses, it appears from these results, that although the solution is not fully converged, reasonable answers can be obtained with the medium mesh. The implications for 3-D analyses, and the fact that this conclusion may not fully apply to some of the other configurations or to higher impact velocities, are discussed later.

To benchmark the code against the experiments, comparisons will be drawn with the rear-surface velocities of the witness plate, as measured by velocity interferometers or VISARs. In contrast to hole sizes in the plates and the general characteristics of the debris clouds, these data are the most sensitive to the details of both the modeling and the experiments. Thus, it is of interest to examine the influence of mesh resolution on the calculated witness plate velocities. For this analysis, CTH tracers were specified on the *inside* of the back surface of the witness plate at a depth of approximately 0.2 mm, with a spacing of 1 mm along the radial direction. The velocities along the axial direction of the problem are extracted from the tracer data to illustrate this response. Radial locations for the tracers were picked to indicate representative variations and to match axial offsets observed in early experiments. Calculated free-surface velocity records are provided in Figures 5.05 and 5.06 for locations at different radii, above and below the axis of symmetry. Plots were not made for larger radii, as they were located too far away to exhibit any significant response over the time duration considered here.

An initial peak, followed by a decrease, and then another slow rise, characterize the calculated witness plate velocities in Figures 5.05 and 5.06. As described earlier, when this compressive pulse reflects off the back surface, a state of tension is induced in the material. The material cannot sustain this tension and the back portion of the layer begins to spall. The tracers shown in the figures are located in the spalled material. Hence, we observe a rise in their velocities as this material spalls and is accelerated from the witness plate. Both records are located in the vicinity of the outer radial extent of spalled material. There is a large gradient in the back surface axial velocities in this region. Thus, the history data is highly sensitive to its radial location. This is noted by the difference in the magnitude of the calculated peak velocities for the two relatively close locations that are shown. Away from the spall region, back surface velocities are small and more indicative of structural response.

Another important piece of data used for code validation is the target hole size. In particular, we are interested in comparisons of the hole sizes measured from radiographs. Consequently, we would like to assess the sensitivity of the calculated hole size to mesh resolution. Hole diameters calculated as a function of mesh resolution are also provided in Table 5-1. These data were determined from the material plots at 14 μs. Comparisons were also made at 12 μs; however, the differences were negligible. It is important to note the calculated hole diameter in Table 5-1 is defined as the inner diameter of the perforation hole in the target. This would not necessarily be the same measurement provided in experimental radiographs. However, the use of this definition provides a consistent means to evaluate the effect of mesh resolution. The numerical data indicate that the calculated hole diameter in the target is insensitive to mesh resolution.

The implications of the mesh resolution study for 3-D analyses are unclear. One cannot directly compare results as a function of mesh resolution between 2-D axisymmetric and 3-D problems. The reason is the radial weighting applied to the governing equations for 2-D axisymmetric problems. In practice, one cannot achieve comparable resolution for 3-D analyses. This is primarily due to limited computational resources and turn-around time for the analysis. However, the 2-D analysis can provide valuable insights into the issue, which aid in the development of the 3-D problem. One can expect that any comparisons of target hole dimensions will be insensitive to mesh resolution. One can also expect to observe later calculated arrival times as compared with experiment, since a coarser mesh will be needed for the 3-D analysis of the problem. However, the magnitude of the calculated witness plate velocities should be less influenced by mesh resolution.

5.2.2 *Influence of Flyer Geometry*

In the actual experiments, especially the *long throw* ones that involve substantial flight paths for the flyers, x-ray radiographs indicate that the flyers are warped when they impact the target. To assess the importance of this we will look at the influence of flyer geometry on the outcome of the impact event as a function of the flyer's radius of curvature. Early experimental observations suggested that this radius of curvature was as short as 32.6 mm. This will provide a starting point for this study, in which flyers having radii of curvature of 32.6 and 65.2 mm are modeled. The choice of the latter value is arbitrary and simply represents twice the experimental observation. Comparison with the results for the flat flyer plate will provide insight into the impact physics as the flyer curvature decreases (note that curvature is inversely proportional to the radius of curvature). Once again, the problem will be modeled in 2-D axisymmetry, with the same mesh used throughout. The choice of zoning is based upon the previous mesh resolution study, which indicated the medium mesh (*i.e.*, Δx = 0.1 mm) is adequate, albeit not fully converged, for modeling this problem in 2-D axisymmetry.

Spatial plots of the material, density, and temperature fields at selected times for the two warped flyers are provided in Figures 5.07 through 5.10. Review of the numerical data indicates a very different phenomenology associated with the warped flyer. The deformation process associated with the flyer differs significantly from that associated with the planar geometry. From the density plots, we see that the higher curvature flyer (R = 32.6 mm) folds over on itself, creating an elongated, dense projectile. This process of deformation changes drastically as the flyer geometry changes, with the *fold over* non-existent for the flat flyer. From the density plots, one also observes increasing radial dispersion of the debris cloud with decreasing radius of curvature. This observation holds for the central, inner core of target material. Qualitatively, the impact phenomenology becomes more representative of a spherical impactor as the radius of curvature decreases. Similar observations were noted by Konrad *et al.* [43] in a test series directly comparing the impact phenomenology of a low L/D flyer plate with that of a solid spherical impactor.

Calculated leading-edge velocities for the debris cloud are also provided in Table 5-1. As expected, the radial dispersion of the debris cloud results in lower leading edge velocities. The dispersion of the debris cloud front leads to a very different type of loading on the witness plate. As the radius of curvature decreases, the magnitude of the loading on the witness plate decreases, with a corresponding increase in the duration of the loading. Hence, the loading is less impulsive in nature, with structural bending becoming more predominant. For the warped flyers, perforation of the witness plate does not occur over the time duration considered in the analysis (approximately 20 to 25 μs). However, the calculations do indicate significant material velocities in the witness plate. One can expect that further bending of the plates would have been predicted, with rupture occurring later in time.

Synthetic radiographs were generated at 14 μs for comparison with related experimental results, as shown in Figure 5.11. The algorithm for generating the synthetic radiographs projects the total mass along a shotline onto a prescribed viewing plane. The resulting plot displays an aerial density of the material. When viewing the synthetic radiographs, one notes several dark vertical bands. These bands are an artifact of modeling the problem in 2-D axisymmetry. In a real 3-D problem, material will fracture, leading to a debris cloud composed of irregular fragments and molten material. When modeling the problem in 2-D axisymmetry, the rings of material stay essentially intact. Consequently, the out-of-plane phenomena are not modeled well. One should bear this in mind when interpreting results for the 2-D axisymmetric problem.

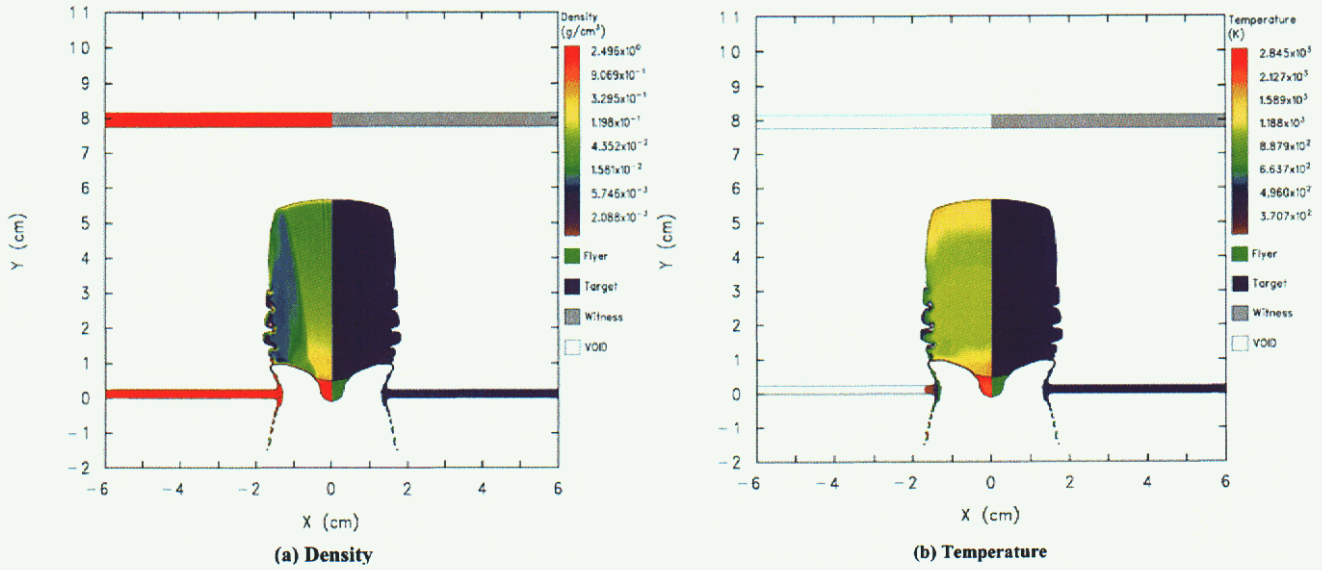

(a) Density (b) Temperature

Figure 5.07. *Preliminary calculations of the density (a) and temperature (b) for the warped flyer (R = 32.6 mm) at* $t = 8\ \mu s$. *The variables are shown on the left and the materials are indicated on the right.*

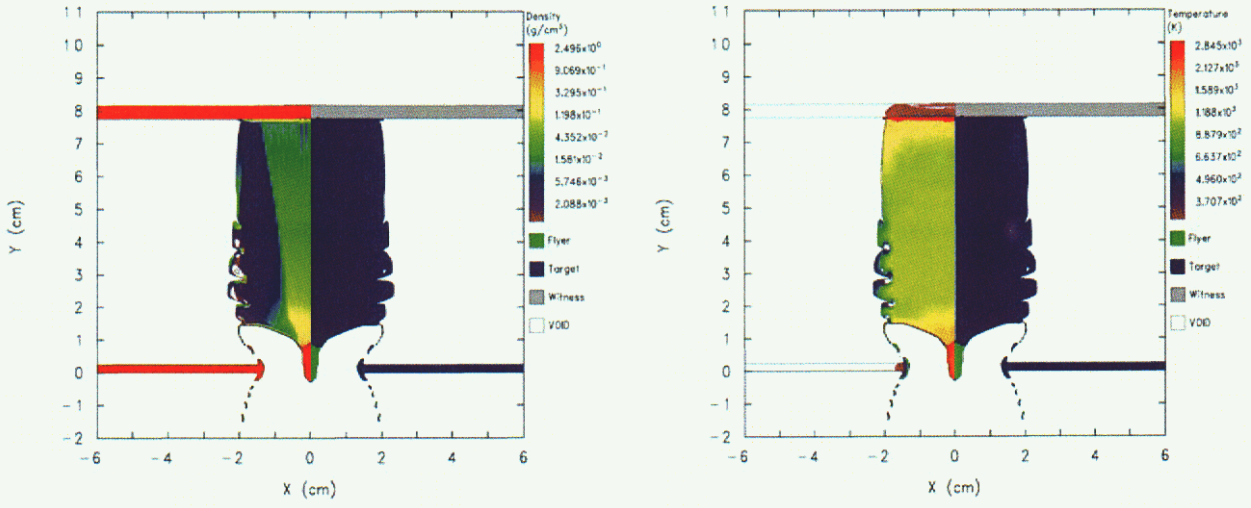

(a) Density (b) Temperature

Figure 5.08. *Density (a) and temperature (b) for the warped-flyer (R = 32.6 mm) preliminary calculation at a later time,* $t = 12\ \mu s$.

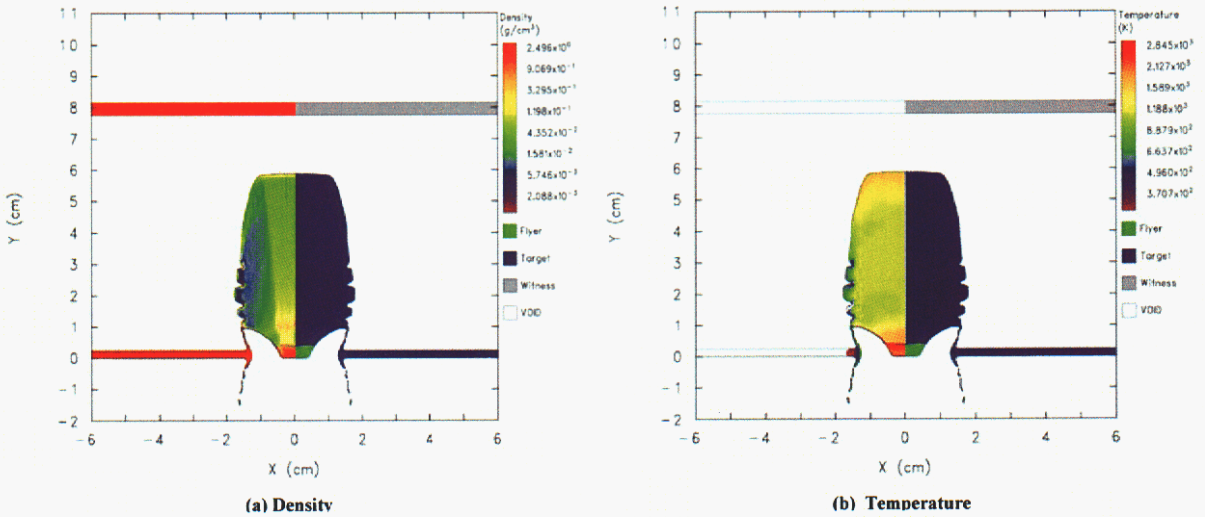

Figure 5.09. *Density (a) and temperature (b) for a larger radius-of-curvature flyer (R = 65.2 mm) calculation, at* $t = 8\ \mu s$.

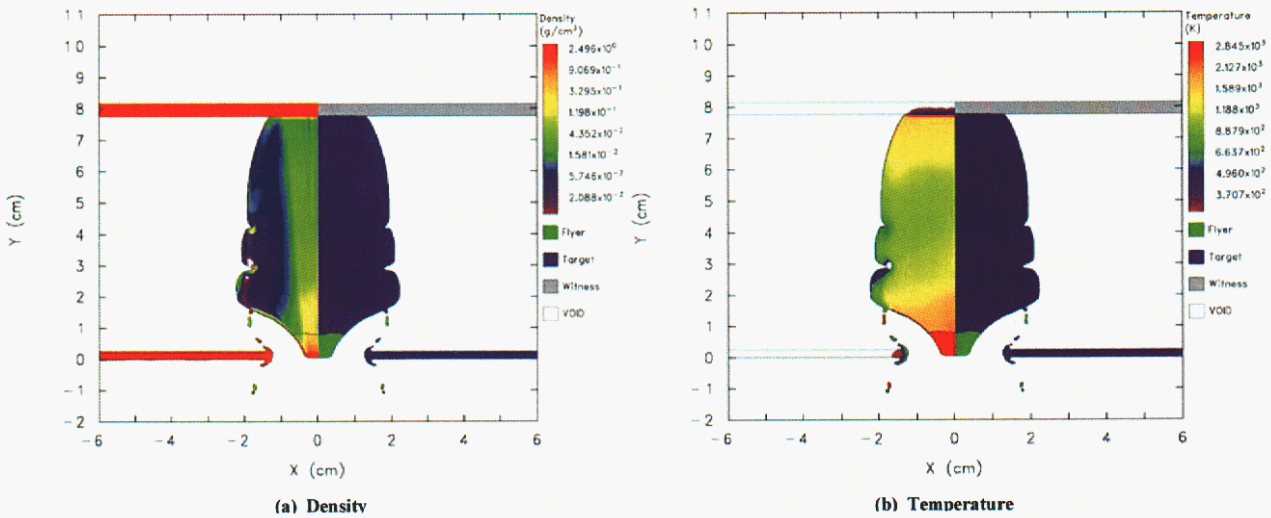

Figure 5.10. *Density (a) and temperature (b) for the warped-flyer (R = 65.2 mm) calculation, at a later time of* $t = 12\ \mu s$.

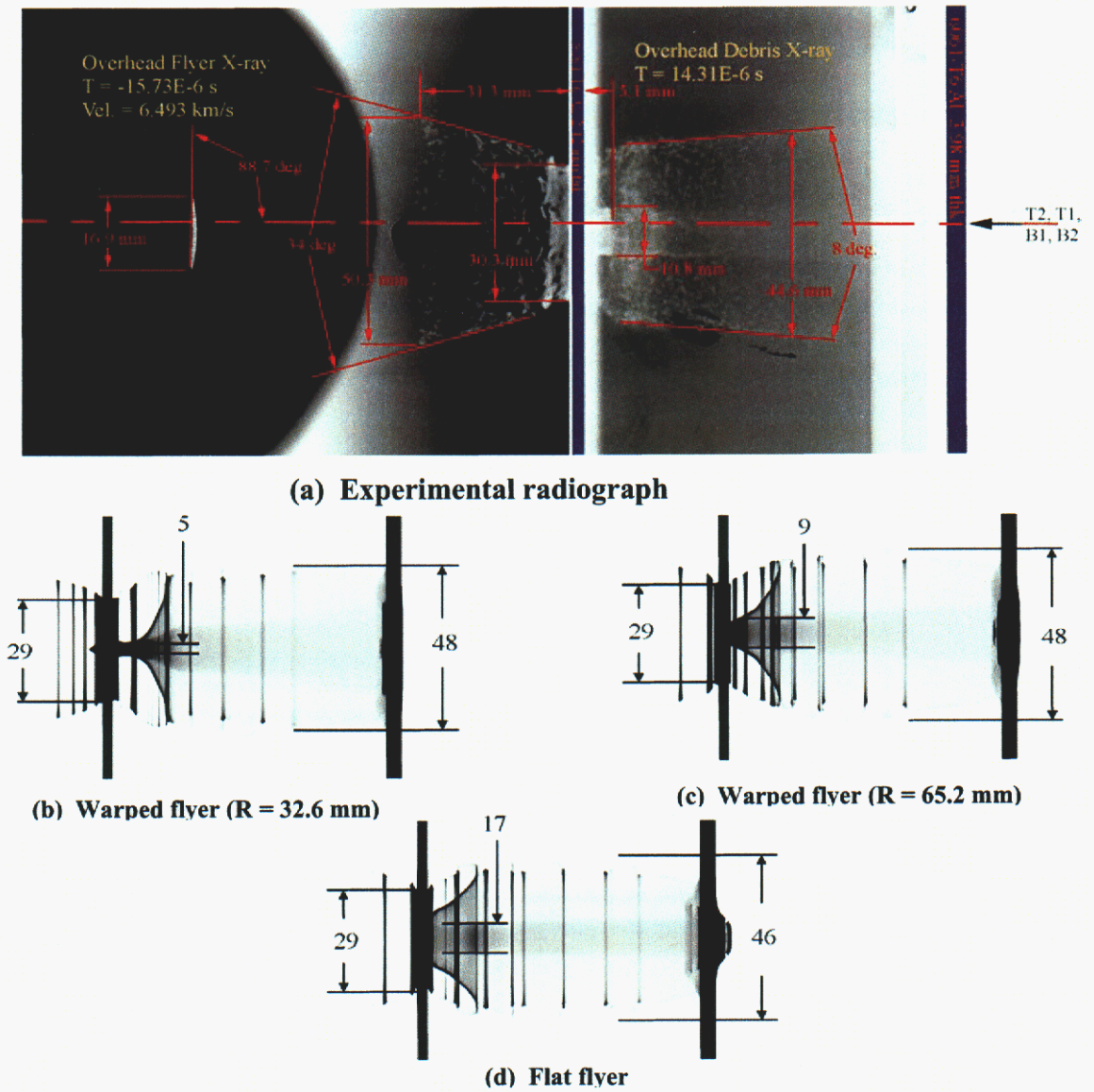

Figure 5.11. *2-D radiographs for the preliminary analysis. An experimental radiograph for a closely related experiment (CLP-2) is shown in (a). A synthetic radiograph for the 2-D calculation with small radius of curvature (R = 32.6 mm) is given in (b), that for a large radius of curvature (R = 65.2 mm) in (c), and for a flat flyer in (d). The comparisons are at 14 μs, and all dimensions are in millimeters.*

Interpretation of measurements made from the synthetic radiographs is subjective. This is due to the lack of clarity in the spatial plots as well as an inability to exactly reproduce the experimental setup (*e.g.*, viewing planes, exposure settings, and so forth). However, there are several features sufficiently defined and suitable for quantitative comparisons. These data are the diameter of the dense inner core of the debris cloud, taken at an axial position 5.1 mm from the back surface of the target (measured as 10.8 mm); the outer diameter of the debris cloud (measured as 44.6 mm); and the diameter of ejecta from the target (measured as 30.3 mm). The calculated diameter of the inner core diameter varies

significantly with flyer geometry, with the flyer having a radius of curvature of 65.2 mm appearing to have the best correlation with the experimental measurements. The remaining comparisons appear relatively insensitive to flyer geometry and reasonably match the related experimental results. When viewing the synthetic radiographs, it appears the warped flyer having a radius of curvature of 65.2 mm provides better overall correlation with the experimental observation. The *fold over* noted for the larger curvature flyer (R = 32.6 mm) is clearly not indicated in the experiment. Also, the dense inner core in the experiment is somewhat conical, but not as widely dispersed as shown in Figure 5.11 (b). Synthetic radiographs were also generated at 12 μs. Comparisons with the experimental results yielded similar observations and conclusions.

Calculated velocity histories for different locations above and below the symmetry axis are provided in Figures 5.12 and 5.13, respectively. The effects of flyer geometry are readily apparent in the records, where the magnitude of the witness plate velocity increases with the radius of curvature. This correlates with the character of the debris cloud associated with the different flyer geometries. As the radius of curvature increases, the inner core of material in the debris cloud becomes more focused, resulting in a more localized loading on the witness plate. In turn, this leads to larger back surface velocities near the axis.

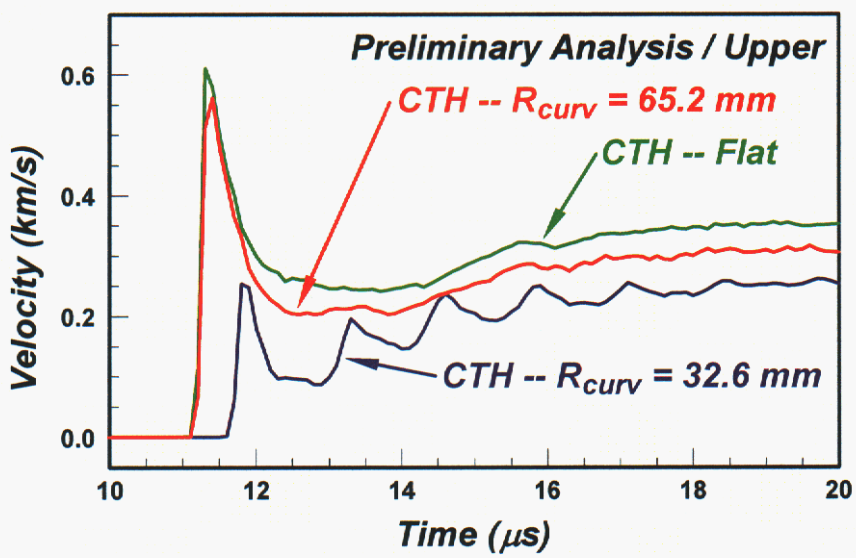

Figure 5.12. *2-D velocity histories for the preliminary calculations and the upper tracer location, as a function of flyer geometry. For these velocity records, the larger radius of curvature (R = 65.2 mm) gives results that are nearly the same as those for the flat flyer.*

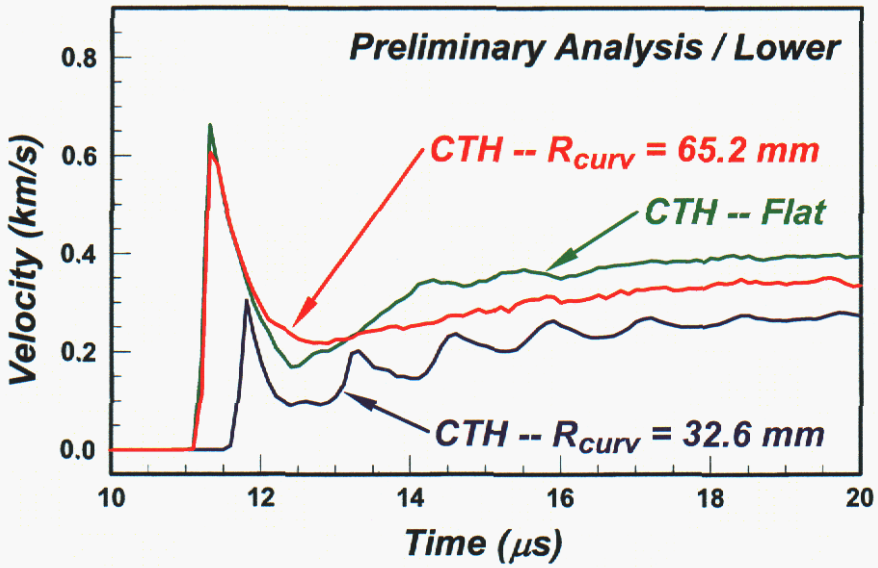

Figure 5.13. *2-D profiles for calculated velocity records for the preliminary analysis and the lower tracer position. Again, the record for the larger radius of curvature (R = 65.2 mm) is very similar to that for the flat-plate flyer.*

However, since we do know from radiographs for a long-throw experiment that the flyer really was warped, these comparisons suggest that the larger radius of curvature may provide a better qualitative match to the observations. With regard to the flyer geometry, there are qualitative differences between related experimental radiographs and calculations using small radius-of-curvature flyers. Uncertainty in measuring this curvature could provide a possible explanation. Potential sources of error include lack of sharpness in the radiographs, lack of orthogonality with the viewing plane, non-constant curvature, and/or changing curvature with flyer propagation distance. At the present time, this measurement error cannot be quantified. However, based upon the preceding analysis, it is probably safe to assume the two warped flyers considered here bracket the typical flyer geometries for long-throw experiments.

5.3 Analysis of the 3-D Problem

We will now discuss the preliminary modeling of this basic configuration in 3-D, mainly to examine differences with the 2-D axisymmetric analysis. As mentioned previously, there are some inconsistencies in the results when evaluating the two warped flyers. The 2-D analysis suggests the flyer having the larger radius of curvature (R = 65.2 mm) is more representative of long-throw experimental conditions. Thus, for the 3-D analysis, we felt it was necessary to explicitly model both flyer geometries to further assess possible differences with the experiments. No attempt was made to model the flat flyer in 3-D.

Quarter symmetry was assumed when modeling the 3-D problem. In the CTH problem setup, the x- and y-axes of the mesh were aligned with the symmetry planes, while the z-axis was aligned with the velocity vector of the flyer. Semi-infinite boundary conditions were prescribed at the outer extents of the mesh along the x- and y-axes. The

CTH mesh was composed of an interior uniform mesh region surrounded by an outer region where the mesh is smoothly graded. Along the x- and y-axes, the grid was uniformly zoned from the centerline out to a radius of 30 mm. The mesh was then graded out to a radius of 50 mm with a grading ratio of approximately two percent. The mesh spacing along the z-axis was predominately uniform, with only a small graded region employed behind the flyer. The cell size in the uniform region was 0.2 mm. There were approximately 12.5 million cells in the mesh. This problem was run on the SNL Intel Teraflops machine using 196 processors. The resolution of this problem is comparable to the coarse mesh used in the 2-D mesh resolution study. Better resolution was desired, but was not possible in practice as memory requirements and analysis turn-around times would have become unmanageable.

Material plots illustrating the three-dimensional evolution of the debris cloud for the two warped flyers are provided in Figures 5.14 and 5.15. Examination of the 3-D results provides observations and conclusions that are similar to those made for the 2-D axisymmetric problem concerning the impact phenomenology. The most obvious differences between the 2-D and 3-D calculations reside with the evolution of the debris cloud. This is most clearly illustrated by comparing results at 12 μs, as shown in Figures 5.16 and 5.17. When comparing the 2-D and 3-D results, one notes lower leading-edge velocities and greater radial dispersion of the debris cloud for the 3-D simulations. These differences are attributed to mesh dependencies. To confirm this, the corresponding 2-D axisymmetric problems were run (*i.e.*, the 2-D problem employed a mesh having a cell size of 0.2 mm). Spatial plots of the density, temperature, and material fields were virtually identical to those of the 3-D analysis. Similar comparisons were made for the leading edge velocities of the debris cloud and the measured hole diameters in the target. These are listed in Table 5-2. Once again, comparable results are noted for the 2-D and 3-D problems when considering *equivalent* meshes.

Table 5-2. *Comparison of 2-D and 3-D analysis results for warped flyers.*

Problem Type	Mesh	Radius of Curvature (mm)	Leading Edge Velocity (km/s)	Hole Diameter (mm)
2-D Axisym	Medium	65.2	7.26	25.0
2-D Axisym	Coarse	65.2	6.52	25.6
3-D	Coarse	65.2	6.47	25.6
2-D Axisym	Medium	32.6	6.97	26.0
2-D Axisym	Coarse	32.6	6.20	26.0
3-D	Coarse	32.6	6.20	26.0

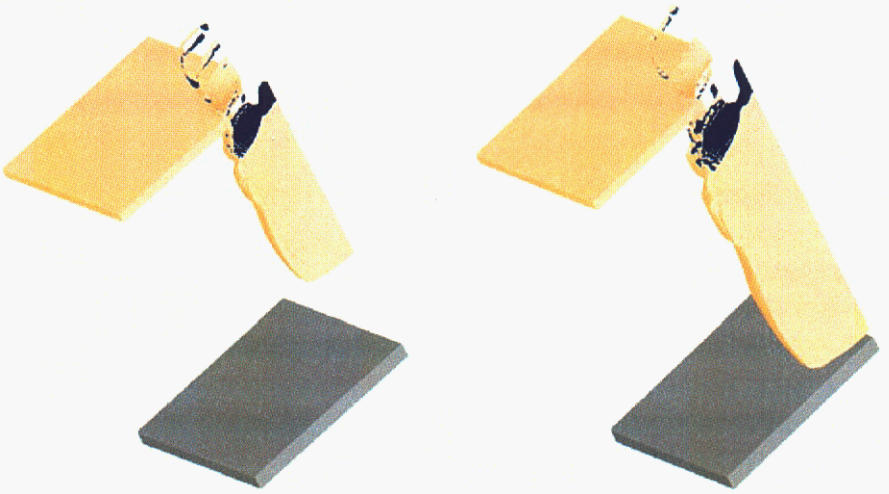

(a) t = 8 μs (b) t = 12 μs

Figure 5.14. *3-D calculation for the preliminary analysis at (a) t = 8 μs, and (b) 12 μs, for the smaller radius-of-curvature (R = 32.6 mm) warped flyer.*

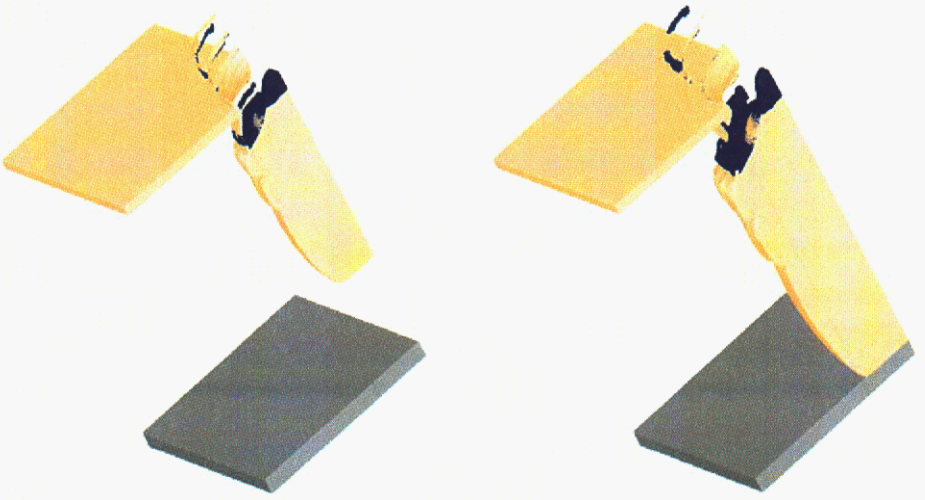

(a) t = 8 μs (b) t = 12 μs

Figure 5.15. *3-D calculation for the preliminary analysis at (a) t = 8 μs, and (b) 12 μs for the larger radius-of-curvature (R = 65.2 mm) warped flyer.*

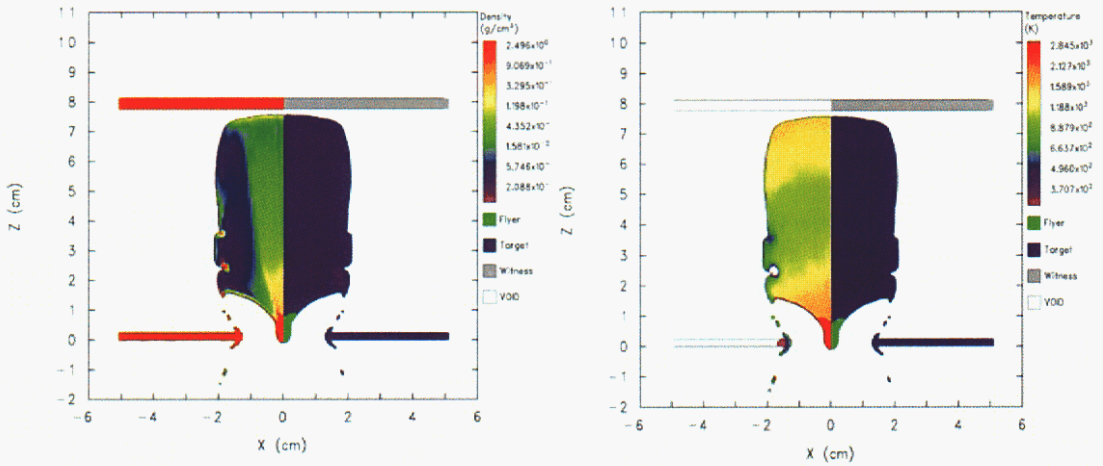

(a) Density (b) Temperature

Figure 5.16. *Density (a) and temperature (b) for the 3-D preliminary calculation using a coarse mesh and a warped flyer (R = 32.6 mm) at* $t = 12\ \mu s$. *For these plots, the density and temperature are shown on the left and the materials are indicated on the right. The corresponding 2-D results are given in Figure 5.8.*

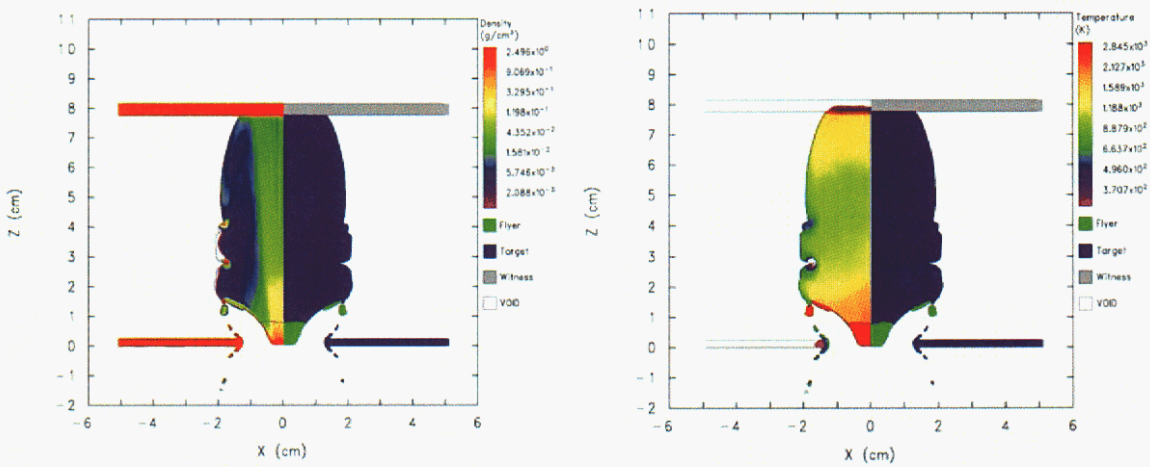

(a) Density (b) Temperature

Figure 5.17. *Density (a) and temperature (b) for the preliminary 3-D calculation with a coarse mesh and a warped flyer (R = 65.2 mm) at* $t = 12\ \mu s$. *Again, the variables are given on the left and the materials are indicated on the right. The corresponding 2-D comparison is given in Figure 5.10.*

These results are surprising. For the 2-D axisymmetric problem, there is a radial weighting applied to the governing equations. One would expect a greater difference when comparing results of 2-D and 3-D problems with equivalent meshes. It is possible that for this class of problem, we are observing a close correlation between the results for the 2-D axisymmetric and 3-D problems as a function of mesh resolution. This is fortuitous as the results of the 2-D mesh resolution study can now aid with interpretation of results for the 3-D problem.

Synthetic radiographs were generated at 14 μs for comparison with the related experimental radiograph shown earlier (Figure 5.11); they are presented here in Figure 5.18. The general character of the radiographs is similar to those generated for the 2-D analysis. The major difference is with the bands of dense material in the debris cloud. Clearly, the out-of-plane phenomena are better accounted for in the 3-D analysis, but it still falls short of replicating the fragmentation behavior observed in the experiments. In particular, significant differences are noted for the fragment size and distribution. These observations indicate a potential problem with the fracture criteria, the fracture model itself, or mesh effects.

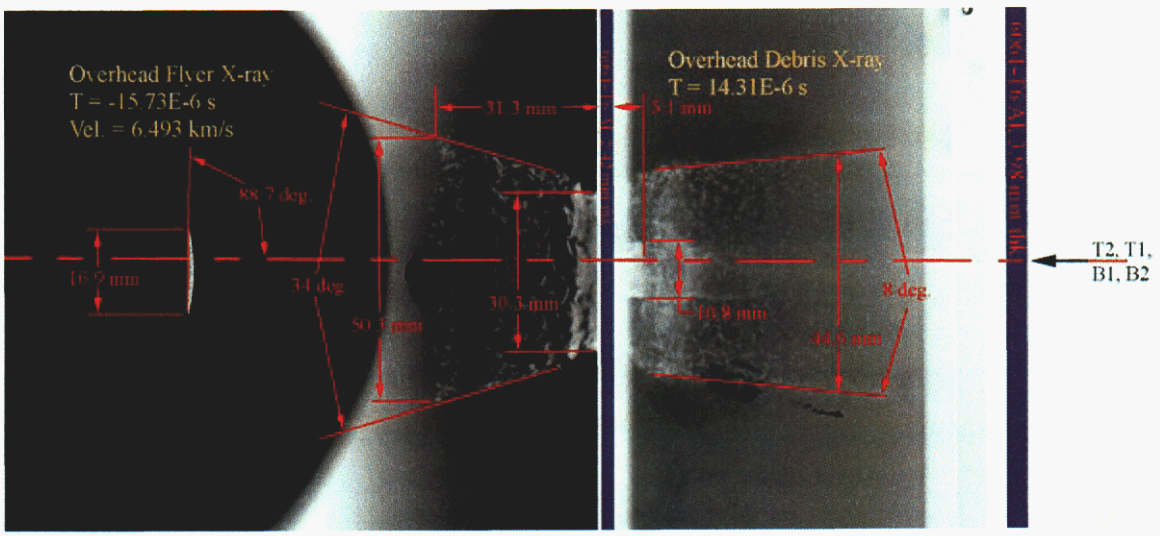

(a) Experimental radiograph

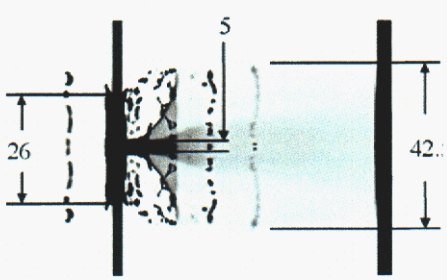

(b) Warped flyer (R = 32.6 mm)

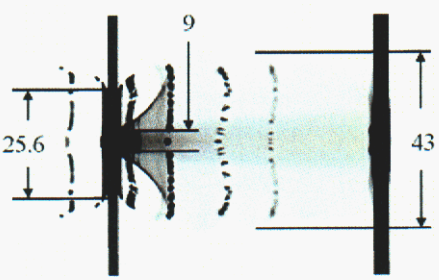

(c) Warped flyer (R = 65.2 mm)

Figure 5.18. *3-D radiographs for the preliminary analysis, for the related experiment (a), for the 3-D calculations with small radius of curvature (R = 32.6 mm) (b), and for the large radius of curvature (R = 65.2 mm) (c). The comparisons are at 14 μs, and all dimensions are in millimeters.*

As with the 2-D analysis, the results for the higher radius of curvature flyer (R = 65.2 mm) appear more representative of the experimental results. As discussed previously, the error associated with measurement of the flyer curvature cannot be quantified. However, it is felt that the warped flyer geometries considered provide some bounding estimate of results by bracketing the true flyer geometry.

With regard to the velocity histories from the rear of the witness plate, the 3-D calculations give results that essentially mirror those from the comparably zoned 2-D computations. That is, the peak amplitudes are substantially higher for the large radius-of-curvature calculations, and are nearly the same as would be predicted with a flat-plate configuration. However, we note that the arrival times are over-predicted; this is likely due to the coarse resolution and the attendant errors in the jump-off velocity of the debris cloud from the target plate, as was suggested previously.

We conclude this extensive analysis by noting that the numerically simulated radiographs agree reasonably well in a qualitative fashion with the experimental results. However, signal arrival times at the rear of the witness plates often show a large variation that is strongly correlated with zone size. This latter discrepancy is probably due to numerical errors associated with the jump-off velocity at the rear of the target plate. In addition, the geometry and configuration of the flyer can have a major influence on its interaction with the target plate, the formation and evolution of the debris cloud, and even the detailed response of the down-stream witness plate. It is for these reasons that most of our later experiments, at both high and low velocities, were performed with much shorter flight paths for the flyer plates, and much smaller stand-off distances for the witness plates. There are a number of possibilities for these uncertainties, and they include the lack of non-equilibrium equations of state, inadequate material failure models, or even poorly understood numerical resolution and convergence issues that may be related to the experimental conditions.

6. One-Dimensional Calculations

The discrepancies revealed by the detailed preliminary CTH calculations suggested that there were some specific phenomena, both numerical and physics-based, that needed additional study. We felt that some relatively simple one-dimensional analyses would help to clarify several of these issues.

6.1 Resolution and Debris Jump-off Velocities

We initially observed that mesh-resolution issues influenced the numerical results in ways that we had not anticipated. Specifically, we found that target hole sizes were insensitive to zoning, and also that the debris-cloud dimensions displayed a relatively small dependence on the mesh parameters. In contrast, the computed back-surface velocities of the witness plates appeared to be effected significantly by the zone size. In particular, for many of these simulations the calculated arrival times showed a much larger dependence on zone size than we had expected. However, the velocity magnitudes were not too far from their numerically converged values, at least for the preliminary configuration. To examine these phenomena we looked at 1-D Lagrangian [44] calculations of the flyer-target interaction using the parameters employed in the preliminary CTH calculations, without considering flyer warp or tilt. For these 1-D calculations standard Mie-Grüneisen equilibrium equations of state were used for both the titanium flyer and the aluminum target.

Numerical results from these calculations are plotted in Figures 6.01 and 6.02. The first of these plots shows the velocity histories for the target rear surface for various levels of resolution, ranging from one (Δx = 0.8 mm) to 100 zones (Δx = 0.008 mm) across the thickness of the flyer. This velocity is the one-dimensional analog to the velocity of the leading edge of the debris cloud. Because it equilibrates so rapidly, we call it the *jump-off* velocity. The two finer zone sizes (50 and 100 zones in the flyer) exhibit numerical results that essentially overlap, and are thus fully converged. However, by dropping down to 10 or fewer zones across the flyer, the jump-off velocities fall off by as much as 20 percent or more. Because the debris is allowed to propagate over relatively large distances—50 to 75 mm for many of the experiments considered here—a comparable delay in the arrival times for the witness-plate velocity measurements is often observed in the simulations. Similar results have been obtained by other investigators using other hydrocodes [45, 46]. This phenomenon is different from the standard effects of less-than-adequate resolution, which generally show up in terms of smeared out and attenuated wave profiles. We presume it is related to classic CFD problems connected with pressure-driven free expansions into voids [47]. We should note that because the wave *amplitudes* often show a much smaller effect—only the arrival times are substantially delayed—the total momenta or impulses are also influenced less. In the 2- and 3-D CTH calculations these differences are smeared out to some extent, but they still lead to discrepancies in the witness-plate arrival times of ten percent or more. Note that these jump-off velocity errors occur even for numerical resolutions that are very nearly converged with regard to wave amplitudes. We will take advantage of this observation by appropriately shifting several of the VISAR comparisons considered later.

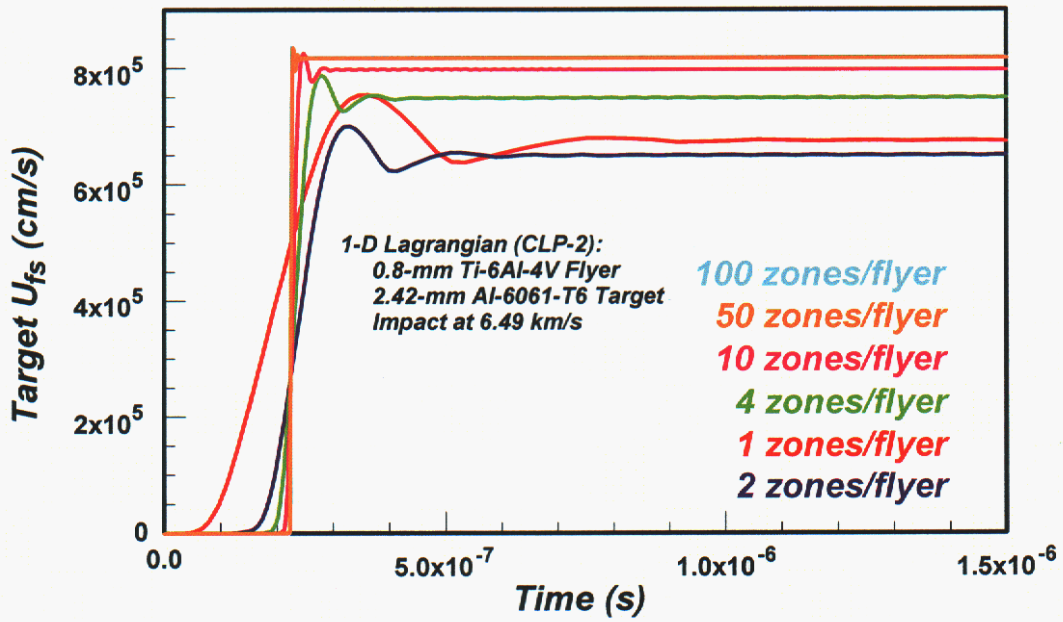

Figure 6.01. *1-D jump-off velocity histories for the rear surface of the target for shot CLP-2, which was similar to the preliminary configuration. The numerical resolution ranges from one (Δx = 0.8 mm) to 100 zones (Δx = 0.008 mm) through the flyer thickness, and the calculations show a range in equilibrated velocity of ~20%.*

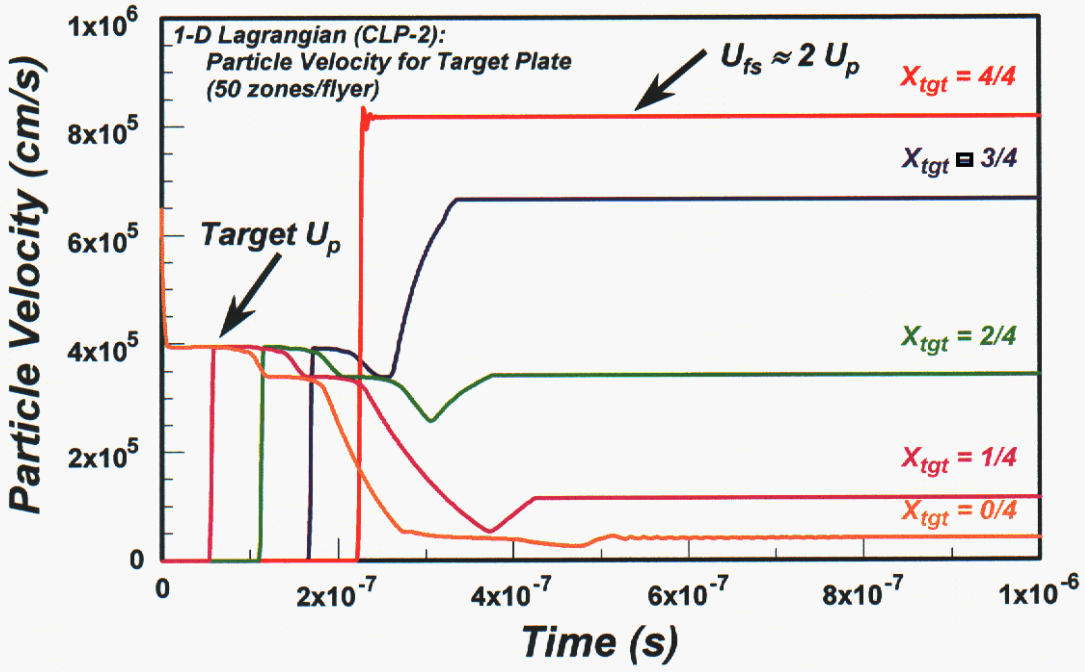

Figure 6.02. *1-D velocity histories through the target thickness for CLP-2, which again was similar to the preliminary configuration. The indicated distances are Lagrangian positions relative to the initial target thickness.*

To show that these 1-D calculations are representative of the initial stages of the formation of the debris cloud, we plot the particle-velocity histories at various points

through the thickness of the target, as shown in Figure 6.02. The calculation used one of the finer-zoned (50 zones in the flyer) configurations, and is thus fully converged. The traces shown are for evenly spaced Lagrangian points through the target, for example, at the front surface (labeled $X_{tgt} = 0/4$), halfway through the target ($X_{tgt} = 2/4$), and at the target rear surface ($X_{tgt} = 4/4$). The particle velocity labeled *Target* U_p matches the value predicted by the Hugoniot jump conditions for the impact, as it should. Also, the free-surface velocity, labeled U_{fs}, is very nearly twice the U_p value, again, as it should be. Thus these 1-D calculations do represent the physics associated with at least the initial stages of the debris generation process. Finally, we note that these calculations are Lagrangian, whereas the multi-dimensional code primarily used for this study, CTH, is Eulerian. This could lead to some numerical differences, however, because the leading-edge debris velocities equilibrate very rapidly, we feel that these observations are reasonable and applicable to both types of codes.

6.2 Influence of EOS on Witness-plate Response

Other observations indicate that the evolution of the debris cloud may depend in a complex way on the *non-equilibrium* equation of state of the target material, which forms the bulk of that debris. To look at this issue with the simple Lagrangian code we chose to examine shots CLP-5 and CLP-15. They were both impacts at ~11 km/s, which should be over the threshold for the vaporization phenomena described earlier. The calculations employed target thicknesses of ~2.5 and ~1 mm, respectively. We used the experimental stand-off distance, 51 mm, and extracted the particle velocity at the interface between the aluminum and the lithium-fluoride window at the rear of the witness plate.

To provide an indication of the importance of the equation of state under these impact conditions, we used the nominal parameters for aluminum, and then, for the target plate only, varied the vaporization energy, E_s, over a reasonable range. The Al/LiF interface velocity histories in the witness plate are plotted in Figure 6.03. For this one-dimensional geometry and the nominal value of E_s, 14 kJ/g, the peak velocities are between 5 and 6 km/s, as shown in the upper two plots. Reducing the vaporization energy to a value near the melt energy of aluminum, 2.2 kJ/g, gives the results shown on the bottom. The lower value of E_s allows substantially more material to vaporize, and the debris cloud disperses in a much more uniform fashion, even in the one-dimensional calculations described here. Thus the loading on the witness plate is less in amplitude but broader in time. In fact, the peak velocities at the Al/LiF interface are about one-fourth as large. We could also have raised the value of E_s, to produce a reduction in the amount of material vaporized from that in the nominal calculation. However, that would have complicated the numerical analysis by producing considerable failure and fracture in the debris formation process in the target material, and would have obscured the general phenomena we were trying to observe.

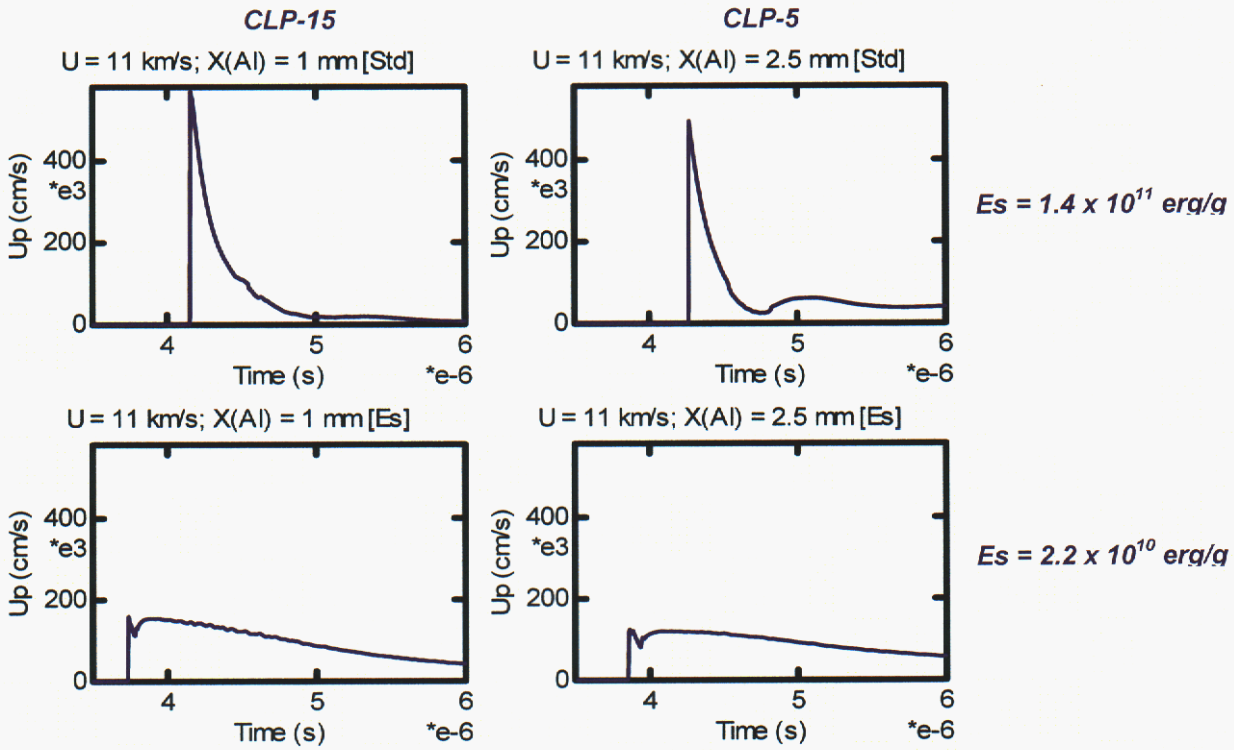

Figure 6.03. *Velocity history at the Al/LiF interface in the witness plate. The left-hand column is for CLP-15 parameters, and the right-hand column is for CLP-5. The upper plots are for the nominal vaporization energy,* E_s *= 14 kJ/g, and the lower plots are for the reduced value,* E_s *= 2.2 kJ/g.*

To see some of the details of the debris cloud evolution, we have plotted both the material velocity and density in Figure 6.04. In this instance we have plotted only the results for shot CLP-5, because the general phenomena are the same for both CLP-5 and CLP-15. The numerical resolution is indicated by the symbols on the individual curves. A five-zone buffer of low-density air between the debris and the witness plate, which was included to allow the smooth progression of the Lagrangian calculation, was not included in the plots. The time was late in the interaction, just before the debris impacts the witness plate. For the nominal value of E_s, the debris cloud retains a higher density (~80 percent that of solid aluminum), plate-like leading edge that gives rise to the greater level of loading on the witness plate. When E_s is dropped to the artificially low value near the melt energy, much more material is vaporized, the debris cloud moves somewhat faster, but there is no plate-like leading edge. In fact, the higher debris velocity for the latter case is the reason for the earlier time of the plot—again, just before the debris impact on the witness plate—for the low-E_s calculation. Even though the velocity is higher, it cannot make up for the much lower debris density, and consequently, the loading on the witness plate is much lower in amplitude, but appears to last for a longer period of time. In both cases shown in the figure, we have used the same parameter scales so that the comparisons can be made more readily.

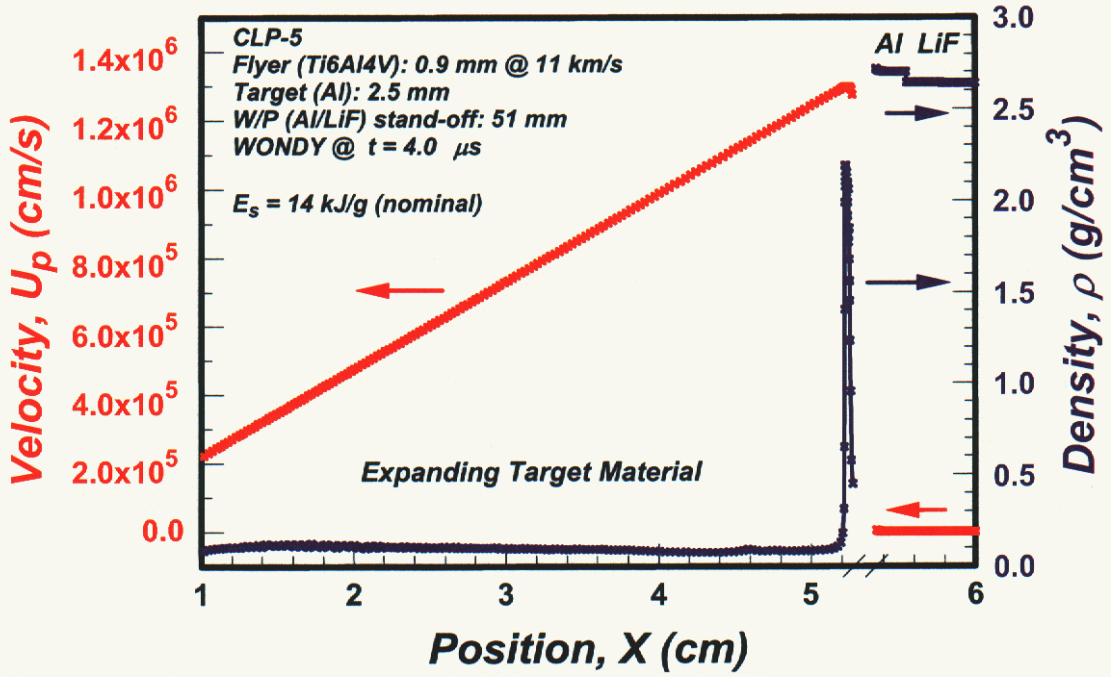

(a) Nominal E_s

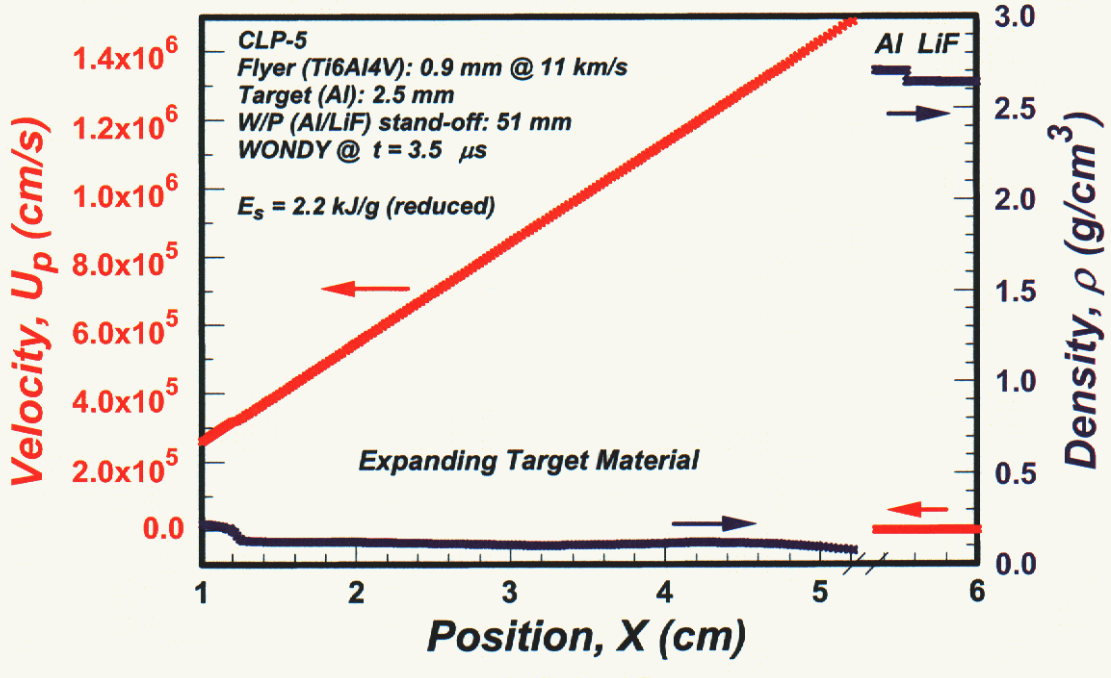

(b) Reduced E_s

Figure 6.04. *1-D material velocity and density plots for CLP-5, just before the debris impacts the witness plate. The upper plot (a) is for the nominal value of the vaporization energy for the target, and the lower plot (b) is for a reduced value, roughly equal to the melt energy of aluminum. Note that for the former case the debris cloud contains a high-density plate-like leading edge, while the second case, because of the larger amount of vaporized material, has no such feature. However, the debris velocities for the latter are uniformly about 15% higher.*

The general conclusion is that reasonable changes in the way the equation of state treats vaporization can have a major influence on the generation and evolution of impact-induced debris clouds. This is true, in particular, for conditions near the threshold for vaporization. These simple calculations are only rough approximations to the real debris-cloud behavior, which must be analyzed with more detailed multi-dimensional hydrocodes, but they do provide some qualitative idea of the importance and potential need for non-equilibrium equations of state for these types of problems. These future, more elaborate models would then represent vaporization as time-dependent functions of pressure, temperature, and density.

7. CTH Calculations and Comparisons with Experiments

7.1 Quasi 1-D Experiments and Calculations

Multi-dimensional CTH calculations were performed for many of the other experimental shots as well. As with the preliminary analyses, the equations of state that we are using are the standard ones used with CTH for aluminum and titanium alloy. The aluminum, which is used for both the target and the witness plates, is modeled with Sesame No. 3700 [12]. It includes both equilibrium melting and vaporization, and incorporates a tensile region for temperatures below 1500 K. The Ti-6Al-4V alloy flyer is represented by Sesame No. 4060, and does not include the melting transition [38]. Both of these materials use strength models as given by Steinberg [37].

As mentioned earlier, there are many different aspects of the experimental configuration that must be taken into consideration when simulating the measured results, and in fact, the computational details vary for each experiment. The overall configuration is certainly two-dimensional, and in a few cases even three-dimensional. For example, if the impact of the flyer on the target is non-normal, or if the flyer appears to be curved rather than planar, the response should be modeled with multi-dimensional calculations. On the other hand, if the flight distances of the flyer before impact and the stand-off distances between the target and the witness plate are both relatively small, then at least along the center-line, the sample response appears to be nearly one-dimensional. In this latter case the code calculations can bring out physics issues without the complications associated with geometric divergence and dispersion. Although we have performed many calculations as part of this program, here we will concentrate on just a few that meet these nearly-one-dimensional criteria so that some of these physics issues can be addressed. The best candidate experiments are CLP-6 and CLP-22. As shown earlier, the flyers are essentially flat, and impact the target in a normal fashion. The stand-off distances for the witness plates are 23 and 10 mm. This is in contrast to many of the other shots, where the stand-off is 50 to 75 mm. Thus the measured velocity histories at the back of the witness plates, as seen through LiF windows, should be very nearly one-dimensional. The impact velocities are ~9 and ~11 km/s, respectively, and at the higher level should thus be at or above the *vaporization* threshold described earlier. One-dimensional CTH calculations were performed for both of these experiments.

To ensure that the calculations have adequate numerical resolution, individual zone sizes of 0.01 mm were employed. Although they will not be shown here, numerous runs for which this zone size was varied by a factor of 20, from 0.2 to 0.01 mm, established that this finer zone size provides reasonable convergence of the numerical solutions.

The most straightforward comparison between the experiments and the CTH calculations are obtained from the velocity histories at the interface between the rear of the aluminum witness plate and the front surface of the lithium-fluoride window. Figure 7.01 shows these comparisons for CLP-6 and CLP-22. For the shot with the lower flyer velocity, CLP-6, the calculated peak witness-plate velocity matches the VISAR record reasonably well, but the numerical record does not decay nearly as rapidly as the measurement. This is probably due to the relatively thin *plate-like* leading edge of the debris cloud, which is not properly modeled in the calculation. In contrast, the higher-velocity comparison for CLP-22 shows excellent agreement for the entire velocity profile. This trend for improved agreement with increasing flyer velocity is consistent with the *vaporization* threshold described earlier. In addition, the debris from this latter shot propagates over a much shorter stand-off distance and has less opportunity to expand and disperse into separate regions. Thus in this case the debris cloud expands in a much more uniform fashion, and is significantly less plate-like in its structure when it impacts the witness plate. The implication is that at these more extreme conditions a non-equilibrium equation of state may not be required to adequately describe the debris generation phenomena. Note that in Figure 7.01 we have labeled the calculated records as *time shifted.* A reason for this is there are numerical issues associated with the calculated initial *jump-off* velocity of the leading edge of the debris cloud from the rear of the target plate, which we have discussed earlier. This potential velocity error can introduce some uncertainty into the simulated arrival times of the debris on the witness plate. In the present context we have bypassed this issue by aligning the calculated and measured VISAR records so that the actual profiles can be more directly compared.

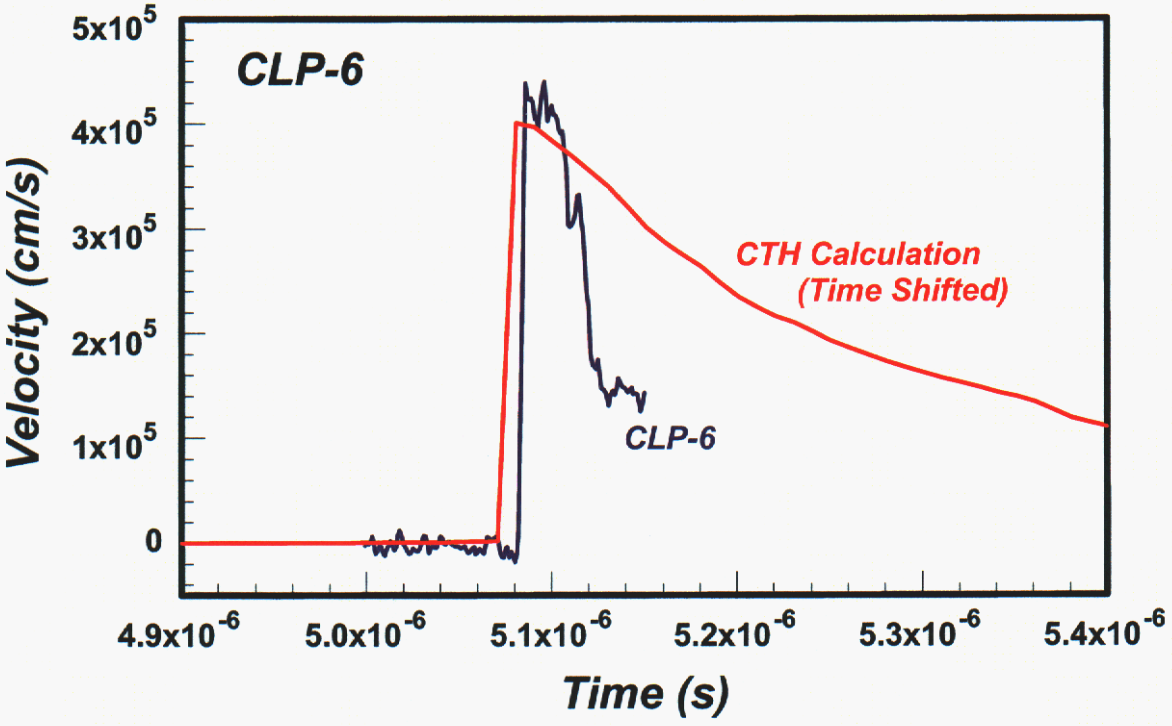

(a) CLP-6

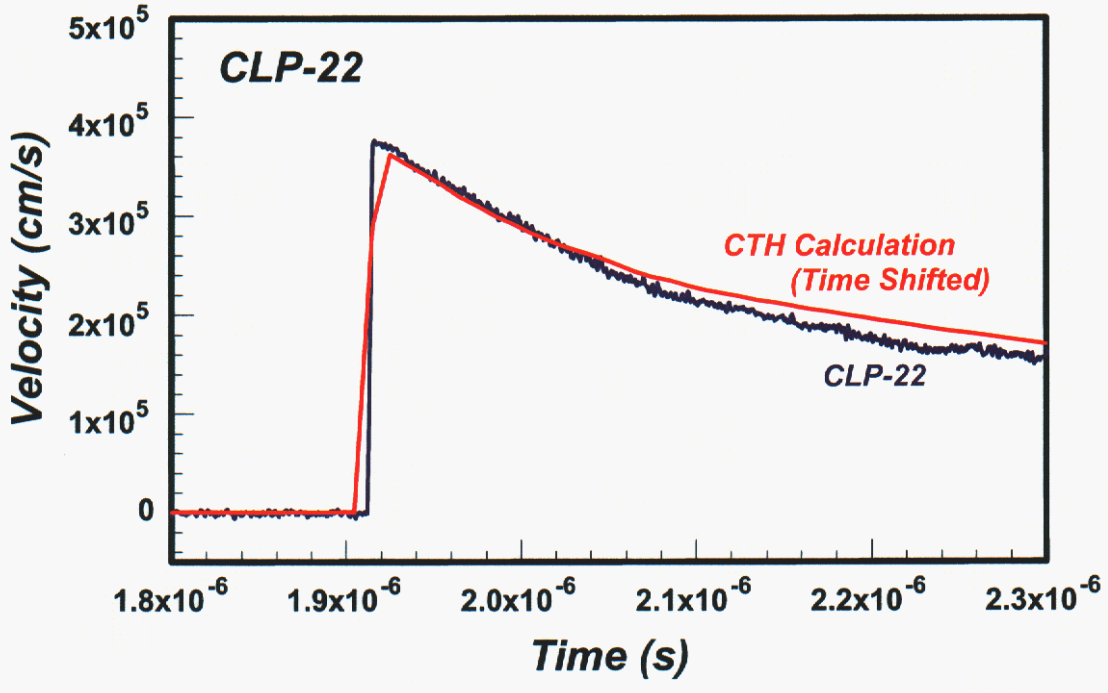

(b) CLP-22

Figure 7.01. *Comparisons of experimental results with CTH simulations for (a) shot CLP-6, and (b) shot CLP-22. Note that the peaks match for both cases, but that the release behavior is well reproduced only for CLP-22 (~11 km/s impact velocity), not for CLP-6 (~9 km/s impact velocity).*

7.2 Other Calculations

Although we felt that we had a reasonable approach to numerical resolution after completing the study on the preliminary configuration (Section 5), there were still a few issues that needed to be addressed. Subsequent modeling in one spatial dimension for other shots indicated that the numerical solutions would only fully converge by using zone sizes on the order of 0.01 to 0.02 mm, which is a factor of five to ten finer than we had used with the 2- and 3-D preliminary analysis. At that time we decided that, because of the computer resources required, very little could be done beyond one-dimensional analyses to address this class of problem at the finest possible level of resolution. As mentioned earlier, this seemed to be a reasonable compromise between computing requirements and desired numerical resolution.

Concern soon developed over the relative influence and importance of one- and two-dimensional effects. This led to exploring various debris propagation distances in both 1-D and 2-D so we could compare the effects of modeling dimensionality and propagation distances. This was where most of our subsequent efforts were directed. A brief summary of the experiments studied with these calculations follows:

CLP-20: A large debris propagation distance of ~75 mm was modeled in 1-D, with a nominal zone size of 0.01 mm. The flyer impact velocity was 6.5 km/s. In contrast to some of the other shots, over-prediction relative to the measured VISAR records resulted. The most reasonable explanation is that this is due to the lack of radial divergence of the debris cloud in the 1-D calculation of the large stand-off configuration, and that a 2-D analysis would give a more realistic simulation and thus a substantially lower peak velocity.

CLP-4: A smaller debris propagation distance (~50 mm) and a higher ~10-km/s impact velocity helps the problem described in connection with 1-D modeling of CLP-20. We ran this problem in 1-D at resolutions of 0.02, 0.01, and even 0.008 mm, and found that the predicted velocities were less than measured, with even the finest zoning yielding a peak velocity down from the experimental value by about 20%.

CLP-22: This shot employed a very short stand-off distance (10 mm) between the target and the witness plate, and thus the response was very nearly one-dimensional. The impact velocity of the flyer on the target was ~11 km/s. We performed many different calculations, in both 1-D and 2-D, and used stand-off distances of 10 mm (the real value) and 50 mm (hypothetical) at several different resolutions. For the smaller propagation distance, the higher resolution (0.02 mm) worked quite well, and matched the experimental VISAR records nicely (Figure 7.01 (b)). We found that for this nearly 1-D experiment, both 1-D and 2-D calculations gave similar results when the same zone sizes were used. To further illustrate the complex issue of numerical resolution and convergence, Figures 7.02 and 7.03 show calculated velocity records from both 1-D and 2-D calculations, for

zone sizes ranging from 0.2 to 0.02 mm, and using both the real and the hypothetical configurations. Different levels and rates of convergence were observed.

CLP-6: This experiment had a stand-off of 23 mm, which represents a debris propagation distance midway between the two cases examined in conjunction with CLP-22. The initial impact velocity was lower, at ~9 km/s. The 1-D computational results matched the measurements quite well for the early part of VISAR record, but less well for latter part, as indicated in Figure 7.01 (a). The comparisons between the calculations and the experimental observations for these last two cases, CLP-6 and CLP-22, are shown and discussed in more detail earlier (Section 7.1).

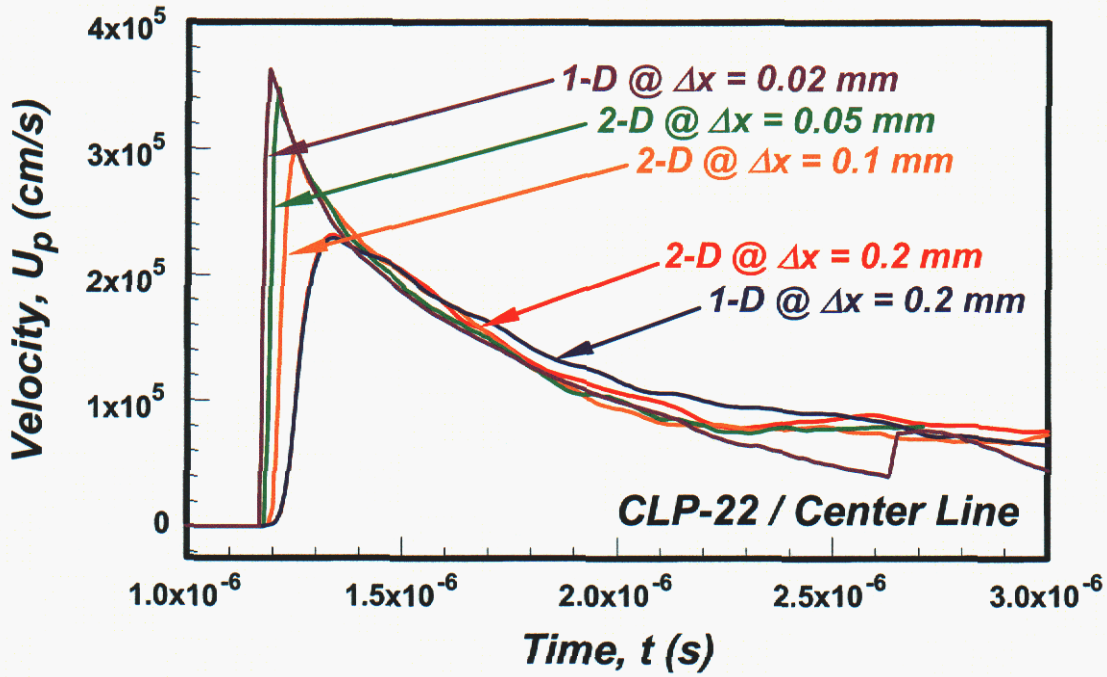

Figure 7.02. *Comparison of numerical resolution for CLP-22. The curves represent the velocity of the witness plate/window interface for 1-D and 2-D calculations, with zone sizes ranging from 0.02 to 0.2 mm. Note that both the 1-D and 2-D traces are fully consistent. It is the 1-D,* Δx *= 0.02 mm curve that is used in the experimental comparison in Figure 7.01 (b).*

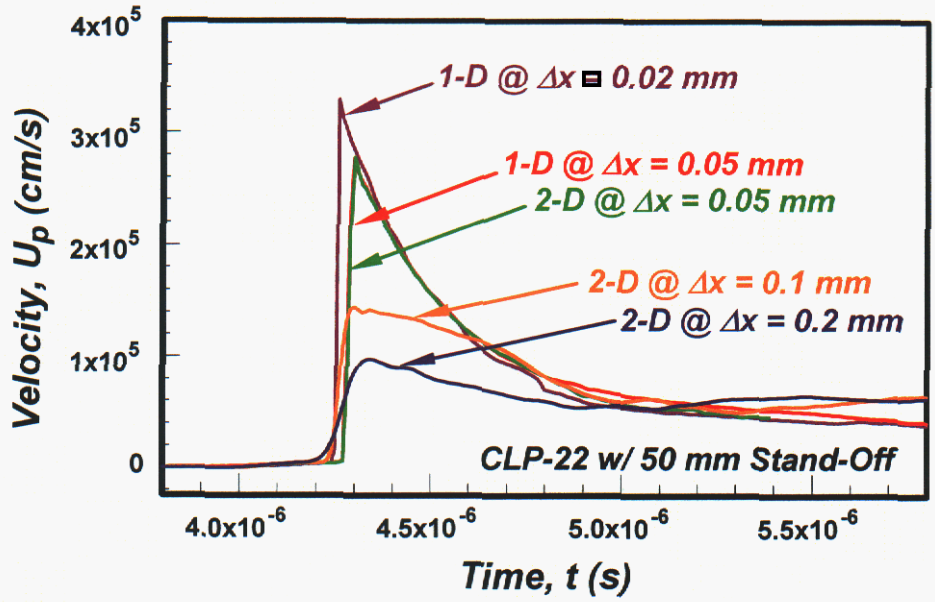

Figure 7.03. *Comparison of numerical resolution for CLP-22 with a hypothetical 50 mm stand-off. As with Figure 7.02, the curves represent the velocity of the witness plate/window interface for zone sizes from 0.02 to 0.2 mm. Again, the 1-D and 2-D traces are consistent, and virtually overlap for* Δx *= 0.05 mm. However, the five-times larger stand-off allows the debris cloud to expand more, significantly changing the character of the variation of the velocity histories with zone size.*

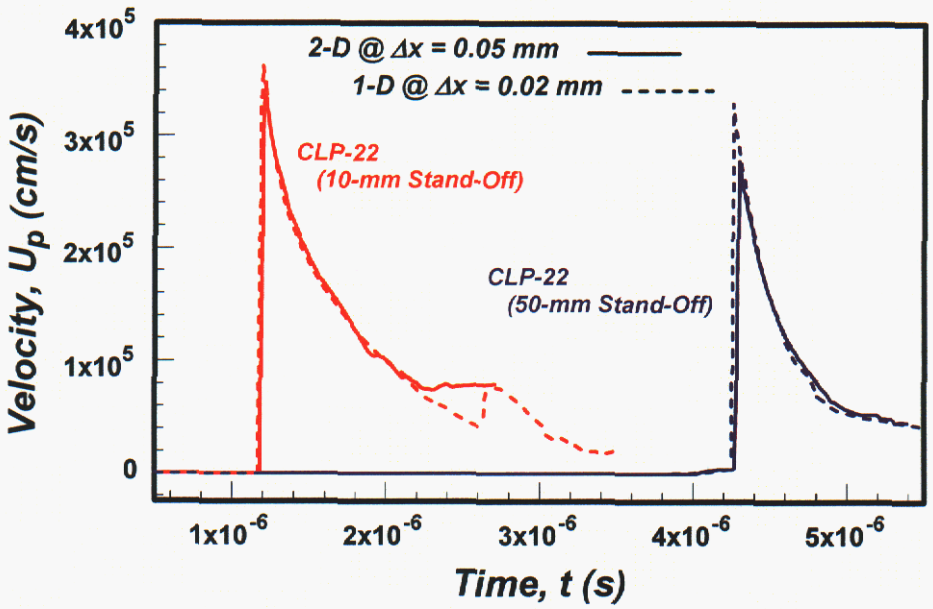

Figure 7.04. *Comparison between fine-zoned calculations for CLP-22 with 10-mm (actual) and 50-mm stand-off distances. Both 1-D and 2-D calculations are shown. The differences in peak amplitude are an indication of the slightly increased two-dimensionality and additional debris dispersion associated with the larger stand-off. The different zone sizes also show different rates of convergence for the two stand-off distances.*

Before leaving the subject of zoning and resolution, we need to make a few additional comments. First, all of the problems examined here are very similar—they all involve hypervelocity impacts on spaced structures with nominal dimensions on the order of centimeters. The principal variations are associated with flyer impact velocity and the stand-off distance over which the debris is allowed to propagate. Even with this similarity it is evident from Figures 7.02 and 7.03 that the rate and degree of numerical convergence often depend in a complicated fashion on the details of the problem being examined. In this case it is the propagation distance for the debris cloud. The coarsest peak velocities are down from the *converged* values by 39 percent for the short stand-off (Figure 7.02), but down by 69 percent for the large stand-off (Figure 7.03)! This difference in convergence can be seen even in Figure 7.04 where we have plotted just the fine-zoned results for these same two cases. These differences are evident even though the 1-D and 2-D calculations are almost identical with each other. For another example, the calculations for the preliminary configuration (with an impact velocity of ~6.5 km/s) seemed to achieve a acceptable level of numerical convergence with a nominal zone size of 0.1 mm. However, subsequent configurations involving impact velocities considerably larger, appeared to require zone sizes much smaller to obtain a similar level of convergence. Our basic conclusion from these observations is that numerical resolution is still an open issue, but it probably depends on the details of the parameters being studied (*e.g.*, impact velocity, debris propagation distance, . . .). If a high level of convergence is critical, the subject should probably be addressed individually for each set of conditions that are to be studied.

Intentionally Left Blank

8. Discussion of Computations

The detailed preliminary analysis led to several important conclusions. Although we would almost always like to have finer numerical resolution, we initially found that for multi-dimensional calculations on targets of the size and complexity represented by this configuration, a reasonable balance among computing time, available resources, and solution accuracy could be obtained with a nominal zone size of ~0.1 mm, even though full numerical convergance was not always attained. However, we subsequently found that calculations at higher impact velocities and with different stand-off distances, mostly using 1-D CTH modeling, showed peak witness-plate velocity amplitudes that indicated a lesser degree of convergence than we had expected. Zone sizes smaller than the base-line value of 0.1 mm by a factor of five or ten may be required to achieve the goal of full convergence for these other configurations. Thus numerical resolution, and its connection with many different problem-specific factors, should still be considered at least partially an open issue.

In any case, after deciding on a 0.1-mm zone size for the initial calculations, we concentrated on the other physics-based issues that needed attention. We first found that the outcome of the impact event is significantly influenced by the flyer geometry. For this particular long-throw experiment, the flyer deformed in-flight leading to a warped geometry at impact on the target. The effect of this warping, modeled as a function of the radius of curvature, was examined with both 2-D axisymmetric and 3-D calculations. As the radius of curvature is increased (*i.e.*, the flyer becomes flatter), the leading-edge velocity of the debris cloud increases with a corresponding decrease in the lateral expansion of the debris cloud. The evolution of the debris cloud has a strong influence on the nature of the loading produced on the witness plate. As the radius of curvature increases, this loading becomes more impulsive in nature. For the case of a flat flyer, a plugging failure in the witness plate was observed. Conversely, as the radius of curvature decreases, the magnitude of the loading on the witness plate decreases, with a corresponding increase in the duration of loading, yielding more blast-like effects. As a result, structural bending of the witness plate becomes more predominant. This is more indicative of the response noted in samples recovered from other similar experiments [36]. Closely related studies involving silica phenolic are described elsewhere [48, 49].

CTH calculations based on early estimates of long-throw flyer curvature (R = 32.6 mm) showed differences from experimental observations. In particular, the flyer was predicted to fold-over on itself after the target impact. This behavior was not indicated in any of the available experimental radiographs. On the other hand, the calculations based upon a larger radius of curvature flyer (R = 65.2 mm) provided much better agreement with the experimental evidence. It is felt that the actual curvature of long-throw flyers was smaller (greater radius of curvature) than the measurement, with the analysis providing rough bounding estimates by bracketing the true flyer geometry. The radius of curvature is a difficult measurement to obtain from the experimental radiographs. Further efforts should be devoted toward improving capabilities to make this measurement as well as to providing quantification of the associated error.

In the 3-D analysis, there were clear shortcomings with the modeling of failure and fragmentation. There are a number of possible reasons for the differences; specifically, the choice of fracture criteria, the actual failure model, and how the model interacts with the numerical mesh, may all be important. The latter possibility certainly influenced the 3-D results, as the cell width associated with the coarse mesh was likely insufficient to accurately describe fracture initiation and eventual breakup of the target plate. The influence of the selected fracture criteria and the failure model on the calculated witness-plate velocities is unclear. Further investigation is required to examine the importance of failure modeling on these quantities.

The follow-on 1-D calculations clarified the jump-off velocity issue, as distinct from the conventional resolution and convergence issues usually associated with hydrocode analyses. It is clear that when the configuration of interest involves the rapid expansion of a high-pressure and high-temperature material into a void or near vacuum, as it does in the debris generation process examined here, significant errors can be introduced into the numerical solution. These discrepancies appear as inaccuracies in the equilibrated expansion velocity of the leading edge of the debris cloud. Because the debris clouds are propagated over appreciable stand-off distances, this can lead to errors in the signal arrival times at the witness plates. The interesting result is that although the arrival times often do not match up, the signal amplitudes, and thus the momenta or impulses delivered to the witness plates, show much smaller discrepancies.

The 1-D Lagrangian calculations also substantiated that equations of state, even for materials as well known as aluminum, still need attention for certain response regimes. As was described earlier, impact conditions examined in this study, especially those at the higher impact velocities, appear to be mostly in a transition region between mechanical- and vaporization-controlled parameter spaces. This transition regime is associated with the onset of vaporization, and occurs for penetrating impacts producing extensive debris clouds, which is certainly the case here. Below the transition region the behavior is dominated by mechanical response phenomena—stress-wave propagation and material failure response—that can in principle be described by one family of models. At more extreme conditions—well above the transition regime—the response is expected to be dominated by vaporization phenomena. For yet more extreme conditions, plasma physics issues come into play, but the latter is not a region that we are addressing here. However, in the transition region—where the materials behave according to a mixture of mechanical and vaporization effects—we feel that the response is not well modeled with the equations of state and constitutive models included with the current generation of hydrocodes. At the lowest impact velocities employed here, material failure issues play a role; while at the highest velocities examined, the debris generation phenomena is beginning to be dominated by vaporization processes. Between these limits, our experimental measurements, and the parallel calculations, are suggesting that the debris generation process is rate dependent and heterogeneous, and thus controlled by non-equilibrium equations of state, which are not readily available. The phenomena associated with this transition region have been observed before in conjunction with analyses dealing with the design of stand-off shields for the protection of space-based

assets [50], and in connection with the shock loading and release of zinc and other metals [5].

One advantage of the extensive analysis performed here is that it has allowed us uncover the issue of non-equilibrium or rate-dependent equations of state as a subject that will be important for certain (but probably limited) parameter regimes. This was an issue that we had not anticipated at the outset of the project. And in fact, we chose aluminum—one of the best known and most studied of all the metals—just to avoid these types of problems!

Intentionally Left Blank

9. Conclusions

In this work, a systematic computational and experimental study was performed to enhance our understanding of debris generation and propagation resulting from shock-induced vaporization of aluminum. Using record-high impact velocities achieved with the Sandia three-stage light-gas gun, aluminum was shocked to thermo-mechanical states sufficiently energetic to produce vaporization upon release. This is the first comprehensive study to investigate the expansion properties of aluminum when shocked to 230 GPa. Velocity histories produced by stagnation of the expansion products against witness plates were measured either at a free surface, or at an aluminum/lithium-fluoride window interface using a velocity interferometers. X-ray measurements of the debris were also conducted using high-speed radiographic techniques. The measured experimental data for aluminum were compared with CTH wave-code calculations using the equation of state for aluminum [12] referred to as SESAME 3700. Some of the key results of the present study are:

- Aluminum was shocked over the calculated stress range from 1 Mb to over 2.3 Mb, and calculated temperatures over the range from 11000 K to 15000 K. In the present investigation, the release products were allowed to propagate over distances of up to 50 mm (~ 50 times the plate thickness) or more.
- As shown by the radiographs, at lower impact velocities fracture and fragmentation play a significant role in the debris generation process. At the still relatively high temperatures involved, these failure mechanisms are not particularly well modeled.
- Shocks followed by rapid releases are observed at an aluminum/lithium-fluoride window interface, suggesting that thin *plate-like* debris is interacting with the witness plate.
- Radiographic measurements of the impact generated products confirm that the expansion debris is *plate-like*. Time-dependent vaporization is also indicated.
- Release isentropes from shocked stress levels below 140 GPa indicate little or no vaporization when the material is expanded over propagation distances of 10 mm.
- Both radiographs and witness-plate velocity measurements suggest that the vaporization process is both time-dependent and heterogeneous when the material is released from shocked states around 230 GPa.
- The threshold for vaporization kinetics in aluminum becomes significant when expanded from shocked states over 230 GPa.
- Release isentropes calculated using the SESAME equation of state for aluminum suggest that good agreements can be obtained if the debris products are modeled as a plate.
- Experiments at 11 km/s which indicate ramp-loading followed by shocks are not simulated well because the time-dependent vaporization processes are not modeled in the calculations.
- Numerical resolution and convergence issues, especially for multi-dimensional configurations and hydrocodes, are important and complex problems. They

should probably be addressed individually for each major set of conditions to be investigated.

Natural extensions of this work include the need to: (1) further quantify these measurements with estimates of vapor fractions in the expanded debris products; (2) perform three-dimensional calculations with refined meshes to simulate 3-D inclined plate impact experiments; (3) adjust the critical point parameters to better match experiments when vaporization does occur; and (4) enhance the theoretical models to include boiling kinetics and improved high-temperature failure models for use with existing hydrocodes and equation-of-state models.

References

1. A. V. Bushman and V. E. Fortov, "Wide-range equations of state for matter under extreme conditions," *Sov. Tech. Rev. B. Therm. Phys.* **2**, 219–336 (1987).
2. J. R. Asay, T. G. Trucano, and L. C. Chhabildas, "Time-resolved measurements of shock-induced vapor-pressure profiles," *Shock Waves in Condensed Matter – 1987* (Eds., S. C. Schmidt and N. C. Holmes), pp. 159-162, Elsevier Science Publishers B. V. (1988)
3. J. R. Asay and T. G. Trucano, "Studies of density distributions in one-dimensional shock-induced debris clouds," *Int. J. Impact Engng.* **10**, 35-50 (1990).
4. S. A. Mullin, C. E. Anderson, Jr., and J. S. Wilbeck, "Dissimilar material scaling relationships for hypervelocity impact," Prepared by Southwest Research Institute for Defense Nuclear Agency under contract DNA001-86-C-0037, Project 06-1039-001, DNA-TR-89-112 (1990).
5. R. M. Brannon, L. C. Chhabildas, "Experimental and numerical investigation of shock-induced full vaporization of zinc," *Int. J. Impact Engng.* **17**, 109-120 (1995).
6. G. I. Kerley and J. L. Wise, "Shock-induced vaporization of porous aluminum," *Shock Waves in Condensed Matter – 1987* (Eds., S. C. Schmidt and N. C. Holmes), pp. 155-158, Elsevier Science Publishers B. V. (1988).
7. J. L. Wise, G. I. Kerley, and T. G. Trucano, "Shock-vaporization studies on zinc and porous carbon," *Shock Compression of Condensed Matter – 1991*, (Eds., S. C. Schmidt, R. D. Dick, J. W. Forbes, D. G. Tasker), pp. 61-64, Elsevier Science Publishers B.V. (1992).
8. L. C. Chhabildas, L. M. Barker, J. R. Asay, T. G. Trucano, G. I. Kerley, and J. E. Dunn, "Launch Capabilities to Over 10 km/s," *Shock Waves in Condensed Matter – 1991* (Eds., S. C. Schmidt, R. D. Dick, J. W. Forbes, and D. G. Tasker), p. 1025, Elsevier Science Publishers B. V. (1992).
9. L. C. Chhabildas, J. E. Dunn, W. D. Reinhart, and J. M. Miller, "An impact technique to accelerate flier-plate velocities to over 12 km/s," *Int. J. Impact Engng.* **14**, 121-132 (1993).
10. L. C. Chhabildas, L. N. Kmetyk, W. D. Reinhart, and C. A. Hall, "Enhanced hypervelocity launcher, Capabilities to over 16 km/s," *Int. J. Impact Engng.* **17**, 183-194 (1999).
11. S. L. Thompson and H. S. Lauson, *Improvements in the CHARTD Radiation-Hydrodynamics Code III: Revised Analytic Equation of State*, SC-RR-710714, Sandia Laboratories, Albuquerque, New Mexico (1972).
12. G. I. Kerley, "Theoretical equation of state for aluminum," *Int. J. Impact Engng.* **5**, 109-120 (1987).
13. J. M. Mcglaun and S. L. Thompson, "CTH: A Three-Dimensional Shock Wave Physics Code," *Int. J. Impact Engng.* **10**, 351-360 (1990).

14. E. S. Hertel, R. L. Bell, M. G. Elrick, A. V. Farnsworth, G. I. Kerley, J. M. McGlaun, S. V. Petney, S. A. Silling, P. A. Taylor, and L Yarrington, *CTH: A Software Family for Multi-Dimensional Shock Physics Analysis*, SAND92-2089C, Sandia National Laboratories, Albuquerque, NM (1993).
15. R. L. Bell, M. R. Baer, R. M. Brannon, D. A. Crawford, M. G. Elrick, E. S. Hertel, S. A. Silling, and P. A. Taylor, "CTH User's Manual and Input Instructions, Version 6.0," Sandia National Laboratories, Albuquerque, NM (2000).
16. M. B. Boslough, J. A. Ang, L. C. Chhabildas, W. D. Reinahrt, C. A. Hall, B. G. Cour-Palais, E. L. Christiansen, and J. L. Crews, "Hypervelocity Testing of Advanced Shielding Concepts for Spacecraft Against Impacts to 10km/s," *International Journal of Impact Engineering*, **14**, pp. 95-106 (1993).
17. L. C. Chhabildas, W. D. Reinhart, D. E. Carroll, G. I. Kerley, and T. F. Thornhill, *Equations of State Studies of Graphite-Epoxy and of Glass/Rubber/Graphite-Epoxy Composites for Engagement Velocities to 12 km/s*, SAND2001-1405, Sandia National Laboratories, Albuquerque, NM, (2001).
18. L. C. Chhabildas, W. D. Reinhart, D. E. Carroll, G. I. Kerley, and T. F. Thornhill, *Equation of State Studies of Silica Phenolic to 150 GPa, Using a Three-Stage Launcher to 11 km/s*, SAND2001-1404, Sandia National Laboratories, Albuquerque, NM (2001).
19. L. C. Chhabildas, L. M. Barker, J. R. Asay, and T. C. Trucano, "Relationship of Fragment Size to Normalized Spall Strength for Materials," *International Journal of Impact Engineering*, **10**, pp. 107-124 (1990).
20. L. C. Chhabildas and J. R. Asay, "Dynamic Yield Strength and Spall Strength Measurements under Quasi-Isentropic Loading," *Shock Waves and High Strain-Rate Phenomena in Materials* (M. A. Meyers, L. E. Murr and K. P. Staudhammer, eds), Marcel Decker, pp. 947-955 (1992).
21. L. M. Barker, "High Pressure Quasi-Isentropic Impact Experiments," *Shock Waves in Condensed Matter – 1983* (J. R. Asay, R. A. Graham, and G. R. Straub, Eds), Elsevier Science Publishers, pp. 217-224 (1984).
22. T. F. Thornhill, W. D. Reinhart, C. H. Konrad, and L. C. Chhabildas, "Accurate Velocity Measurements of the Two-Stage Light-Gas Gun Projectile," *51st Aeroballistics Range Association Proceedings*, Madrid, Spain (2002).
23. C. H. Konrad, "Analysis for the Sandia National Laboratories (SNL) Optical Beam Reflectance (OBR) Technique," Internal Memo, Sandia National Laboratories, Albuquerque, NM (1999).
24. N. C. Holmes, "Analysis of Errors for Optical Beam Reflective Date for JASPER," Internal Memo, University of California, Lawrence Livermore National Laboratory (1999).
25. W. D. Reinhart, L. C. Chhabildas, D. E. Carroll, T. K. Bergstresser, T. F. Thornhill, and N. A. Winfree, "Equation of state measurements of materials using a three-stage gun to impact velocities of 11 km/s," *Int. J. Impact Engng.* **26**, 625-637 (2001).

26. D. E. Carroll, L. C. Chhabildas, W. D. Reinhart, N. A. Winfree, and G. I. Kerley, "Computational characterization of three-stage gun flyer plate launch," *Shock Waves in Condensed Matter – 2001* (Eds., M. D. Furnish, N. N Thadhani, and Y. Horie), pp. 307-310, AIP Conference Proceedings **620** (2002).

27. Instruction Manual, X-Ray Tube Model XT 150, Scandiflash AB (1990).

28. TDS 500D, TDS 600C & TDS 700D Digitizing Oscilloscopes Performance Verification and Specifications, Tektronix Inc.

29. L. M. Barker and R. E. Hollenbach, "Laser interferometer for measuring high velocities of any reflecting surface," *J. Appl. Phys.* **43**, pp. 4669-4675 (1972).

30. L. M. Barker and R. E. Hollenbach, "Shock-wave studies of PMMA, fused silica, and sapphire," *Journal of Applied Physics*, **41**, pp. 4208-4226 (1970).

31. L. M. Barker and K. W. Schuler, "Correction to the Velocity-per-fringe Relationship for the VISAR Interferometer," *Journal of Applied Physics*, **45**, pp. 3692-693 (1974).

32. J. L. Wise and L. C. Chhabildas, "Laser interferometer measurements of refractive index in shock compressed materials," *Shock Waves in Condensed Matter* (Ed., Y. M. Gupta), pp. 441-454, Plenum Press, N.Y (1986).

33. W. F. Hemsing, "Velocity Sensing Interferometer (VISAR) Modification," *Rev. Scientific Instruments*, **50**, pp. 73-78 (1979).

34. M. D. Furnish, L. C. Chhabildas, and W. D. Reinhart, "Time-Resolved Particle Velocity Measurements at Impact Velocities of 10km/s," *Int. J. Impact Engng.* **23**, 261-270 (1999).

35. L. C. Chhabildas, M. D. Furnish, and W. D. Reinhart, "Shock-induced melting in aluminum: wave-profile measurements," *Shock Waves in Condensed Matter – 1999* (Eds., M. D. Furnish, L. C. Chhabildas, and R. S. Hixson), pp. 97-100, AIP Conference Proceedings **505** (2000).

36. S. L. Thompson, *ANEOS Analytic Equations of State for Shock Physics Codes Input Manual*, SAND89-2951, Working draft, Sandia National Laboratories, Albuquerque, NM (1990).

37. D. J. Steinberg, *Equation of State and Strength Properties of Selected Materials*, UCRL-MA-106439, Change 1, Lawrence Livermore National Laboratory (1996).

38. J. M. McGlaun, Sandia National Laboratories, Albuquerque, NM, Private communication.

39. E. S. Hertel, *Comparison of Analytic Whipple Bumper Shield Ballistic Limits with CTH Simulations*, SAND92-0347, Sandia National Laboratories, Albuquerque, NM (1993).

40. L. N. Kmetyk, L. C. Chhabildas, M. B. Boslough, and R. J. Lawrence, *Effect of Phase Change in a Debris Cloud on a Backwall Structure*, SAND94-0878, Sandia National Laboratories, Albuquerque, NM (1994).

41. C. E. Anderson, T. G. Trucano, and S. A. Mullin, *Debris Cloud Dynamics*, SAND87-2298J, Sandia National Laboratories, Albuquerque, NM (1987).

42. L. C. Chhabildas, M. B. Boslough, W. D. Reinhart, and C. A. Hall, "Debris Cloud Characterization at Impact Velocities of 5 to 11 km/s," *Shock Compression of Condensed Matter – 1994*, Proceedings of the Conference of the American Physical Society Topical Group on Shock Compression of Condensed Matter, American Institute of Physics Press, New York, pp. 1841-1844 (1994).
43. C. H. Konrad, L. C. Chhabildas, and M. B. Boslough, "Dependence of Debris Cloud Formation on Projectile Shape," *Shock Compression of Condensed Matter – 1994*, Proceedings of the Conference of the American Physical Society Topical Group on Shock Compression of Condensed Matter, American Institute of Physics Press, New York, pp. 1845-1848 (1994).
44. M. E. Kipp and R. J. Lawrence, *WONDY V—A One-Dimensional Finite-Difference Wave Propagation Code*, SAND81-0930, Sandia National Laboratories, Albuquerque, NM (1982).
45. T. C. Carney, Los Alamos National Laboratory, Los Alamos, NM, Private communication (2001).
46. M. Gerassimenko, Lawrence Livermore National Laboratory, Livermore, CA, Private communication (2001).
47. A. V. Farnsworth Jr., Sandia National Laboratories, Albuquerque, NM, Private communication (2002).
48. L. C. Chhabildas, W. D. Reinhart, T. F. Thornhill, G. C. Bessette, R. J. Lawrence, and D.E. Carroll, *Validation Studies for Target Materials of Interest at Impact Velocities from 6 to 11 km/s*, SAND2002-0516, Sandia National Laboratories, Albuquerque, NM (2002).
49. R. P. Nance, J. R. Cogar, L. C. Chhabildas, W. D. Reinhart, and T. G. Thornhill, "Influence of Plate Curvature in Hypervelocity Flyer-Plate Impacts," Proceedings of the Conference on *New Models and Hydrocodes for Shock Waves in Condensed Matter*, 19–24 May 2002, Edinburgh, Scotland (2002).
50. R. J. Lawrence, *A Simple Approach for the Design and Optimization of Stand-Off Hypervelocity Particle Shields*, AIAA Paper No. 92-1465, AIAA, Washington, DC (1992).

Distribution

1 Dominca
Attn: Nancy Winfree
9813 Admiral Dewey Ave. NE
Albuquerque, NM 87111

1 BAE SYSTEMS
Attn. Steven W. Clark
310 Voyager Way
Huntsville, AL 35806

2 Office of Secretary of Defense
Attn: Len Sakell, Director-Operational Test & Evaluation, Room 1C730
Mario Lucchese, Room 1C730
1700 Defense Pentagon
Washington, DC 20301-1700

1 Theater Missile Defense
Program Element Office
Attn: Mike Brown
2531 Jefferson Davis Hwy
Arlington, VA 22242-5170

1 U.S. Army Evaluation Analysis Center
Attn: Todd Fisher, Director
4120 Susquehanna Avenue
Aberdeen Proving Ground, MD 21005-1303

2 U.S. Army Space and Missile Defense Command
Attn: Robert Becker, SMDC-TC-MT-KL
Milan Dutta, SMDC-TC-MT-KL
P.O. Box 1500
Huntsville, AL 35807-3801

1 GBI Project Management Office
Attn: Charlie Dobson, GMG-TE
P.O. Box 1500
Huntsville, AL 35807-3801

1 Kerley Technical Services
Attn: Gerald I. Kerley, consultant
P.O. Box 709
Appomattox, VA 24522-0709

1 Applied Research Associates, Inc.
Attn: Dennis Grady
4300 San Mateo Blvd. NE
Albuquerque, NM 87111

6 Naval Surface Warfare Center
Attn: John Borg, Code G22
Russ Brown, Code B51
John Cogar, Code G24
R. K. Garrett, Jr., Code G22
Michael Hopson, Code G22
Leonard Wilson, Code G24
17320 Dahlgren Rd.
Dahlgren, VA 22448-5100

2 The Pentagon
Attn: Tony England, MDA/GMT
Lt. Col Sylvia Ferry, MDA/SET
7100 Defense Pentagon
Washington, DC 20301-7100

3 Missile Defense Agency / SE
Attn: Marlene Owens, MDA/SE
Kathleen Loper, MDA/SE
Michael Cross, MDA/SE
1301 Southgate Road
Arlington, VA 22202

6 The University of California
Lawrence Livermore National Laboratory
Attn: Douglas R. Faux, L-140
Michel Gerassimenko, L-183
Glenn W. Pomykal, L-183
David A. Young, L-045
Frank Handler
Neil C. Holmes
P.O. Box 808
Livermore, CA 94551-0808

1 BATTELLE
Attn: Carl Alexander
505 King Ave.
Columbus, OH 43201

5 The University of California
Los Alamos National Laboratory
Attn: T. C. Carney, MS-F665
R. P. Swift, MS-F665
D. S. Prono, MS-F613D
L. A. Schwalbe
R. S. Hixon, MS-P952
P.O. Box 1663
Los Alamos, NM 87545

1 Teledyne Solutions, Inc.
Attn: John Newquist
5000 Bradford Drive, Suite 200
Huntsville, AL 35805-1953

3 NASA Johnson Space Center
Attn: J. C. Crews, SN3
E. C. Christiansen, SN3
J. S. Kerr, SN3
Mail Code: AH3
2101 NASA Road One
Houston, TX 77058

1 U.S. Air Force
AFDTC
WL/MNSA
Attn: J. C. Foster Jr. AD/MNW
104 Cherokee Avenue
Eglin AFB, FL 32542-5434

2 Boeing Company
Attn: Sherry Riddle
Ron Peasle
P.O. Box 24002
Huntsville, AL 35824-6402

1 ITT Industries, Advanced Engineering & Sciences Division
Attn: Nasit Ari
5009 Centennial Blvd.
Colorado Springs, CO 80919

2	DSTL Porton Down Attn: Graham Cambray Nick Robinson Salisbury SP4 OJQ United Kingdom		
1	MS	0318	P. Yarrington, 9230
1		0479	W. J. Tedeschi, 2113
1		0751	R. M. Brannon, 6117
1		0819	D. E. Carroll, 9231
1		0819	R. M. Summers, 9231
1		0819	T. G. Trucano, 9211
1		0820	P. F. Chavez, 9232
5		0820	G. C. Bessette, 9232
1		0820	P. N. Demmie, 9232
1		0820	M. E. Kipp, 9232
1		0820	P. A. Taylor, 9232
1		0824	J. L. Moya, 9130
1		0824	A. C. Ratzel, 9110
1		0828	M. Pilch, 9133
1		0834	W. M. Trott, 9112
1		0835	E. A. Boucheron, 9141
1		0835	J. M. McGlaun, 9140
1		0836	L. J. DeChant, 9116
1		0836	E. S. Hertel, 9116
1		0836	R. G. Schmitt, 9116
1		0893	J. Pott, 9123
1		1156	W. V. Saul, 15322
1		1164	J. T. Hitchcock, 15403
1		1164	J. L. McDowell, 15400
1		1168	C. Deeney, 1646
1		1168	M. D. Furnish, 1647
1		1178	D. D. Bloomquist, 1630
1		1181	J. P. Davis, 1646
1		1181	M. D. Knudson, 1646
10		1181	L. C. Chhabildas, 1647
1		1181	C. A. Hall, 1647
10		1181	W. D. Reinhart, 1647
2		1181	T. F. Thornhill, 1647
1		1181	T. J. Vogler, 1647
1		1185	R. J. Dukart, 15417
1		1185	D. P. Kelly, 15417
1		1185	E. W. Reece, 15401
1		1185	R. J. Weir, 15417

10	1186	R. J. Lawrence, 1674
1	1186	T. A. Mehlhorn, 1674
1	1190	J. P. Quintenz, 1600
1	1191	K. M. Matzen, 1670
1	1194	D. H. McDaniel, 1640
1	1421	G. A. Samara, 1120
1	9018	Central Technical Files, 8945-1
2	0899	Technical Library, 9616
1	0612	Review & Approval Desk, 9612 For DOE/OSTI

Intentionally Left Blank